
TABLE OF CONTENTS

ABSTRACT	I
RÉSUMÉ	IV
ACKNOWLEDGEMENT	VII
TABLE OF CONTENTS	IX
LIST OF TABLES	XIII
LIST OF FIGURES	XV
CHAPTER 1 INTRODUCTION	1
1.1 DEFINITION OF PROBLEMS.....	2
1.2 OBJECTIVES	5
REFERENCES.....	8
CHAPTER 2 LITERATURE REVIEW	10
2.1 INTRODUCTION OF 8XXX ALUMINUM CONDUCTOR ALLOYS	11
2.1.1 Industrial application of 8xxx aluminum conductor alloys	11
2.1.2 Fabrication process of 8xxx aluminum conductor alloys	12
2.1.3 Alloying elements in 8xxx aluminum conductor alloys	13
2.1.4 Properties requirements for aluminum conductors.....	17
2.2 ELECTRICAL PROPERTIES OF 8XXX ALUMINUM CONDUCTOR ALLOYS	18
2.3 MECHANICAL PROPERTIES OF 8XXX ALUMINUM CONDUCTOR ALLOYS	21
2.3.1 Substructure strengthening	23

2.3.2	Solid solution strengthening	26
2.3.3	Particle strengthening	28
2.4	CREEP BEHAVIOUR OF ALUMINUM CONDUCTOR ALLOYS	30
2.4.1	Creep phenomenon	30
2.4.2	Characterizations of creep properties	33
2.4.3	Creep threshold stress	35
2.4.4	Creep stress exponent	45
2.4.5	Analyzing the creep mechanisms	58
2.4.6	Investigation of creep properties in aluminum conductors.....	59
	REFERENCES.....	61
CHAPTER 3	EXPERIMENTAL	69
3.1	EXPERIMENTAL DESIGN.....	70
3.2	MICROSTRUCTURE OBSERVATION.....	73
3.2.1	Optical microscopy (OM).....	73
3.2.2	Scanning electron microscopy (SEM)	73
3.2.3	Electron backscatter diffraction (EBSD)	73
3.2.4	Transmission electron microscopy (TEM)	74
3.3	PROPERTIES MEASUREMENTS	75
3.3.1	Electrical conductivity	75
3.3.2	Microhardness.....	76
3.3.3	Tensile test	76

3.3.4	Compression test.....	77
3.3.5	Creep test	77
	REFERENCES.....	80
CHAPTER 4 EFFECT OF FE ON MICROSTRUCTURE AND PROPERTIES OF 8XXX ALUMINUM CONDUCTOR ALLOYS		81
4.1	INTRODUCTION	83
4.2	MATERIAL AND METHODS	85
4.3	RESULTS AND DISCUSSION.....	86
4.3.1	Microstructures of as-cast and extruded materials	86
4.3.2	Effect of Fe on mechanical and electrical properties.....	91
4.3.3	Effect of Fe on creep properties.....	94
4.4	CONCLUSIONS.....	101
	REFERENCES.....	103
CHAPTER 5 EFFECT OF FE-RICH INTERMETALLIC PARTICLES AND FE SOLUTES ON CREEP BEHAVIOR OF 8XXX ALUMINUM CONDUCTOR ALLOYS		105
5.1	INTRODUCTION	107
5.2	MATERIAL AND EXPERIMENTAL PROCEDURE	109
5.3	RESULTS.....	111
5.3.1	Distribution of Fe-rich intermetallics and Fe solutes	111
5.3.2	Creep behavior.....	114

5.4	DISCUSSIONS	120
5.4.1	Effect of Fe-rich intermetallic.....	122
5.4.2	Effect of Fe solutes	125
5.5	CONCLUSIONS.....	127
	REFERENCES.....	129
CHAPTER 6 EFFECTS OF MINOR CU AND MG ADDITIONS ON MICROSTRUCTURE AND MATERIALS PROPERTIES OF 8XXX ALUMINUM CONDUCTOR ALLOYS		131
6.1	INTRODUCTION	133
6.2	EXPERIMENTAL	135
6.3	RESULTS AND DISCUSSION.....	137
6.3.1	Microstructure evolution	137
6.3.2	Electrical conductivity and tensile strength.....	142
6.3.3	Effects of Cu and Mg on creep properties	149
6.4	CONCLUSIONS.....	157
	REFERENCE	158
CHAPTER 7 CONCLUSIONS AND RECOMMENDATIONS		160
7.1	CONCLUSIONS.....	161
7.2	RECOMMENDATIONS	165
PUBLICATIONS		166

LIST OF TABLES

Table 1.1 Chemical composition limits for AA1350 and AA8xxx aluminum alloy as electrical conductors [10,11].....	3
Table 2.1 Comparison of physical and mechanical properties of some typical aluminum conductor alloys.....	17
Table 2.2 Effect of alloying elements in and out of the solid solution on the resistivity of aluminum.....	20
Table 2.3 Comparative effects of different mechanisms on strength and resistivity in aluminum [33].....	22
Table 2.4 Atomic radius, shear modulus and strengthening parameter H of Cu and Mg in aluminum [46].....	27
Table 2.5 Estimated increase of aluminum hardness caused by 1% addition of Cu and Mg in different tempers.....	27
Table 2.6 Threshold stress models proposed for the dispersoids strengthened alloys.....	37
Table 3.1 Chemical compositions of the experimental alloys at 0.3% Fe used in this work.....	70
Table 3.2 Chemical compositions of the experimental alloys at 0.5% Fe used in this work.....	71
Table 3.3 Chemical compositions of the experimental alloys at 0.7% Fe used in this work.....	71
Table 3.4 Parameters of the thermal holding treatment methods in this study.....	72

Table 4.1 Chemical composition of experimental alloys studied (wt.%).	85
Table 5.1 Chemical composition (wt.%) of the alloys.....	110
Table 5.2 Concentration of Fe solutes in the samples.....	113
Table 5.3 Experimentally estimated increments of threshold stresses $\Delta\sigma_{th}$, $\Delta\sigma_{th}(P)$ for $FeAl_3$ particles and $\Delta\sigma_{th}(S)$ for Fe solutes at various temperatures (MPa).....	122
Table 5.4 The calculated Orowan stress σ_{or} and detachment stress σ_d for the alloys.....	125
Table 6.1 Chemical compositions of the experimental alloys investigated (wt.%).	136

LIST OF FIGURES

Fig. 1.1 Cable products available in feeder sizes only.....	2
Fig. 2.1 Backscattered electron image for four different types of frequent Fe-rich particles: (a) Al_mFe , (b) Al_6Fe , (c) $FeAl_3$ and (d) $\alpha-AlFeSi$ (Al_8Fe_2Si).....	14
Fig. 2.2 Optical micrograph (a) and TEM image (b) of Al–0.75 wt.% Fe–0.15 wt.% Mg alloy rods continuously fabricated [13] (magnification 500 times for optical micrograph).	15
Fig. 2.3 TEM micrograph of Al–Fe–Mg alloys showing particles on sub-boundaries [41].	25
Fig. 2.4 Sketch of a dislocation passing two hard particles, based on the Orowan mechanism [44]......	29
Fig. 2.5 Typical creep curve showing the three stages of creep. The dotted line shown in the figure is for the compression creep curves.	31
Fig. 2.6 Configuration representing particle dislocation interactions in 2014 Al, revealing the presence of threshold stress [66]......	36
Fig. 2.7 Creep threshold stress, normalized with respect to a calculated Orowan stress at 300 °C, as a function of average precipitate radius.	38
Fig. 2.8 Threshold stress originated from two processes, (a) threshold stress in the competing process, (b) corresponding energy profile, (c) threshold stress in the sequential process, (d) energy profile.	43
Fig. 2.9 Schematic view of vacancy diffusion during N-H and Coble creep. Arrows indicate the flow of vacancies through the grains from boundaries lying normal to the tensile direction to parallel boundaries. Thicker arrows indicate the tensile axis.	46

Fig. 2.10 Grain-boundary sliding creep mechanism.....	47
Fig. 2.11 The slip bands and GBS of aluminum during creep deformation. (a) slip in an aluminum crystal deformed at a slow creep rate at 573 K. $\times 30$; (b) GBS of aluminum, the close parallel lines are markers introduced during the preparation of the sample [102]. ...	48
Fig. 2.12 Schematic view of class-A creep mechanism.....	49
Fig. 2.13 Dislocation structures for steady-state creep of Al–Mg alloys at 359 °C [105]..	51
Fig. 2.14 Mechanism of dislocation-climb creep.....	52
Fig. 2.15 TEM micrographs of post-creep dislocation structures of Al–0.3 wt.% Sc alloy aged at 300 °C for 5 h and crept at 300 °C under 36 MPa [42].....	53
Fig. 2.16 Schematic illustration of strain rate versus stress for Al–Mg alloy, showing the transition in creep mechanisms [116].	56
Fig. 2.17 Creep deformation mechanism map Ashby-map [122].....	59
Fig. 3.1 Experimental equipment used in this work, (a) Optical microscopy (OM), (b) Scanning electron microscopy (SEM), and (c) Transmission electron microscopy (TEM)... ..	75
Fig. 3.2 Experimental equipment used in this work, (a) SigmaScope SMP10 electrical conductivity meter, (b) Megger resistance ohmmeter, (c) HVS-1000 Digital Micro Hardness Tester, (d) Instron 8801 tensile test system, (e) Gleeble 3800 device, and (f) compression creep test machine.....	79
Fig. 4.1 Optical micrographs showing the as-cast grain structures: (a) Al3; (b) Al5; (c) Al7.	87
Fig. 4.2 Typical characteristics of Fe-rich intermetallics in Fig. 4.1: (a) SEM micrograph; (b)	

EDS spectrum; (c) EBSD pattern; (d) simulated solution of EBSD pattern, identifying Al_mFe phase with a lower mean angular deviation of 0.315.	88
Fig. 4.3 Optical micrographs of the extruded samples: (a) Al3; (b) Al5; (c) Al7, showing fine Fe-rich intermetallic particles distributed along the extrusion direction (ED).	89
Fig. 4.4 Orientation imaging maps of the extruded samples with different Fe contents: (a) Al3; (b) Al5; (c) Al7; (d) Inversed pole figure color map and extrusion direction (ED).	91
Fig. 4.5 Evolution of mechanical properties (a) and EC (b) with different Fe contents.	92
Fig. 4.6 Mechanical properties (a) and EC (b) of the samples after annealing at 350 °C for 4 h.	93
Fig. 4.7 Typical creep strain (ϵ) (a) and instantaneous creep rate ($\dot{\epsilon}$) (b) curves of the samples with different Fe contents, tested at 100 °C and 69 MPa.	95
Fig. 4.8 Double logarithmic plot of the minimum creep rate $\dot{\epsilon}_m$ against applied stress σ for Al3, Al5, and Al7 alloys.	96
Fig. 4.9 Double logarithmic plot of minimum creep rate $\dot{\epsilon}_m$ vs effective stress $\sigma - \sigma_{th}$ for Al3, Al5 and Al7 alloys.	97
Fig. 4.10 TEM bright field images of Al3 samples after creep at 100 °C and 69 MPa, representing interaction between dislocations and dispersion particles: (a) dislocation pile-up at Al_mFe intermetallic particles, (b) subgrain boundary blocking the dislocation motion, and (c) intermetallic particles distributed on subgrain boundaries.	99
Fig. 4.11 Relation between the threshold stress, σ_{th} and Orowan stress, σ_{or}	100
Fig. 5.1 SEM back-scattered micrographs of the Alloy A3 (a-b) and Alloy A7 (c-d) after thermal holding treatments.	112
Fig. 5.2 Binary Al–Fe phase diagram illustrating the solid solubility of Fe content at a given	

temperature [24].	114
Fig. 5.3 Typical compressive curves of the alloys: (a) creep strain (ε) and (b) instantaneous creep rate ($\dot{\varepsilon}$), tested at 100 °C and applied load of 45 MPa	115
Fig. 5.4 Variations of minimum creep rate $\dot{\varepsilon}_m$ with applied stress σ for alloys tested at 100 °C (a), 150 °C (b), and 200 °C (c).	116
Fig. 5.5 Determining the threshold stress by linear fitting $\log \dot{\varepsilon}_m$ against $\log \sigma$ for A3L alloys (a) and the threshold stress σ_{th} of all the alloys at the three test temperatures (b).	118
Fig. 5.6 Logarithmic plots of minimum creep rate $\dot{\varepsilon}_m$ vs the effective stress, $\sigma - \sigma_{th}$, for alloys at three temperatures: 100 °C (a), 150 °C (b), and 200 °C (c).	120
Fig. 5.7 The increment of threshold stress $\Delta\sigma_{th}$ due to FeAl_3 particles and Fe solutes with increasing temperatures.	122
Fig. 5.8 The diffusion rate of Al and Fe in aluminum as a function reciprocal temperature [12].	127
Fig. 6.1 Optical micrographs showing the particles distribution of the alloys: (a) Al-0.3Fe, (b) Al-0.3Fe-0.29Cu, (c) Al-0.7Fe, and (d) Al-0.7Fe-0.18Cu-0.1Mg, showing fine Fe-rich intermetallic particles distributed along the extrusion direction (ED).	139
Fig. 6.2 Orientation image mapping showing the extruded microstructure of the alloys: (a) Al-0.3Fe, (b) Al-0.3Fe-0.29Cu, (c) Al-0.7Fe, (d) Al-0.7Fe-0.18Cu-0.1Mg, and (e) Inversed pole figure color map and extrusion direction (ED). Boundary misorientation indicated as follows: white lines 1–5°, blue lines: 5–15°, thin black lines: 15–30°, and thick black lines > 30°.	140
Fig. 6.3 The evolution of subgrain size with an increase of (a) Cu and (b) Mg contents.	142
Fig. 6.4 Individual influences of selected alloying elements on electrical conductivity: (a)	

Cu and (b) Mg	143
Fig. 6.5 Correlation between calculated and experimentally measured EC.	145
Fig. 6.6 Individual influences of selected chemical elements on UTS: (a) Cu, (b) Mg, and (c) Fe with a linear relationship.....	147
Fig. 6.7 Correlation between calculated and experimentally measured UTS.....	148
Fig. 6.8 EC and UTS profile of the alloys with different Cu and Mg additions. Arrows show the increasing Cu and Mg additions to their corresponding regions.	149
Fig. 6.9 Typical compressive creep curves of Al–0.3Fe alloys with different Cu contents, tested at 100 °C and applied load of 69 MPa: (a) creep strain (ϵ) and (b) instantaneous creep rate ($\dot{\epsilon}$).....	151
Fig. 6.10 Evolution of the primary creep strain (ϵ_p) (a) and minimum creep rate $\dot{\epsilon}_m$ (b) as a function of Cu contents.....	152
Fig. 6.11 Typical compressive creep curves of Al–0.3Fe–0.18Cu alloys with different Mg contents, tested at 100 °C and applied load of 69 MPa: (a) creep strain (ϵ) and (b) instantaneous creep rate ($\dot{\epsilon}$).	153
Fig. 6.12 Evolution of the primary creep strain (ϵ_p) (a) and minimum creep rate $\dot{\epsilon}_m$ (b) as a function of Mg contents.....	154

CHAPTER 1
INTRODUCTION

Chapter 1

Introduction

1.1 Definition of problems

Aluminum conductors are widely used in building, aerospace, telephone lines, power grids and magnet winding [1-3]. Due to a much higher conductivity to weight ratio than copper and relatively lower price, they have become an attractive candidate for replacing copper conductors in electrical power industry, as shown in Fig. 1.1. As an electrical conductor material, it is necessary to satisfy the full requirements for high electrical conductivity, mechanical properties and sufficient creep resistance at an operation temperature up to 100 °C [4].



Fig. 1.1 Cable products available in feeder sizes only.

Among the aluminum conductor alloys, 8xxx aluminum alloys are the most commercialized conductor alloys used in the electrical distribution within buildings. They

are firstly developed to replace AA1350 alloys for the overhead electrical transmission [5]. In 8xxx alloys, alloying additives, such as Fe, Mg and Cu (in small amounts) are added, as listed in Table 1.1, making it possible to obtain a material with great microstructural stability, excellent comprehensive performance and creep resistance and not subject to the junction failure that occurred to AA1350 aluminum conductors [6-9].

Table 1.1 Chemical composition limits for AA1350 and AA8xxx aluminum alloy as electrical conductors [10,11].

Alloy	Compositions, wt.%						
	Si	Fe	Cu	Mg	Zn	B	Each
AA1350	0.10	0.40	0.05	0.001	0.05	...	0.03
AA8017	0.10	0.55-0.8	0.10-0.20	0.01-0.05	0.05	0.04	0.03 ^A
AA8030	0.10	0.30-0.8	0.15-0.30	0.05	0.05	0.001-0.04	0.03
AA8076	0.10	0.6-0.9	0.04	0.08-0.22	0.05	0.04	0.03
AA8130	0.15 ^B	0.40-1.0 ^B	0.05-0.15	...	0.10	...	0.03
AA8176	0.03-0.15	0.40-1.0	0.10	...	0.05 ^C
AA8177	0.10	0.25-0.45	0.04	0.04-0.12	0.05	0.04	0.03

^A 0.003 max lithium

^B 1.0 max silicon and iron

^C 0.03 max gallium

To improve the tensile strength and simultaneously to maintain excellent electrical property, the main alloying elements, Fe, Cu and Mg were added in 8xxx aluminum alloys [6-8]. Fe is added in this alloy to improve microstructural stability due to the presence of small insoluble dispersion eutectic particles which were formed during solidification and fabrication process [5,11], and to enhance mechanical properties through particle dispersion strengthening [12]. However, it has a detrimental effect on the casting speed due to the

lower heat extraction rate upon casting, leading to the low productivity. So, it would be preferable to keep lower Fe content and compensate properties by increasing concentrations of other elements. Small amount of Cu and Mg are known to improve the mechanical properties due to the solid solution strengthening [13,14], but the introduction of Cu and Mg will reduce the electrical conductivity [15]. Thus, it would be preferable to quantitatively understand the effects of Cu and Mg on mechanical properties and on electrical conductivity to balance the properties for their alloy development.

On the other hand, creep resistance is one of the most important properties during the industrial application of electrical conductor [9,16,17]. Gradual loosening at the terminals occurred due to poor creep resistance leads to some serious electrical fires in aluminum conductors [7-9]. The creep resistance could be improved by particles and solute additions, which lead to decreasing grain boundary mobility, impeding dislocation movement and accelerating dislocation multiplication [18-21]. The presence of Fe-containing particles has a strong effect in improving the creep resistance of aluminum alloys by impeding dislocation glide and climb and stabilizing the grain and substructure [12,25]. On the other hand, Fe solutes in commercial aluminum could be greatly increasing the creep resistance of aluminum alloys due to the low diffusion rate, while Cu and Mg could increase the creep resistance due to strong solute drag effect and clustering effect [21-24].

Though some works on electrical conductivity and mechanical properties have been performed, a systematic investigation of alloying elements (Fe, Cu and Mg) on the electrical

conductivity and mechanical properties of 8xxx aluminum alloy conductors has rarely been reported. Moreover, the study on effect of small amount of Cu and Mg on the creep behavior of 8xxx aluminum conductor alloys at relatively low temperature ($T < 0.5 T_m$, where T_m is the melting point) has not been found in the literature. Furthermore, the poor understand of alloying elements on the microstructure evolution and their inference on material properties of aluminum conductor alloys seriously limit the ability for the alloy design and development. Therefore, this present study is aimed to investigate the effect of alloying elements (Fe, Cu and Mg) on microstructure and properties of 8xxx aluminum alloys to provide alternative alloy chemical compositions with a good combination of high productivity, enhanced electrical conductivity, good mechanical and creep properties.

1.2 Objectives

The goal of the present work mainly consists of three parts and the specific objectives are proposed as follows:

Part 1. Investigating the effect of Fe on microstructure and properties of 8xxx aluminum conductor alloys

1. Studying the evolution of as-cast microstructure of the 8xxx aluminum alloys with a series of Fe additions (0.3 wt.% to 0.7 wt.%).
2. Investigating the tensile strength and electrical conductivity of the 8xxx aluminum alloys with various Fe additions.

-
3. Constitutively analyzing the relationship between the initial microstructure and the tensile and electrical properties.
 4. Studying the effect of Fe contents on the creep resistance of 8xxx aluminum conductor alloys at 100 °C.

Part 2. Exploring the role of Fe solute and Fe-containing particles on the creep behavior of 8xxx aluminum conductor alloys

1. Studying the microstructural evolution of the 8xxx aluminum alloys with two thermal holding treatments.
2. Investigating the effect of Fe solutes and Fe particles on the creep properties of the 8xxx aluminum alloys at elevated temperatures.
3. Discovering the relationship of Fe solutes and Fe particles with creep resistance at various temperatures.
4. Understanding the creep mechanisms at the studied temperature range.

Part 3. Studying the effect of Cu and Mg additions on the microstructure and properties of 8xxx aluminum conductor alloys.

1. Studying the microstructural evolution of the 8xxx aluminum alloys with a series of Cu and Mg additions during the hot extrusion.
2. Quantitatively investigating the effect of various Cu and Mg additions on tensile

strength and electrical conductivity of the 8xxx aluminum alloys.

3. Drawing the relationship diagram between the ultimate tensile strength and the electrical conductivity.
4. Investigating the effect of Cu and Mg additions on the compressive creep resistance.

References

- [1] V.M. Sizyakov, V.Y. Bazhin, A.A. Vlasov, *Metallurgist* 54 (2010) 409-414.
- [2] T. Shikagawa, G. Itoh, S. Suzuki, H. Kuroda, T. Horikoshi, *Aluminium Alloys* 519-521 (2006) 515-518.
- [3] L. Pan, B. Bourassa, X.G. Chen, *Aluminium Alloys 2014 - ICAA14* 794-796 (2014) 1121-1126.
- [4] K.W. Barber, K.J. Callaghan, *IEEE T. Power Deliver.* 10 (1995) 403-409.
- [5] C. Olin, in: U.S.P. 3711339 (Ed.), US, 1973.
- [6] J. Rabinow, *Nat. Bur. Stand. (US) NBSIR* (1978) 78-1507
- [7] J. Rabinow, Report for the US. Consumer Product Safety Commission, 1974.
- [8] W.J.a.B. Meese, R., *Nat. Bur. Stand. (U.S.), Bldg* (1977).
- [9] D. Newbury, S. Greenwald, *J. Res. Nat. Bur. Stand.* 85 (1980) 429-440.
- [10] ASM International. Handbook Committee., *ASM handbook Volume 2, Nonferrous Alloys and Special-Purpose Materials*, 10th ed., ASM International, Materials Park, OH, 1992.
- [11] ASTM. B800-05, Standard Specification for 8000 Series Aluminum Alloy Wire for Electrical Purposes-Annealed and Intermediate, ASTM Internationa, West Conshohocken, PA, 2005.
- [12] H.J. Mcqueen, E.H. Chia, E.A. Starke, *JOM* 38 (1986) 19-24.
- [13] H.J. Mcqueen, K. Conrod, G. Avramovic-cingara, *Can. Metall. Quart.* 32 (1993) 375-386.
- [14] R.W. Cahn, P. Haasen, *Physical metallurgy*, 4th, rev. and enhanced ed., North-Holland,

Amsterdam; New York, 1996.

[15] G.E. Dieter, *Mechanical metallurgy*, 3rd ed., McGraw-Hill, New York, 1986.

[16] O. Ryen, O. Nijs, E. Sjolander, B. Holmedal, H.E. Ekstrom, E. Nes, *Metall. Mater. Trans. A* 37A (2006) 1999-2006.

[17] D.E. Newbury, *Anal. Chem.* 54 (1982) A059-A064.

[18] E. Kandare, S. Feih, A. Kootsookos, Z. Mathys, B.Y. Lattimer, A.P. Mouritz, *Mater. Sci. Eng. A* 527 (2010) 1185-1193.

[19] T. Hasegawa, T. Miura, T. Takahashi, T. Yakou, *ISIJ Int.* 32 (1992) 902-908.

[20] P.K. Chaudhury, F.A. Mohamed, *Mater. Sci. Eng. A* 101 (1988) 13-23.

[21] N.N. Du, Y. Qi, P.E. Krajewski, A.F. Bower, *Metall. Mater. Trans. A* 42A (2011) 651-659.

[22] X. Sauvage, N. Enikeev, R. Valiev, Y. Nasedkina, M. Murashkin, *Acta Mater.* 72 (2014) 125-136.

[23] P.K. Chaudhury, K.T. Park, F.A. Mohamed, *Metall. Mater. Trans. A* 25 (1994) 2391-2401.

[24] O.D. Sherby, A. Goldberg, O.A. Ruano, *Philos. Mag.* 84 (2004) 2417-2434.

[25] R.N. Lumley, A.J. Morton, I.J. Polmear, *Acta Mater.* 50 (2002) 3597-3608.

CHAPTER 2

LITERATURE REVIEW

Chapter 2

Literature review

2.1 Introduction of 8xxx aluminum conductor alloys

2.1.1 Industrial application of 8xxx aluminum conductor alloys

Of all the conducting elements, aluminum and copper are often used as current carrying conductors due to their conductivity and mechanical properties. Although electrical conductivity of aluminum is somewhat less than that of copper, has long been used as an electrical conductor in view of its light weight and lower price. The first use of aluminum for electrical purposes was invented in Britain in 1876. And it entered service in transmission lines in 1909. In the US, utilities have used Al wires for over 100 years.

However, until 1965, the AA1350 aluminum conductor alloy began to be widely used for residential buildings. This alloy has a conductivity of 61 %IACS compared to 103 %IACS for pure copper but a density of only 30%, so that it is a far more effective medium than copper for conductors that have to be supported on overhead line structures. Meanwhile, widespread cost that the price of copper was very high made the installation of aluminum conductors a very attractive alternative. However, several issues were encountered with the use of AA1350 aluminum alloy conductor in household applications. Some junction failures occurred due to gradual loosening at the terminals that caused damage and fires [1-3].

Therefore, a new series of alloys, namely 8xxx aluminum alloy with 0.3–0.9 wt.% Fe which was registered in Aluminum Association to replace AA1350 alloys for the overhead electrical transmission [4]. The comprehensive performance, and high creep resistance of this type of conductors when installed properly can be just as safe as copper. The high extent Fe in these alloys are advantageous when the wire is batch annealed at 200–250 °C. However, it is bad for the flash annealing when the annealing conducted at higher temperature for shorter times.

2.1.2 Fabrication process of 8xxx aluminum conductor alloys

The product of 8xxx conductor is fabricated by Properzi continuous casting methods [5]. When the billet is continuously rolled to a rod with total strain of 4.3 (98.6%), the subgrain were formed and the size of subgrains greatly decreased during the process (*i.e.*, for Al–0.65 wt.% Fe alloys, after 3 passes and 13 passes, the temperature T declines from 485 to 180 °C and subgrains decrease from 6.0 μm to 1.1 μm [6]). This heavy reduction breaks the eutectic compounds into segments and distributed throughout the aluminum matrix. Without an intermediate annealing treatment in order to retain the substructure, the rolled rod is transferred directly to wire drawing. At completion the wire is given a recovery annealing treatment which raises electrical conductivity and ductility without greatly changing the subgrain size.

In order to have better combination of mechanical and electrical properties in 8xxx aluminum conductors, processing parameters are investigated including extrusion ratio, homogenization and novel manufacturing process. Guo *et al.* [7] studied the influence of the extrusion ratio on the AA8030 aluminum alloys rods, and obtained the best ratio of 13, which showed the maximum electrical conductivity of 60.8 %IACS. Engler *et al.* [8] investigated the evolution of microstructure during homogenization and subsequent rolling and back-annealing for the Al–Fe–Mn alloy AA8006 to understand the underlying mechanism that control the recrystallization behavior of the alloys. In the research of Zhang *et al.* [9], it is found that Al–0.7 wt.% Fe–0.24 wt.% Cu alloy manufactured using horizontal continuous casting and subsequent continuous forming method showed well combined mechanical properties and electrical conductivity; in addition, a better creep resistance under condition of 90 °C and 76 MPa is obtained.

2.1.3 Alloying elements in 8xxx aluminum conductor alloys

In general, pure aluminum is weak and the aluminum conductors in transition lines have been developed by addition of other elements to improve the distribution and morphology of the stabilizing particles to improve the comprehensive properties. The addition of alloying additives, such as Fe, Cu, and Mg, was added in 8xxx aluminum alloys. These additions in aluminum may create a solid solution or individual phases, which will be discussed in the following.

Fe

The solid solubility of Fe in aluminum is very low (0.054 wt.% at 650 °C and about 0.005 wt.% at 450 °C [11]), and therefore most of Fe combines with both aluminum and silicon to form secondary intermetallic phase, such as Al_mFe , FeAl_3 , Al_6Fe , and $\alpha\text{-AlFeSi}$ ($\text{Al}_8\text{Fe}_2\text{Si}$) [10-12]. The typical morphologies for four different frequent intermetallics are shown in Fig. 2.1 [12]. Besides, the phase transition occurred under certain conditions. Shakiba *et al.* [12] has indicated that the phase transformation from the metastable Al_mFe or $\alpha\text{-AlFeSi}$ phase to the FeAl_3 equilibrium phase occurred during the homogenization treatment in the temperature range of 550 to 630 °C.

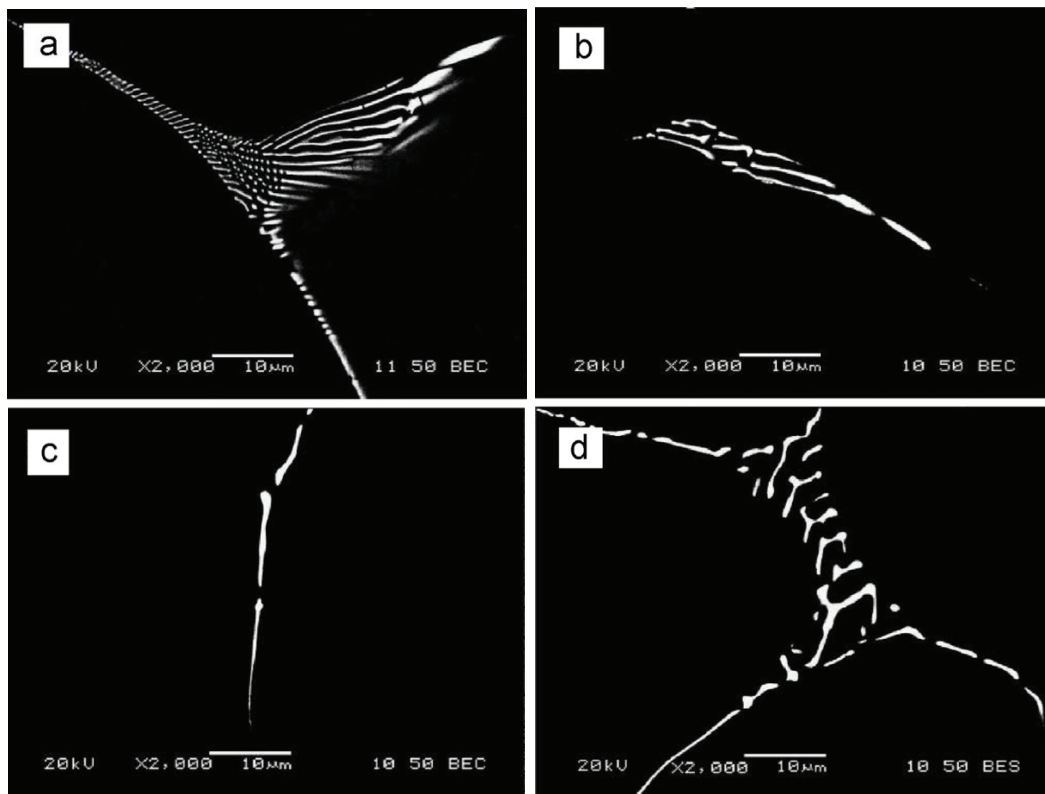


Fig. 2.1 Backscattered electron image for four different types of frequent Fe-rich particles: (a) Al_mFe , (b) Al_6Fe , (c) FeAl_3 and (d) $\alpha\text{-AlFeSi}$ ($\text{Al}_8\text{Fe}_2\text{Si}$).

During the aluminum conductors fabrication process, the eutectic network was broken up into small particles and uniformly distributed through the matrix [6]. The metastable Fe-bearing intermetallic compound was reported to be FeAl_3 or Al_6Fe [6,13], with morphology in Fig. 2.2(a). Besides, these coarse dispersed particles could pin on the subgrain as shown in Fig. 2.2(b), which retard the dynamic recovery in aluminum alloys [6,14]. The particle strengthening and substructure strengthening due to Fe greatly increased the stress in 8xxx aluminum alloys.

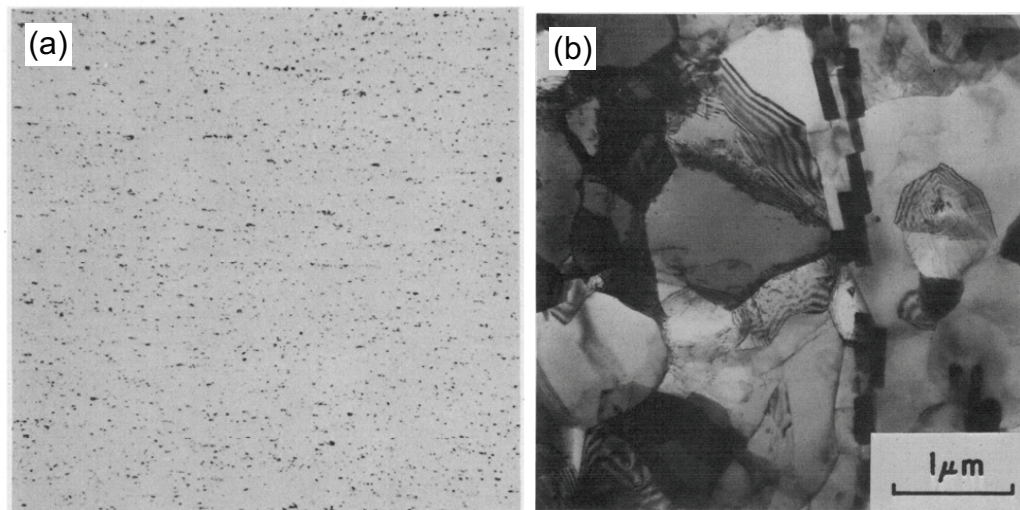


Fig. 2.2 Optical micrograph (a) and TEM image (b) of Al–0.75 wt.% Fe–0.15 wt.% Mg alloy rods continuously fabricated [13] (magnification 500 times for optical micrograph).

Cu

The solid solubility of Cu in aluminum is much higher than Fe (5.7 wt.% at 548.2 °C and about 3.5 wt.% at 450 °C [15]). It is reported that small addition of Cu in solid solution could result in the fine substructure during the hot deformation process due to the lower diffusion rate [16]. Small amount of Cu in solid solution resulted in retardation of dislocation movement and enhanced the rate of dislocation multiplication.

On the other hand, Cu is often added to improve the strength of aluminum alloys. However, addition of Cu more than 1.1 wt.% results in the formation of coarse intermetallics during casting, which causes the corrosion. In addition, addition of copper causes greatly decreasing of electrical conductivity. Consequently, it is favourable to have a proper copper content by balancing the strength and electrical conductivity.

Mg

Mg has a very high solid solution in aluminum. At room temperature, aluminum can dissolve up to 1.7 wt.% Mg at equilibrium and the solubility increased up to 14.9 wt.% at 450 °C. Due to the relatively high diffusion rate, Mg in solid solution state could form clusters, which could significantly increase the stress of aluminum alloys [17].

Besides, Mg is often added to improve the mechanical properties of aluminum alloys. However, addition of Mg causes great decrement in electrical conductivity. Consequently, there is a trade-off between the mechanical property and electrical conductivity.

2.1.4 Properties requirements for aluminum conductors

The aluminum conductors must possess to be safely developed to have a good combination of high electrical conductivity, high mechanical properties, and high creep resistance to stress relaxation for contact stability [1,6,18,19].

Firstly, high electrical conductivity is mostly desirable for conductors. Low electrical conductivity will cause great energy losses in the application and lead to temperature problems. The minimum requirement for electrical conductivity is 61.0 %IACS for applications in building conductors [20].

Besides, the aluminum conductor alloys should have sufficient mechanical properties to meet the minimum requirements imposed by service conditions in electrical applications. In general, a minimum ultimate tensile strength of 103 MPa in straining hardening and partially annealing state is needed for aluminum conductors [20]. Table 2.1 shows the comparison of mechanical properties and electrical conductivity of some typical aluminum conductor alloys [5].

Table 2.1 Comparison of physical and mechanical properties of some typical aluminum conductor alloys.

Alloys	UTS (MPa)	YS (MPa)	EL %	Electrical conductivity (%IACS)
Al-0.5Fe-0.5Co	145	120	18	59.8
Al-0.65Fe	125	110	20	60.4
AA1350	110	96	15	61.9

Another property that needed for the application of aluminum conductor is high creep resistance [21]. Creep is a permanent deformation resulting from an applied stress in a material over a long duration of time. In practice, stress relaxation by creep occurred at operation temperature up to 100 °C allows subsequent decrease in contact pressure [19]. This results in gradually loosening at terminals, and causes an increase of the constriction resistance [22], which in turn increase the temperature due to the increase of resistance. The joint force decreases significantly and further leads to increase in joint resistance [21]. Though creep property is very important for aluminum conductors, to the author's knowledge, limited reference is available for systematically study on the creep properties of 8xxx aluminum conductor alloys.

2.2 Electrical properties of 8xxx aluminum conductor alloys

In the development of suitable conductor alloys, electrical conductivity is the primary criterion to be considered. Electrical conductivity is the ability of a material to measure how well it can carry a flow of electrons. The electrical conductivity of extreme purity aluminum (99.99%) at room temperature is 64.94% of electrical resistivity annealed copper based on the international standard (%IACS) [23]. The electrical conductivity of the annealed copper (5.8001×10^7 S/m) is defined to be 100 %IACS at 20 °C.

The unit of electrical conductivity is S/m, however, for convenience, electrical conductivity is frequently expressed in terms of %IACS. Conductivity values in S/m can be

converted to %IACS by multiplying the conductivity value by 1.7241×10^{-6} as shown in the following equation:

$$\%IACS = 1.7241 \times 10^{-6} \text{ S/m} \dots\dots\dots (\text{Eq. 2.1})$$

Electrical conductivity of aluminum strongly depends on quantity of impurities and metallic additions [23-26]. The solute contents in aluminum matrix could enhance scattering of free electrons by the creation of defects and dislocations, which reduce the electrical conductivity [27]. According to I. N Fridlyander [23], impurities have negative influence on electrical conductivity of aluminum, which depends on quantity of solute and metallic additions. It can be arranged in the following order: Cr, V, Mn, Ti, Mg, Ag, Cu, Zn, Si, Fe, Ni. A summary of the maximum solubility of various elements in aluminum is shown in Table 2.2, together with the average increase in resistivity per 1% of the element in solution and out solution [28]. The formation of dispersoids or precipices had less effect in decreasing electrical conductivity than that of solute.

Table 2.2 Effect of alloying elements in and out of the solid solution on the resistivity of aluminum.

Elements	Maximum solubility in Al, wt.%	Average increase in resistivity, wt.%, $\mu\Omega\cdot\text{cm}$	
		In Solution	Out of Solution
Cr	0.77	4.00	0.18
Cu	5.65	0.344	0.30
Fe	0.052	2.56	0.058
Li	4.0	3.31	0.68
Mg	14.9	0.54	0.22
Ni	0.05	0.81	0.061
Si	1.65	1.02	0.088
Ti	1.0	2.88	0.12
V	0.5	3.58	0.28
Zn	82.8	0.094	0.023
Zr	0.28	1.74	0.044

Note: Addition to high purity Al base resistivity of $2.71 \mu\Omega\cdot\text{cm}$ at 25°C

Besides, the influence of alloying elements on electrical conductivity can be quantitatively determined accordingly to the Matthiessen rule [29]. The relationship between EC and the concentration of alloying elements in solid solution (wt.%) can be expressed as follows:

$$\frac{1}{EC} = \rho_b + \sum_i \rho_i C_i + \rho_p f_p \dots\dots\dots \text{(Eq. 2.2)}$$

where ρ_b is resistivity of the base alloy, $\sum_i \rho_i C_i$ is the sum of the resistivity contributions from the various solution additions, *i.e.* ρ_i is the resistivity parameter and C_i is the concentration of the i^{th} solute, ρ_p is the resistivity parameter of the particles to resistivity and f_p is the particles volume fraction. In as-homogenized state, the relationship between the

electrical conductivity (EC, S/m) and the concentration of alloying elements in solid solution can be expressed as follows [30,31]:

$$\frac{1}{EC} = 0.0267 + 0.0032Fe_{ss} + 0.0068Si_{ss} + 0.003Mg_{ss} + 0.0021Particle\% \quad \dots\dots\dots \text{(Eq. 2.3)}$$

where, Fe_{ss} , Si_{ss} , and Mg_{ss} are the weight percentages of these elements in solid solution, and the last part in this equation is the total volume fraction of particles which is an estimation of the particle contribution to the electrical resistivity. However, the parameter for the particle contribution would be variable, which depends on the shape and size of the particles in the alloys [26].

2.3 Mechanical properties of 8xxx aluminum conductor alloys

For aluminum conductors, it is necessary to have high mechanical properties to stress relaxation for contact stability, and will not be susceptible to oxide growth [32]. To effectively improve mechanical properties of an aluminum conductor, the strengthening mechanisms must be applied, which has the optimum ratio of increase in strength to resistivity ($\Delta\sigma/\Delta\rho$), as indicated in Table 2.3. Substructure strengthening, solid solution strengthening and particle strengthening could be the effectively strengthening mechanism for aluminum alloys and would be discussed below.

Table 2.3 Comparative effects of different mechanisms on strength and resistivity in aluminum [33].

	Mechanism	Calculated or measured at room temp.	Property		$\Delta\sigma/\Delta\rho$ (MPa/ $\mu\Omega$.cm)	
			Resistivity ($\mu\Omega$.cm)	Strength (MPa)		
Substructure	Grain Boundaries	$D = 100\mu$	nil	8.8	Very high	
	Dislocations	$n = 2 \times 10^{10} \text{ mm}^{-2}$	3	20	7	
		$n = 2 \times 10^6 \text{ mm}^{-2}$	3×10^{-3}	2	70	
		$n = 2 \times 10^4 \text{ mm}^{-2}$	3×10^{-5}	.02	700	
	Cell & Subgrain boundaries	$\theta = 10^\circ$ $d = 2\mu(m=-1/2)$	6×10^{-5}	30	5×10^5	
$\theta = 10^\circ$ $d = 2\mu(m=-1)$		6×10^{-5}	36	6×10^5		
Alloying	Solid Solution	Ag	26	390	15	
		Be	0.07	4.3	61	
		Cd	0.47	6.3	13	
		Ce	7×10^{-4}	0.90	1300	
		Cu	1.8	160	89	
		Fe	0.05	2.5	51	
		Ga	1.5	93	62	
		Ge	1.6	43.9	27.4	
		Mg	9.9	371	37.4	
		Mn	5.6	26	4.7	
		Ni	0.10	2	20	
		Si	0.8	25	31	
		Zn	15.0	294	20	
		V	1.2	8.1	7	
	Mg ₂ Si	4.21	74	17.5		
	Precipitation Hardening (over values in the pure metal)					
	Deformable particles (peak hardness)					
	Ag14%, 250°C, 10hr	6.5	400	62		
	Mg ₂ Si, 175°C, 8hr	1.4	284	203		
	Cu 1.7At%, 130°C -60°C, 1000 hr	0.7	88	125		
Non-deformable particles (Orowan)(over values in the pure metal)						
	Ag14 at%, 50°C, 100hr	3.35	70	21		
	Mg ₂ Si, 175°C, 9 days	1.3	170	130		

*** Calculated at the solubility limit
 θ = subgrain misorientation

2.3.1 Substructure strengthening

The substructure of an aluminum alloy consists of a mixture of single dislocations and dislocation arrangements, which is formed as a result of recovery [34]. During deformation, the mobile dislocations interact with the substructure and the mobility of the dislocations is reduced. The slip length (*i.e.*, the average distance of a mobile dislocation travels from the source to becoming stored in the substructure) depends on these interactions [35]. The fine substructure will act as barriers to slip, and results in a reduced mean free path for dislocation movement. The effect of grain boundaries on the room temperature strength of metals can be described by the relationship as follows [36]:

$$\sigma_y = \sigma_0 + kd_s^{-1} \dots\dots\dots \text{(Eq. 2.4)}$$

where σ_0 is the yield strength of a substructure free metal with the same grain size, k is a constant that is related to the strength of subboundary, d_s is the subgrain diameter. At elevated temperatures, the substructure strengthening may be described by a relationship as follows:

$$\sigma_y = \sigma_0 + kd_s^{-1/2} \dots\dots\dots \text{(Eq. 2.5)}$$

Rack and Cohen [37] have shown this to be the case for heavily deformed Fe alloys. Data from the review paper of Mcelroy and Szkopiak [38] on aluminum, iron, and iron-based alloys also correlate well with $d_s^{-1/2}$.

Generally, there are two ways in which alloying additions may benefit for the

development and stabilization of a fine substructure, which would be the alloying elements in solid solution state and the formation of particles. Firstly, the alloying elements in solution could result in a retardation of dislocation movement, an enhanced rate of dislocation multiplication and a restriction of dynamic softening process [16,39,40]. Shakiba *et al.* [16] investigated the hot deformation behavior of Al–Fe–Si alloys containing 0.05–0.31 wt.% Cu at a temperature range of 440–550 °C, and found that addition of Cu retarded the dynamic recovery and decreased the subgrain size and mean misorientation angle of the grain boundaries. Furu *et al.* [39] showed that an addition of 1% Mg produces a solute drag effect during the hot deformation of aluminum resulting in a slightly smaller subgrain size. Shi *et al.* [40] studied the hot deformation behavior of 7150 aluminum alloys containing (0.01–0.19 wt.%) vanadium at various temperatures (300–450 °C) and strain rates (0.001–10 s⁻¹), and pointed out that as little as 0.03 wt.% vanadium could significantly reduce the subgrain size during the hot deformation process due to the low diffusion rate of vanadium solute atoms. Besides, addition of alloying elements in solid solution was also helpful in the generation of dislocations, lead to a high dislocation density for given amount of deformation. The high dislocation density would accelerate the cell formation and produce a fine substructure [34].

Secondly, the formation of particles due to alloy additions would benefit for the development and stabilization of a fine substructure due to the strong pinning effect on the dislocation motion and migration of grain boundaries [6,14,41-43]. In these materials, the

subgrain size is a function of the particle spacing [42]. Shakiba *et al.* [14] studied the hot deformation behavior of Al–Fe–Si alloys containing various amounts of Fe (0.1–0.7 wt.%) and Si (0.1–0.25 wt.%) at various temperatures (350–550 °C) and strain rates (0.01–10 s⁻¹), and found that with increasing of the Fe content dynamic recovery was greatly inhibited which is associated with a decrease in the subgrain size and mean misorientation angles. Fig. 2.3 shows an example that a large part of the intermetallic particles distribute on the subgrain boundaries, which increases the pinning effect on subgrain boundaries and hence enhances the subgrain stability [41].

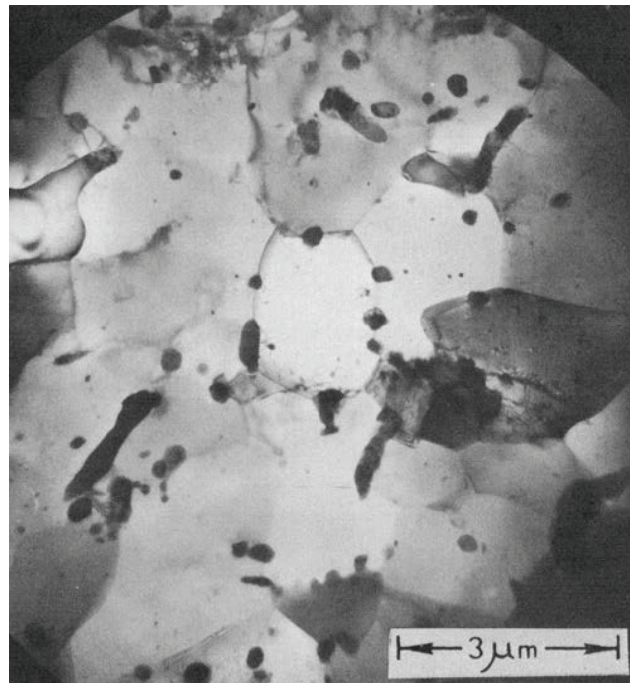


Fig. 2.3 TEM micrograph of Al–Fe–Mg alloys showing particles on sub-boundaries [41].

2.3.2 Solid solution strengthening

The introduction of foreign atoms into a crystal lattice invariably interfered the structure of the base metal increase the strength of the material [35]. Solid solution additions can be helpful by their effect on the stacking fault energy and the ability to tie up defects, thus hindering dislocation motion. The main strengthening mechanisms have been suggested as the elastic interaction due to the size misfit and the modulus misfit between the solute atoms and solvent atoms [44,45]. The size of the solute atom differs from the solvent atoms create a strain field, which will interact with dislocations and give rise to the energy. The modulus misfit is related to the difference in bond force between the solute atoms and the matrix atoms, which creates a soft or hard “spot” in the matrix and an interaction with the moving dislocation is occurred.

Previous work has been done on the solid solution hardening in aluminum alloys [35,45], and found that the strength is affected by the amount and type of alloy additives in aluminum matrix. The relationship between the flow stress and the alloy concentration is generally expressed as follows:

$$\sigma_{ss} = \sigma_b + HC^n \dots\dots\dots (Eq. 2.6)$$

where σ_b is the stress of the base alloy and H and n are constants. The value of n is reported in the range of 0.5–1.0 of pure fcc substitutional solid solutions [35].

In general, small amount of Cu and Mg was added in 8xxx aluminum alloys to increase

the strength by solid solution strengthening [17,35,46]. Addition of Cu and Mg has the high relative difference in atom size and shear modulus misfit with aluminum, as illustrated in Table 2.4, which cause a strong solid solution strengthening effect.

Table 2.4 Atomic radius, shear modulus and strengthening parameter H of Cu and Mg in aluminum [46].

Elements	H MPa (at.%) ⁻¹	Atomic radius r (Å)	Shear modulus G (GPa)
Al	-	1.43	26.2
Cu	119.8	1.28	48.3
Mg	69.4	1.60	17.0

Ryen *et al.* [35] reported that Mg in a solid solution give a nearly linear concentration dependence of strength for commercially pure aluminum alloys. Mamala and Sciezor [47] studied the effect of small amount of (0.1–0.6 wt.%) Cu and (0.3–0.9 wt.%) Mg on the Vickers hardness of aluminum alloys in as cast and heat treated tempers, and the results are summarized in Table 2.5.

Table 2.5 Estimated increase of aluminum hardness caused by 1% addition of Cu and Mg in different tempers.

Alloying elements	As cast, HV	Homogenized and fast cooled to water, HV	Homogenized, slow cooled and heated in 250°C, HV
Cu	18.6	17.0	16.2
Mg	18.3	10.4	8.3

2.3.3 Particle strengthening

A common classification of the different particles that may be present in aluminum alloys is roughly given as follows: (1) unshearable primary or constituent particles, which are formed during solidification, (2) unshearable dispersoids, which are formed during homogenization. The dispersoids impose a Zener drag on grain boundaries which implies that they prohibit recrystallization and grain growth, and (3) precipitates that are formed by solution heat-treatment followed by aging.

The materials in this work are of non-heat-treatable strengthened aluminum alloys and the most relevant part of particle strengthening is the unshearable primary or constituent particles. Heat treatment of such an alloy will generally not produce any strengthening precipitates as in the heat-treatable alloys. The contribution of unshearable particles to the strength of alloys can be evaluated by the Orowan mechanism, as shown in Fig. 2.4. A dislocation passing through two particles will bend initially. At stage 3, it has reached to critical curvature, and when the segments meet on the other side they have opposite signs and leave a dislocation loop around each other (stage 4).

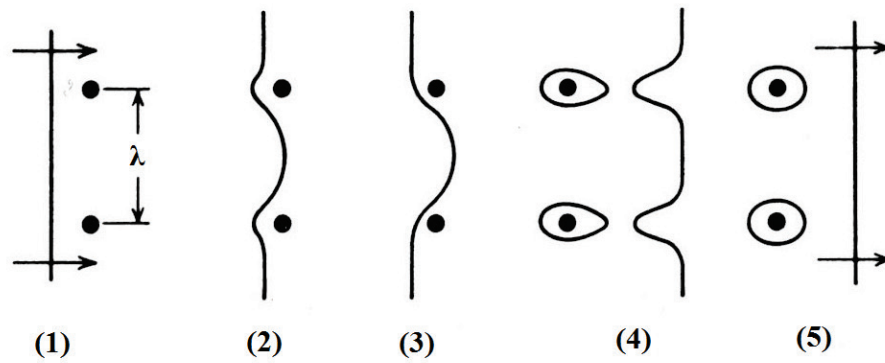


Fig. 2.4 Sketch of a dislocation passing two hard particles, based on the Orowan mechanism [44].

The strengthening due to Orowan dislocation looping is given by an equation as follows [42]:

$$\Delta\sigma_{or} = M \frac{0.4}{\pi} \frac{Gb}{\sqrt{1-\nu}} \frac{1}{\lambda} \ln\left(\frac{2r}{b}\right) \dots\dots\dots (\text{Eq. 2.7})$$

where $\nu = 0.34$ is the matrix Poisson's ration and λ is the inter-precipitate distance, which is calculated according to the equation [48]:

$$\lambda = d \left(\sqrt{\frac{\pi}{4f}} - 1 \right) \dots\dots\dots (\text{Eq. 2.8})$$

where f is the volume fraction of the particles and d is the average particle diameter.

Generally, alloying elements (mainly Fe in this study) in 8xxx aluminum could form dispersoids due to its low solubility [11], which would cause particle strengthening. Addition of Fe could improve the mechanical properties of 8xxx aluminum alloys due to the

formation of Fe-containing particles [18,36,49,50]. Jablonski *et al.* [49] have shown that an addition of 0.5 wt.% Fe in AA8176 aluminum alloys resulted in a great improvement in ultimate tensile strength under drawing condition without significant deterioration on its electrical properties.

2.4 Creep behaviour of aluminum conductor alloys

At room temperature, most metals deform in a way that depends on stress but not on time. As the temperature increased, low loads can give permanent progressive deformation, which is termed creep [44]. Due to the lower creep resistance, the application of aluminum conductors is greatly restricted. In the following session, the creep phenomenon, characterization of creep properties, possible creep mechanisms occurred in aluminum conductor alloys and creep behavior in aluminum conductors will be discussed.

2.4.1 Creep phenomenon

The behavior of aluminum alloys at elevated temperatures is primarily controlled by a phenomenon termed creep. Creep is a permanent deformation of material at constant stress and temperature. The typical shape of a creep curve can be represented as shown in Fig. 2.5. The slope of creep curve is referred to as the creep rate ($\dot{\epsilon} = d\epsilon / dt$), which indicates the elongation speed of the specimen with time [44]. When loads are applied, an instantaneous deformation (ϵ_0) occurs as a combination of the elastic and plastic response.

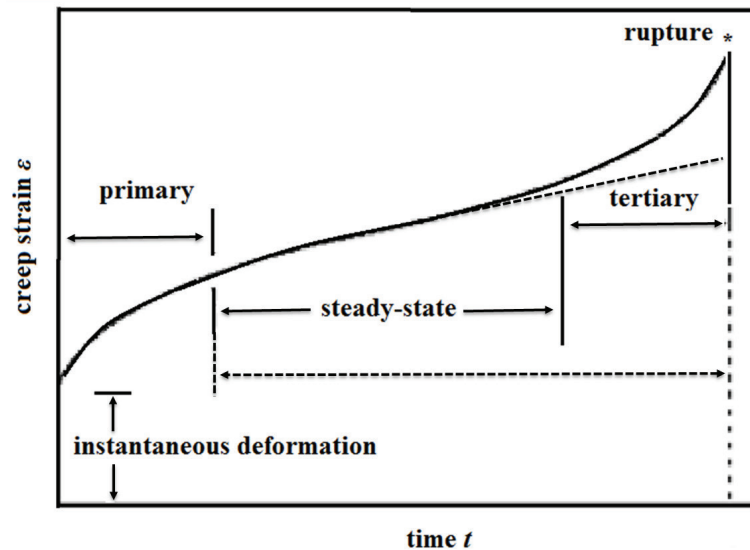


Fig. 2.5 Typical creep curve showing the three stages of creep.

The dotted line shown in the figure is for the compression creep curves.

It is generally considered that there are three different regions of creep in the unreinforced alloys [51]. The primary creep region that occurs upon initial loading exhibits a very high creep rate as the material elastically and plastically responds to the applied load. As the material deforms, the material is strengthened through strain hardening, leading to the decreasing creep rate. This stage is the dominant form of creep observed at low stresses and at low temperatures relative to the melting point of the material [44,51-53].

Primary creep gradually transitions into the steady-state creep stage (or minimum creep stage) with increase of time. During the steady-state creep, the creep rate changes little with time under a constant stress due to an equilibrium between recovery and hardening [54]. In an ideal material, the hardening rate is exactly proportional to the recovery rate, and the steady-state creep rate can be described by the relationship [55]

$$\dot{\epsilon} = \frac{r}{h} \dots\dots\dots (Eq. 2.9)$$

where h is the hardening rate and r is the recovery rate. In reality, some creep deformations do not exhibit a well-defined steady-state stage. Instead, the material will demonstrate a continuously decreasing creep rate with time, which is more suitable to be defined as a quasi-steady-state stage [56]. In these cases, the quasi-steady-state creep curves can be assumed to be linear decrease with increase of time for the purpose of conventional creep analysis with little impact on the quality of the subsequent results [57,58]. The steady-state creep region dominates most of the time of the test, especially during long time creep tests at low temperature and stress. Therefore, the steady-state creep rate is one of the most important design parameters derived from the creep curve for the design of components.

As creep continuing, the steady-state creep transitions into the third stage, typically identified as a tertiary creep (in tension) [51]. Continuous deformation produces voids or internal cracks which in turn decrease the cross-section (necking) and increase the stress. This accelerates the creep rate as shown in the tertiary stage of the creep curve in Fig. 2.5. The tertiary stage is mainly observed at high temperatures and high stresses creep tests. This region is always very short and is the final stage of creep before rupture occurs [54,59]. However, in compression creep curves, there is no such necking as occurred in tension creep, due to the geometric effect that the sample cross-section will get larger with increased strain [58,60]. Thus, the steady-state creep stage dominated during compression creep. As shown

in Fig. 2.5 (dotted lines), the compressive creep curves can be generally divided into two different stages, and no tertiary creep was observed.

2.4.2 Characterizations of creep properties

Creep deformation has been shown to be a strong function of stress, temperature and microstructures [51,61]. Garodo *et al.* [51,58,62] have proposed several forms of equations to describe the total creep strain $\varepsilon(t)$ during the creep test. In these equations the total strain and time dependent creep rates are summed. In cases where the creep strain and temperature are lower, the creep strain can be expressed by [62]

$$\varepsilon(t) = \left(\frac{kT}{\lambda}\right) \ln\left(1 + \frac{t}{\tau}\right) \dots\dots\dots \text{(Eq. 2.10)}$$

where λ and τ are constant, T is experimental temperature. Parameters kT/λ and τ are determined by experimental condition. For this research, the more attention is paid to the minimum creep ($\dot{\varepsilon}_m$), which is given by a simple power law:

$$\dot{\varepsilon}_m = A_a \left(\frac{\sigma}{G}\right)^{n_a} \exp\left(-\frac{Q_a}{RT}\right) \dots\dots\dots \text{(Eq. 2.11)}$$

where A_a is a constant for all stresses and temperatures, σ is the applied stress, G is the shear modulus, n_a is the apparent stress exponent, Q_a is the apparent activation energy for creep, R is the gas constant and T is absolute temperature. The shear modulus is temperature dependent and calculated from the equation (given as $G = 25.4 [1 - 0.5 (T - 300) / 933]$ with GPa unites) [48]. Under the fixed constant in temperature, the stress exponent n_a can be

calculated according to the following equation:

$$n_a = \partial \ln \dot{\epsilon}_m / \partial \ln \sigma \dots\dots\dots (\text{Eq. 2.12})$$

The activation energy Q_a can be measured by the temperature-cycling method [63]. In this method, a specimen was subjected to a number of rapid changes in temperature while under constant stress. The apparent activation energy was then determined after each temperature changes for the relation as follows:

$$Q_a = \frac{R \ln(\dot{\epsilon}_1 / \dot{\epsilon}_2)}{(T_1 - T_2) / T_1 T_2} \dots\dots\dots (\text{Eq. 2.13})$$

where $\dot{\epsilon}_1$ and $\dot{\epsilon}_2$ are the instantaneous creep rates immediately before and after the change in temperature from T_1 to T_2 . The activation energy is designated as the apparent energy for creep because it is empirically determined. Many different mechanisms may be interacting to cause the observed Q_a , but can not be separated based only on the experimental data.

The values of n_a can be used to estimate the creep mechanism in unreinforced aluminum alloys. However, in dispersion strengthened aluminum alloys, the apparent stress exponent (n_a) is higher and variable [64,65]. This behavior can be modeled by introducing in a threshold stress, σ_{th} , below which creep is not measurable experimentally [64]. After incorporating σ_{th} , Eq. 2.11 can be modified as follows [66,67]:

$$\dot{\epsilon}_m = A_a \left(\frac{\sigma - \sigma_{th}}{G} \right)^{n_t} \exp \left(- \frac{Q}{RT} \right) \dots\dots\dots (\text{Eq. 2.14})$$

The incorporation of a threshold stress into the analysis is usually effective in giving values of n_t that is similar to those obtained in the unreinforced matrix materials. According to the different n_a values, the creep mechanisms can be estimated. For the threshold stress, more discussion will be present on the following session.

2.4.3 Creep threshold stress

Unlike pure aluminum where dislocation-dislocation interactions and the development of a dislocation substructure are significant, in dispersoids strengthened aluminum alloys the dislocation - dispersoids interactions are of primary importance. It is common seen that the existence of unshearable particles inhibit the motion of moving dislocations, meanwhile solute atoms dissolved in alloy matrices can also have a pinning effect on mobile dislocations [36,68-71]. A creep threshold stress may exist, which is defined as a lower limiting stress below which no measurable creep rate can be experimentally achieved [64]. The presence of a threshold stress plays an important role in controlling the apparent creep behavior [72-74]. The following section will discuss the origin of threshold stress and the methods in determining threshold stress.

2.4.3.1 Definition of threshold stress

The origin of threshold stress in a material is alternatively interpreted to be the inhibition of dislocation movement either by particles [36,69], by solute atoms [70,71], or by the multiple sources [48].

1. Interaction between particles and dislocations

In the dispersion strengthened aluminum alloys, the presence of the unsharable particles could greatly strengthen the creep resistance [68]. It has been suggested that the particles act as effective barriers to the movement of dislocations and give rise to threshold stress for creep [73]. Lin *et al.* reported that the dislocation particle interaction configuration as shown in Fig. 2.6, suggesting the presence of threshold stress [66].

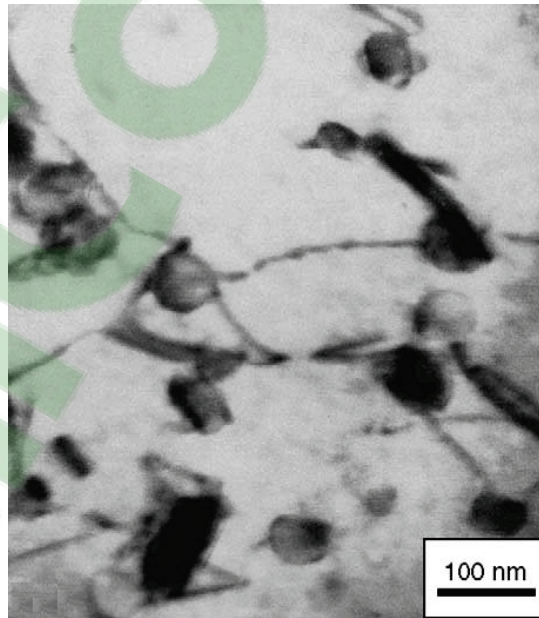


Fig. 2.6 Configuration representing particle dislocation interactions in 2014 Al, revealing the presence of threshold stress [66].

Several models have been proposed to explain the nature of the interaction between dispersion particles and dislocations and to give the magnitude of threshold stress: (a) the threshold stress is the stress required to bow the dislocation between two particles [75,76], corresponding Orowan stress σ_{or} , (b) the additional back stress associated with the local climb of dislocations over an obstacle [77,78], referred as σ_b , and (c) the stress associated with detaching a dislocation from an obstacle which exerts an attractive interaction [72,79], termed as σ_d . The equations for the three possible models together with various parameters are given in Table 2.6.

Table 2.6 Threshold stress models proposed for the dispersoids strengthened alloys.

Model	Stress	References
Orowan stress	$\sigma_{or} = 0.84M \frac{Gb}{(\lambda-d)}$	[75,76]
Local climb (back stress)	$\sigma_b = 0.3M \left(\frac{Gb}{\lambda}\right)$	[77,78]
Detachment stress	$\sigma_d = \sigma_{or} \sqrt{1 - K^2}$	[72,79]

M is the appropriate Taylor factor, λ is the inter-particle spacing, and d is average particle diameter;

K is a relaxation parameter that takes value between 0 (maximum attractive interaction) and 1 (no attractive interaction).

Usually, the magnitude of the threshold stress is related with the particle radius [48]. When the average radius is small, the experimental measured threshold stress is smaller than the calculated Orowan stress [42,48,80]. Marquis *et al.* [80] showed that the threshold stress

increased from 9% to 70% of the Orowan stress for dislocation looping with increasing average particle radius from 2 to 25 nm in Al–Sc alloys. The normalized threshold stress, defined as the ratio of the measured threshold stress to a calculated Orowan stress, is plotted as a function of average precipitate radius as shown in Fig. 2.7, has been reported by many researches [42,81,82].

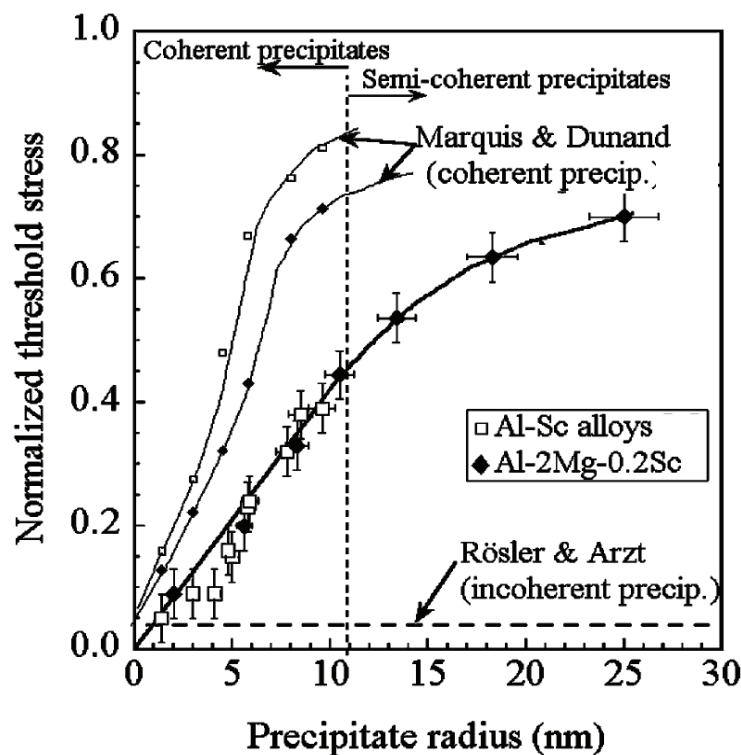


Fig. 2.7 Creep threshold stress, normalized with respect to a calculated Orowan stress at 300 °C, as a function of average precipitate radius.

When the average radius is large, the experimental measured threshold stress is larger than the calculated value which is probably due to the load transfer and substructural strengthening effect, similar as the effect in aluminum composites [67,73,83]. Load transfer

refers to the situation in which a part of the external load is carried by the reinforcement, and there is a consequent reduction in the effective stress acting on the material. Substructural strengthening referred to the additional strengthening which may arise from the increase in dislocation density due to the thermal mismatch between the matrix and the reinforcement or the presence of internal stresses because of the resistance by the reinforcement to plastic flow in the matrix [84]. A coefficient, β , can be used to describe both load transfer and all substructural strengthening process, and the effective stress, σ_e , acting on the matrix can be represented by the expression [85]

$$\sigma_e = (1-\beta) \sigma - \sigma_{th} \dots\dots\dots (\text{Eq. 2.15})$$

where σ is the applied stress, and β has a value in the range from 0 when load transfer and substructural strengthening is absent to a maximum value of 1 when all of the load is transferred and the maximum substructural strengthening effect. In order to use Eq. 2.14 in the standard relationship for the steady-state creep rate, it is convenient to express the effective stress in the form

$$\sigma_e = (1-\beta) (\sigma - \sigma_{th}^*) \dots\dots\dots (\text{Eq. 2.16})$$

where σ_{th}^* is defined as an apparent threshold stress which is given by

$$\sigma_{th}^* = \frac{\sigma_{th}}{(1-\beta)} \dots\dots\dots (\text{Eq. 2.17})$$

The incorporate of load transfer and substructural strengthening in the analysis and

equation 2.14 is replaced by

$$\dot{\epsilon}_m = A'(1-\beta)^{n_i} \left(\frac{\sigma - \sigma_{th}^*}{G} \right)^{n_i} \exp\left(-\frac{Q_a}{RT}\right) \dots\dots\dots (Eq. 2.18)$$

From Eq. 2.18, the value of thresholds stress estimated from the double logarithmic creep rate curves, which yields the apparent threshold stress σ_{th}^* , rather than the true threshold stress. If $\beta = 0$ and $\sigma_{th}^* = \sigma_{th}$, the load transfer or substructural strengthening is absent, which is occurred in most of the precipitate strengthening alloys [80]; however, in the large particle containing alloys or the composites, additional strengthening is often present, $\beta \neq 0$ and the values of σ_{th} is magnified by a factor of $1/(1-\beta)$.

2. Interaction between solute atoms and dislocations

When solute atoms with very low mobility interact with moving dislocations and prevent their motion, the breakaway of dislocations from the solute atmospheres is required in order to continue deformation. The interaction between the solute atoms and lattice or grain-boundary dislocations would be the origin of threshold stress [71,86]. Owing to the strong attractive force between them, an extra external stress is needed before the dislocation breaks away from their solute atmospheres; *i.e.*, the energy to overcome the barrier that is provided by an external force introduces a threshold stress. The interaction energy between a solute atom and an edge dislocation in the lattice, which turns in binding energy W_m , can be calculated by [87]

$$W_m = \frac{4(1+\nu)Gb\epsilon_m r_0^3}{3(1-\nu)y} \dots\dots\dots (\text{Eq. 2.19})$$

where ν is the Poisson ratio, r_0 is the atomic radius of the matrix, and ϵ_m is the atomic radius difference between the matrix and solute r_l , which is given in $(r_l - r_0)/r_0$; y is the distance of dislocation line given by $2b/3$ [88]. The actual binding energy would be smaller than the calculated values, because of the existence of a dislocation core and segregation of solute atoms [70,88]. Sato *et al.* [89] reported that the Cr in solid solution in Al–Cu alloys could cause the presence of threshold stress and the values of threshold stress largely increased with increasing Cr from 0.002 to 0.05 wt.%.

On the other hand, the threshold stress arisen from the solute atmosphere would be decreased with increasing temperature [66,71]. Mohamed *et al.* [90] have speculated that the strong temperature dependence of the threshold stress may be a reflection of an interaction between impurities that are able to segregate at incoherent particles and dislocations that are captured at the detachment side of the particles. The segregation of solute atoms can be described by a relation in the form [70]:

$$c = c_0 \exp\left(\frac{U}{RT}\right) \dots\dots\dots (\text{Eq. 2.20})$$

where c is the concentration of solute segregation, c_0 is the average concentration of solute atoms and U is the binding energy between the solute atoms and a boundary dislocation. With increasing temperature, the segregation of solute atoms is greatly decreased, which in turn decrease the threshold stress.

3. Relation between multiple sources of threshold stress

In the cases of two or more origins to the threshold stress, it is necessary to understand the relation among the individual origins. Two models have been reported for the relation among the contribution of the threshold stresses [48,91,92]. One is the case that the individual origins, which give rise to the threshold stress, are competing and independent, as shown in Figs. 2.8(a) and (b) for example. In this case, it is considered that dislocation motion is impeded simultaneously by all the origins, which leads to a threshold stress higher than for individual source. The experimentally determined threshold stress is expressed by the sum of the threshold stress caused by individual origins:

$$\sigma_{th} = \sum_{i=1} \sigma_{thi} \dots\dots\dots \text{(Eq. 2.21)}$$

where $i = \alpha, \beta, \dots$ is in a generalized form. Karnesky *et al.* [48] have investigated the creep behavior of pure aluminum containing Al_2O_3 incoherent dispersoids and Al_3Sc precipitates at a temperature of 300 °C. It is found that the threshold stress is higher than that for a dislocation interaction with either Al_2O_3 incoherent dispersoids or Al_3Sc precipitates, and this kind of creep behavior is explain by the “compete model” where the threshold stress is equal to the sum of the threshold stress from individual contribution.

The other model is that the individual origins, which give rise to the threshold stress, are sequential, rather than simultaneously as shown in Figs. 2.8(c) and (d). In this case for example, the highest threshold stress in the sequential process corresponds to the

experimentally determined threshold stress:

$$\sigma_{th} = \max(\sigma_{thi}) \dots\dots\dots (Eq. 2.22)$$

where $i = \alpha, \beta, \dots$ is in a generalized form. Rosler and Baker [92] have studied the threshold stress in the alloys where contained two populations particles (nanometer and micrometer size) and predicted that the contribution of the micrometer particles impeded dislocations movement and contributed to the threshold stress rather than nanometer-size precipitates.

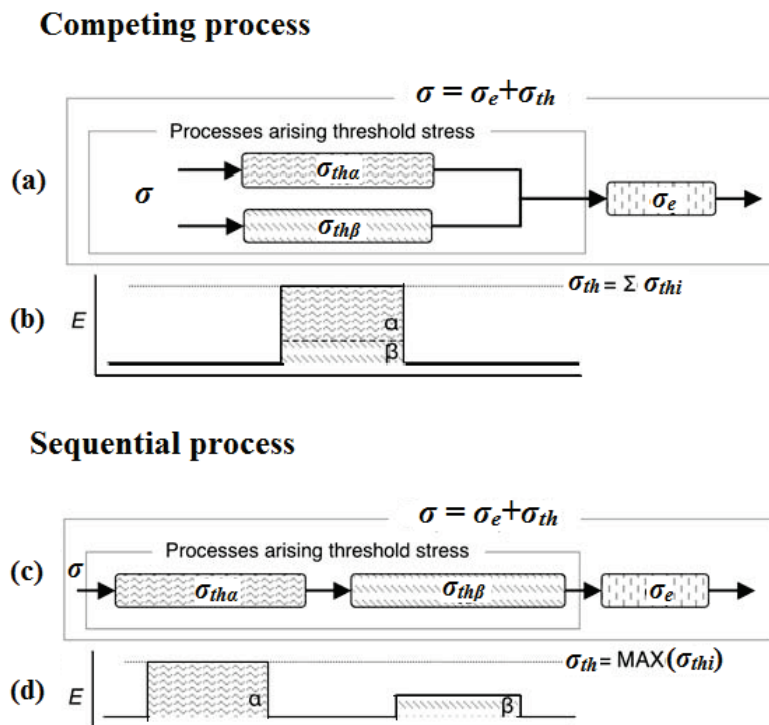


Fig. 2.8 Threshold stress originated from two processes, (a) threshold stress in the competing process, (b) corresponding energy profile, (c) threshold stress in the sequential process, (d) energy profile.

2.4.3.2 Determination of threshold stress

In the dispersion strengthened aluminum alloys, it is possible to estimate the magnitude of σ_{th} by plotting the data on linear axes as $\dot{\epsilon}_m^{1/n}$ against the σ and extrapolating linearly to zero creep rate [93] or by using a linear extrapolation method to a minimum creep rate of 10^{-10} s^{-1} [64].

The former procedure has the disadvantage that it requires, a priori, a judicious selection of the appropriate value of n_t and the procedure is useful only when the experimental creep data extend over five orders of magnitude [57,93]. In addition, by choosing limited discrete values of n , such as 3 or 5, the possibility of a non-integer value of n_t is necessarily excluded. Second, the linear extrapolation of plotting $\dot{\epsilon}_m^{1/n}$ against σ requires an initial selection of the value of n_t and then uses this value to determine the corresponding magnitudes of σ_{th} . However, it is apparent that a more appropriate procedure should be based on determining the values of σ_{th} , using a method which is independent of n_t , and then taking these values of σ_{th} to calculate n_t , from a line of best fit in a logarithmic plot of $\dot{\epsilon}_m$ versus $(\sigma - \sigma_{th})$.

On the other hand, Li *et al.* [64] proposed a new method for estimating the threshold stress, where the double logarithmic plot of creep rate versus applied stress to a creep rate of 10^{-10} s^{-1} . The stress at this creep rate is used to define as σ_{th} . The creep rate of 10^{-10} s^{-1} represents essentially the slowest rate which may be conveniently measured in laboratory experiments. However, it should be noted that this procedure is valid only when the

extrapolation takes place over a limited range of creep rates of the order of not more than approximately two orders of magnitude.

2.4.4 Creep stress exponent

The creep deformation of aluminum is a very complicated process, which can be sorted by their true stress exponent values (n_t) from smallest to largest. Many models have been established during the different stage of the creep [53,94-100]. It is generally believed that there are four types of creep mechanisms in aluminum alloys associated with the different n_t values: when $n_t \leq 2$, the grain boundary sliding and diffusion creep played a dominant role [94-96], $n_t = 3$, for creep controlled by viscous glide processes of dislocations [97,98], $n_t = 5$, for creep controlled by high-temperature dislocation climb [99], and $n_t = 8$ for lattice diffusion-controlled creep with a constant structure [53].

2.4.4.1 $n_t \leq 2$ regions: Diffusion creep and GBS

At low true stress exponent ($n_t < 2$), creep is mainly dominated by the diffusion of vacancies. When a stress is applied to a material, there is an excess of vacancies along those grain boundaries which is lying perpendicular to the tensile axis and a corresponding depletion of vacancies along those grain boundaries which is experiencing a compressive stress. The stress-directed flow of vacancies that take place in order to restore equilibrium referred to diffusion creep. This vacancy flow may involve either Nabarro-Herring (N-H) creep [94,95] occurred as vacancies moving through a crystal (as indicated in Fig. 2.9(a)) or

Coble creep [96] in which diffusion flow occurred along the grain boundaries (as indicated in Fig. 2.9(b)).

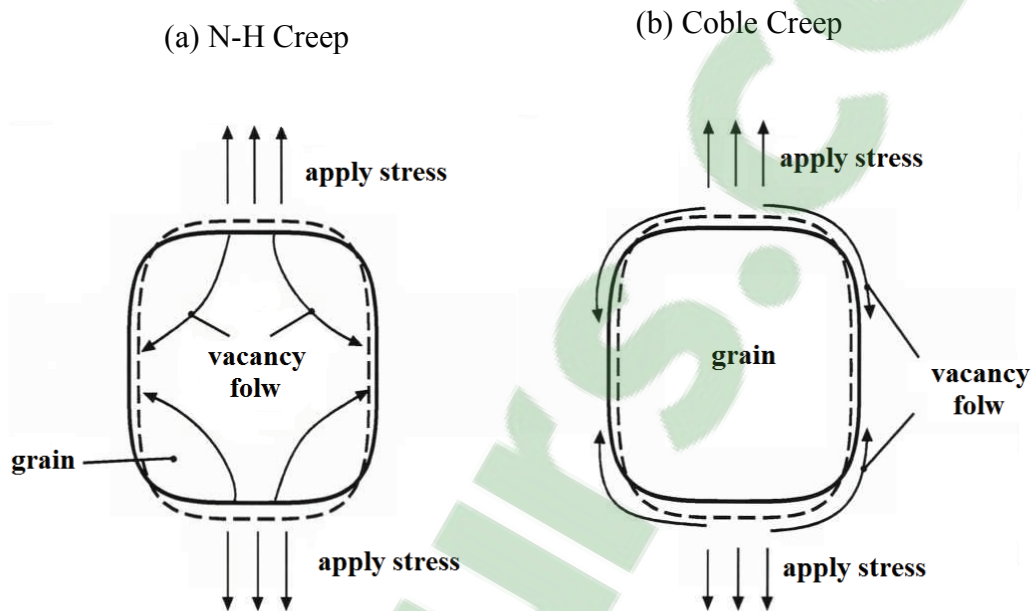


Fig. 2.9 Schematic view of vacancy diffusion during N-H and Coble creep. Arrows indicate the flow of vacancies through the grains from boundaries lying normal to the tensile direction to parallel boundaries. Thicker arrows indicate the tensile axis.

Grain boundary sliding (GBS, $n_t = 2$) is a creep mechanism with no significant elongation but they become displaced with respect to each other so that there is a net increase in their number lying along the tensile axis [100,101]. It has been shown that GBS occurred in crystalline solids when the grain size is very small (typically, $\leq 10 \mu\text{m}$) or when the large grain size is reasonably large ($> 1 \text{ mm}$) at temperature greater than about $0.5 T_m$, where T_m is the absolute melting point [53]. GBS is aided by an accommodation mechanism

of dislocation migration as shown in Fig. 2.10, which is controlled by either lattice diffusion or grain boundary diffusion.

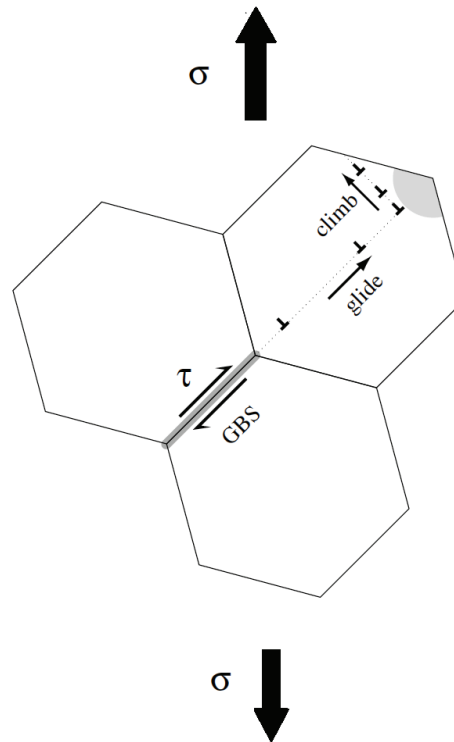


Fig. 2.10 Grain-boundary sliding creep mechanism.

The microstructure evolution during GBS could be observed by metallographic in aluminum as shown in Fig. 2.11 [42,102]. During the creep process, the slip bands become coarser and wider spaced, which can be detected in the optical microscope as indicated in Fig. 2.11(a). On the other hand, as shown in Fig. 2.11(b), the close parallel lines are markers introduced during the preparation of the sample, which are offset by coarse slip bands. The displacement of the line is due to grain boundary sliding.

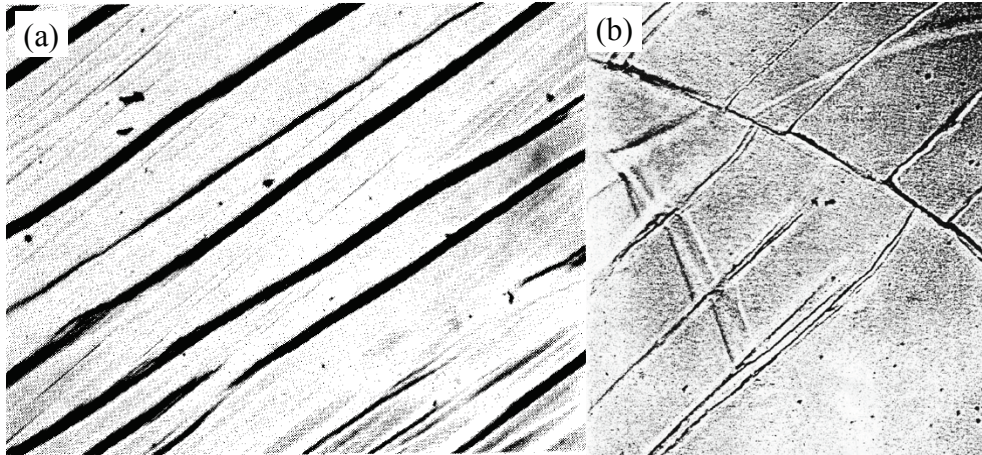


Fig. 2.11 The slip bands and GBS of aluminum during creep deformation. (a) slip in an aluminum crystal deformed at a slow creep rate at 573 K. $\times 30$; (b) GBS of aluminum, the close parallel lines are markers introduced during the preparation of the sample [102].

2.4.4.2 $n_t = 3$ and $n_t = 5$ regions: Dislocation glide and Dislocation climb

For dispersion strengthened aluminum alloys, over a wide range of stress exponent ($3 \leq n_t \leq 5$), the typical steady-state (or minimum creep stage) behavior of aluminum is diffusion controlled dislocation creep. The creep mechanism is believed to consist of viscous glide of dislocations of solid class A behavior (solute-drag creep) [98,103] and diffusion assisted dislocation-climb of class M creep behavior [99]. Since glide and climb are sequential processes, the creep rate is determined by the slower one. The main variation of the above deformation mechanisms in aluminum alloys will be discussed in the following session.

In class-A alloys, where the true stress exponent of $n_t = 3$, and the creep rate is controlled by dynamic interaction between solute atoms and edge dislocations. An elastic

stress field exists around each edge dislocation, with a compressive stress field above dislocation and a tensile stress field below dislocation [104]. To decrease the total strain energy, large solute atoms tend to migrate to the tensile stress fields of dislocations, and small solute atoms tend to migrate to the compressive stress fields. The non-symmetry of solute atom distributions around a slowly moving dislocation causes a drag force on the dislocation and slows its motion, as shown in Fig. 2.12. The drag force from solute atmospheres controlled the glide velocity of dislocations and the creep rate.

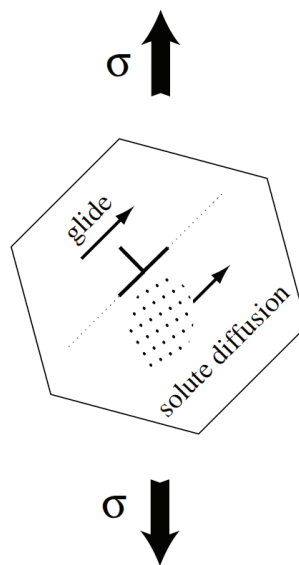


Fig. 2.12 Schematic view of class-A creep mechanism.

Calculations reported in the literature [86] showed that the major force retarding the glide of dislocation in solid solution strengthening aluminum alloys arisen from the Cottrell-Jaswon interaction [104], where the stress σ_s , caused from solute atom atmospheres is given by [90]

$$\frac{\sigma_s}{G} = 0.05ce^2\left(\frac{Gb^3}{kT}\right) \dots\dots\dots(\text{Eq. 2.23})$$

where k is Boltzmann's constant, e is the atom misfit parameter, c is the solute concentration, G is the shear modulus, b is the Burgers vector.

The major microstructural characteristics of dislocation glide creep is a fairly uniform distribution of dislocations and little or no evidence for subgrain formation. Horiuchi and Otsuka [105] have showed that the distribution of dislocations during steady-state creep in an Al-2.7 wt.% Mg alloy at temperature range of 328–461 °C was quite uniform both within and near grain boundaries, without forming cell structures, as shown in Fig. 2.13 for example. Meng *et al.* [106] studied the microstructure in the steady-state creep of Al-Mg alloys, and pointed out the presence of subgrains in the dislocation glide region, where the stress exponent is about 3. In their analysis, they found that these subgrains were not the result of creep deformation because they were also found in the unstrained section of the specimens.

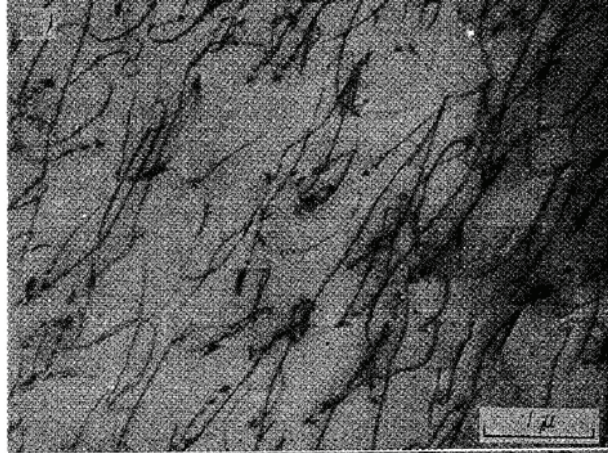


Fig. 2.13 Dislocation structures for steady-state creep of Al–Mg alloys at 359 °C [105].

Class-M alloys exhibit creep characteristics much like pure metals where the climb of edge dislocations is the rate-controlling process [103]. The major characteristics of this creep include the stress exponent of 5 and the formation of subgrains. When a moving dislocation is inhibited by an obstacle on its slip plane and the stress is lower than that needed for dislocation glide over the obstacles; then the dislocation would climb over the obstacles by diffusion processes to parallel slip plane, as shown in Fig. 2.14. Thus, the movement of dislocation by climbing is slower than that by gliding, and it controls the overall rate of the creep deformation.

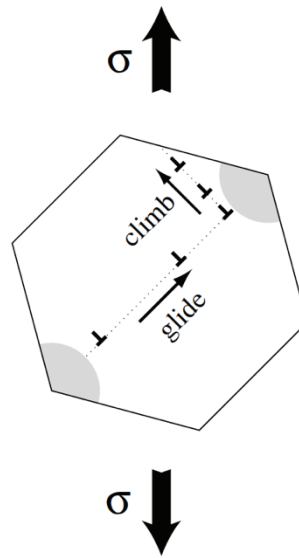


Fig. 2.14 Mechanism of dislocation-climb creep.

The formation of subgrains dominated the microstructure changes that occurred during the dislocation-climb controlled creep in most polycrystalline metals at temperature above about $0.5 T_m$. The cells were formed due to accumulation of edge dislocations by climb (polygonization) and leading to the development of subgrains, as shown in Fig. 2.15 for example [42]. Besides, Morris and Martin [107] studied the microstructure evolution during the dislocation-climb controlled creep process in an Al-11 wt.% Zn alloys, and found the subgrains, highly bowed dislocations in the subgrain interior, and the dislocations emitted from boundaries.

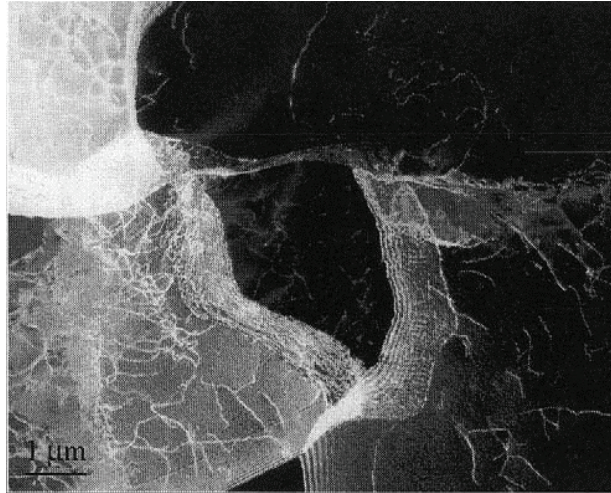


Fig. 2.15 TEM micrographs of post-creep dislocation structures of Al–0.3 wt.% Sc alloy aged at 300 °C for 5 h and crept at 300 °C under 36 MPa [42].

Many investigations have indicated that the subgrain size was a unique function of the flow stress [69,108]. The average subgrain size, ω , has been measured experimentally and reported as being related to the stress, σ , through a relationship of form [69]:

$$\omega = \lambda b \left(\frac{G}{\sigma} \right)^r \dots\dots\dots (\text{Eq. 2.24})$$

where b is the magnitude of the Burgers vector, λ is a constant, G is the shear modulus and r is a constant. Moreover, analysis of subgrain data of pure aluminum or pure aluminum matrix show that $r=1$ and $\lambda=10$ [108]. Under the condition that creep deformation is driven by an effective stress, σ_e ($\sigma_e = \sigma - \sigma_{th}$), the above equation may be modified as follows:

$$\omega = 10b \frac{G}{\sigma_e} \dots\dots\dots (\text{Eq. 2.25})$$

Generally, in the dispersoids strengthened aluminum alloys, the subgrain size is affected by the particle size and the average interparticle spacing [108,109]. When the

average interparticle spacing is much smaller than the experimental determined subgrain size, the substructure is dependent on the particle interparticle spacing [5]. However, in some cases, when the average interparticle spacing is much larger than the experimental determined subgrain size or the particle is very fine, the substructure is stress dependence. Pandey *et al.* [109] have investigated the creep behavior of the Al–10 vol.% SiC composite with particle sizes of 14.5 and 45.9 μm and found the subgrain size of crept specimens followed the stress-controlled substructure model. Seidman *et al.* [42] investigated the microstructure evolution of Al–0.3 wt.% Sc alloys containing small precipitates of radius 1.4 nm during creep test at 300 °C under load of 22 MPa and observed the formation of subgrains which is similar to that observed in pure aluminum.

For the dislocation glide and dislocation climb creep mechanisms, the creep resistance could be improved by many factors, including substructure refinement, solute alloying elements and particle strengthening. The subgrains, solute atoms, and particles could act as barriers to slip and resist dislocation motion, which would enhance the resistance to creep deformation [32,110-112]. Mishra *et al.* [111] studied on the AA2009–15 vol.% SiC_w aluminum composites have shown that the pre-stressing of samples led to enhancement in the creep strength due to the boundaries of smaller subgrains formation during exposure to higher stress. Ferreira. I *et al.* [112] studied the effect of subgrains size on creep rate of pure aluminum and got the conclusion that one order of magnitude decrease in subgrain size will produce a decrease of two orders of magnitude in creep rate.

Solute additions can lead to decreasing grain boundaries mobility, reducing the dislocation glide rate and accelerating dislocation multiplication [17,110,113,114]. In the research of Babicheva *et al.* [113], they showed that segregations of Fe, Co, Ti and Mg in grain boundaries (GBs) of nanocrystalline aluminum could strengthen their GBs and have a positive effect on the mechanical properties and thermo-stability. Sherby *et al.* [114] showed that during the creep process of Al–Fe alloys at 200–250 °C temperature range, where the Al–0.04 wt.% Fe alloy exhibited a higher creep strength than the Al–0.45 wt.% Fe alloy containing FeAl₃ dispersoids.

On the other hand, the presence of particles promotes the retardation of dislocation glide and climb [9,48] and stabilizing the substructure [80]. McQueen [6] investigated the Fe-particle stabilized effect on the aluminum conductors and showed that addition of Fe can greatly improve the creep resistance for Al–0.5 wt.% Fe–0.5 wt.% Co and Al–0.65 wt.% Fe alloys due to the presence of Fe-containing particles.

In practice, the dislocation glide and climb process is often more complex in aluminum alloys because that a transition between dislocation-glide and dislocation-climb creep occurred with increase of stress under a favourable condition [115]. The level of the transition stress depends on the test temperature, the concentration of the solute, the size different between the solute and the matrix atom and the stacking fault energy of the material. Such transitions are illustrated schematically in Fig. 2.16 [116]. Many researchers have shown that these transitions can occur when there is an increase or decrease in creep

stress in Al–Mg alloys as and Al–Cu alloys [117,118].

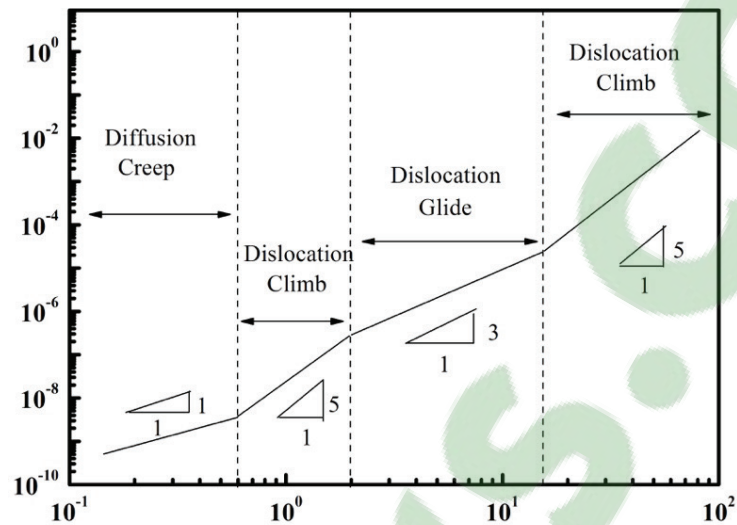


Fig. 2.16 Schematic illustration of strain rate versus stress for Al–Mg alloy, showing the transition in creep mechanisms [116].

Chaudhury *et al.* [117] have investigated the creep behavior of Al–2 wt.% Cu alloys in the temperature range of 510–570 °C, and found two transitions in the stress dependence of steady state creep rate at constant temperature. The first transition occurred at intermediate stresses and was characterized by a change in dislocation-climb creep to dislocation-glide creep with stress exponent changes from 4.5 to 3.2; while the second transition was observed at higher stresses and was manifested by a change in dislocation-glide creep to dislocation-climb creep with stress exponent changes from 3.2 to 4.5, respectively.

In the research of Yavari *et al.* [118], the creep behavior of Al–5 wt.% Mg was studied at the testing temperature of 554 °C. They pointed out that the transient from dislocation climb to dislocation glide occurred with increase of applying stress. At stress lower than 0.5

MPa, the stress exponent was 4.4 and substructural observation showed the formation of subgrain boundaries; while at stress larger than 0.5 MPa, the stress exponent was 3.1 and substructural observation revealed an essentially random distribution of dislocation. Later, Yavari and Longdon [119] studied the creep behavior of Al–3 wt.% Mg and Al–5 wt.% Mg alloys at a temperature of 350 °C, and observed the transition from dislocation glide to dislocation climb with increasing stress. They showed an essentially random distribution of dislocations in the region with stress exponent close to 3.0; while with increasing of the stress, it was found that transition to stress exponent close to 4.6 occurred and the formation of subgrain was observed.

2.4.4.3 $n_t=8$ regions: Substructure-invariant creep

The substructure-invariant creep model was developed originally by Sherby *et al.* [32] to explain the creep behavior of alloys under constant substructure, the subgrain diameter does not vary with stress due to the strong retaining effect of the particles. This mechanism mostly occurred at high temperatures. The major characteristics of this creep incorporate two specific aspects: (I) the stress exponent is equal to 8, and (II) the activation energy for creep is equal to the value anticipated for self-diffusion in the lattice of the matrix. Many researchers [120,121] have demonstrated the possibility of the substructure-invariant model of creep in aluminum composites where the substructure is independent of the level of the applied stress and the value of n close to 8. Pandey *et al.* [120] examined the creep of an Al–4 wt.% Mg reinforced with 10 vol.% SiC, and found the stress exponent was close to 8,

besides, the activation energy was close to the lattice self-diffusion of aluminum.

2.4.5 Analyzing the creep mechanisms

Analysis of the variation of stress exponent value n is regularly considered as a common procedure for estimating the possible creep mechanisms. Determine the n value and compare this value to known stress exponent for different mechanisms in unreinforced aluminum alloys. However, in the dispersion strengthened aluminum alloys, a threshold stress is existed, which is related to the interaction between moving dislocation and dispersions particles. In this case, it has been assumed [73,74] that the presence of a threshold stress controls the apparent creep behavior. The introduction of a threshold stress into the analysis is usually effective in giving the values of n_i that is similar to that obtained in the unreinforced matrix materials.

Another useful tool which sheds light in identifying creep mechanism is the use of the creep deformation maps which were proposed by Weertman [45] in 1965 and improved by Ashby [122] later. Deformation maps have been developed by solving constitutive equations for different deformation mechanisms, and then plotted the different regions in stress-temperature space. Fig. 2.17 shows a creep deformation map in stress-temperature space [122]. These maps are not absolute, but can be helpful in determining potential creep deformation regimes.

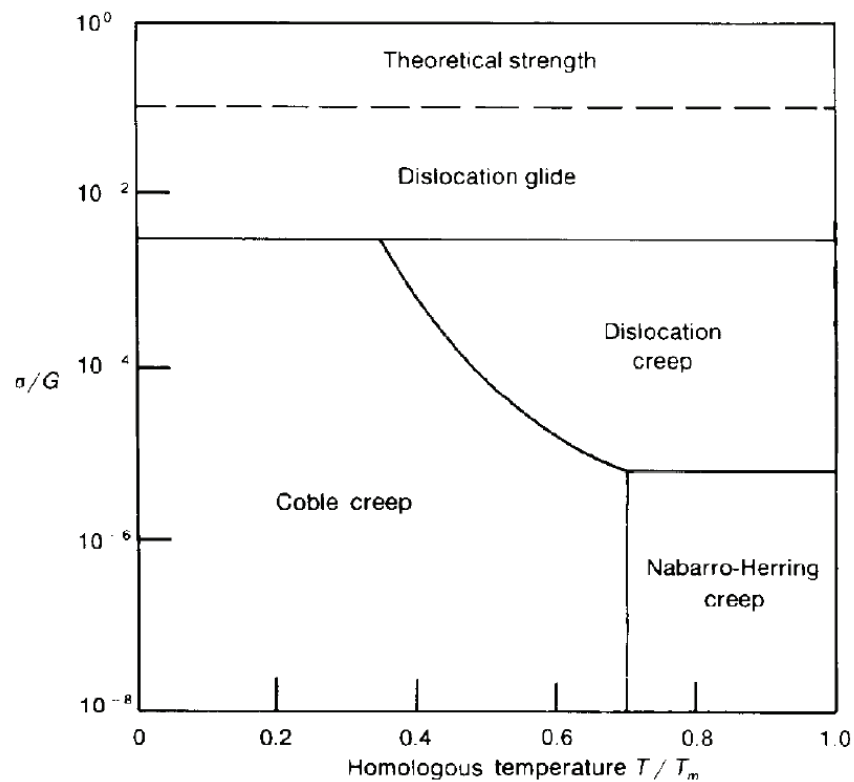


Fig. 2.17 Creep deformation mechanism map Ashby-map [122].

2.4.6 Investigation of creep properties in aluminum conductors

Like all metals under sustained stress, there is a gradual deformation over a term of years in aluminum conductors [21]. Hard-drawn AA1350-H19 aluminum wire in stranded cables under a steadily applied load of 96.5 MPa at 20 °C (70% yield strength) will creep approximately 0.4 to 0.6% of initial length in 10 years. However, its creep strength decreases rapidly with time at temperatures above 100 °C [19]. These limitations do not generally provide a constraint for distribution applications. Alloys include 0.5 wt.% Fe with 0.5 wt.% Co and 0.5 wt.% Fe with 0.2–0.4 wt.% Si wires under repeated testing have

shown better creep characteristics and reduced loss of mechanical strength than either EC alloys at high temperatures. Barker *et al.* [19] studied breaking load tests on Al–0.5 wt.% Fe–0.3 wt.% Si alloys creep tested at 100 °C for 200 hours, and showed a loss of strength of 4% compared with 5% for the equivalent AA1350 aluminum conductor.

On the other hand, Jaffe and Dorn [98,123] studied the creep behavior of polycrystalline aluminum over the range of 0–77 °C and found that the activation energy was 115 KJ/mole with a stress exponent of 3. Metallographic studies and comparison with theory suggested that creep in this range is controlled by the rate of cross-slip dislocations. Sherby *et al.* [114] postulated that dislocation climb was responsible for creep in pure aluminum at 200–400 °C with a stress exponent of 4.4.

References

- [1] J. Rabinow, Nat. Bur. Stand. (US) NBSIR (1978) 78-1507.
- [2] D. Newbury, S. Greenwald, J. Res. Nat. Bur. Stand. 85 (1980) 429-440.
- [3] A. Fox, G.J. Herbert, IEEE Trans. Parts, Hybrids, Packag. 9 (1973) 22-30.
- [4] C. Olin, in: U.S.P. 3711339 (Ed.), US, 1973.
- [5] E.H. Chia, E.A. Starke, Metall. Trans. A 8 (1977) 825-832.
- [6] H.J. Mcqueen, K. Conrod, G. Avramovic-cingara, Can. Metall. Quart. 32 (1993) 375-386.
- [7] Guo Lei, Yi Dan-qing, Zang Bing, Wang Bin, Liu hui-qun, L. gong-qi, Trans. Nonferrous Met. Soc. China 23 (2013) 2083-2089.
- [8] O. Engler, G. Lapyteva, N. Wang, Mater. Char. 79 (2013) 60-75.
- [9] X.Y. Zhang, H. Zhang, X.X. Kong, D.F. Fu, Trans. Nonferrous Met. Soc. China 25 (2015) 1763-1769.
- [10] D.V. Malakhov, D. Panahi, M. Gallerneault, Calphad 34 (2010) 159-166.
- [11] C.M. Allen, K.A.Q. O'Reilly, B. Cantor, P.V. Evans, Prog. Mater. Sci. 43 (1998) 89-170.
- [12] M. Shakiba, N. Parson, X.G. Chen, Mater. Sci. Eng. A 619 (2014) 180-189.
- [13] R.W. Westerlund, Metall. Trans. 5 (1974) 667-672.
- [14] M. Shakiba, N. Parson, X.G. Chen, J. Mater.Eng. Perform. 24 (2015) 404-415.
- [15] H. Okamoto, Handbook: Phase diagrams for binary alloys, 2nd ed., 2010.
- [16] M. Shakiba, N. Parson, X.G. Chen, Mater. Sci. Eng. A 636 (2015) 572-581.

-
- [17] X. Sauvage, N. Enikeev, R. Valiev, Y. Nasedkina, M. Murashkin, *Acta Mater.* 72 (2014) 125-136.
- [18] T. Shikagawa, *Hitach cable review* 25 (2006) 18-21.
- [19] K.W. Barber, K.J. Callaghan, *IEEE T. Power Deliver.* 10 (1995) 403-409.
- [20] ASTM. B800-05, Standard Specification for 8000 Series Aluminum Alloy Wire for Electrical Purposes-Annealed and Intermediate, ASTM International, West Conshohocken, PA, 2005.
- [21] N.S. Beniwal, H.O. Gupta, D.K. Dwivedi, XXXII National Systems Conference (2008) 623-627.
- [22] J. Kindersberger, H. Löbl, S. Schoft, *Proceedings of the 20th International Conference on Electric Contact Phenomena, 2000*, pp. 367-372.
- [23] I.N. Fridlyander, *Physical Metallurgy of Aluminum and Its Alloys*, Moscow, 1983.
- [24] T. Shikagawa, G. Itoh, S. Suzuki, H. Kuroda, T. Horikoshi, *Aluminium Alloys* 519-521 (2006) 515-518.
- [25] M. Mujahid, N.N. Engel, E.H. Chia, *Scripta Metall.* 13 (1979) 887-893.
- [26] L. Weber, C. Fischer, A. Mortensen, *Acta Mater.* 51 (2003) 495-505.
- [27] M.F. Ashby, H. Shercliff, D. Cebon, *Materials: engineering, science, processing and design*, 1st ed., Butterworth-Heinemann, Amsterdam; Boston, 2007.
- [28] J.E. Hatch, Aluminum Association., American Society for Metals., *Aluminum: properties and physical metallurgy*, American Society for Metals, Metals Park, Ohio, 1984.
- [29] B. Raeisinia, W.J. Poole, D.J. Lloyd, *Mater. Sci. Eng. A* 420 (2006) 245-249.
- [30] Q.L. Zhao, B. Holmedal, Y.J. Li, *Philos. Mag.* 93 (2013) 2995-3011.

-
- [31] K. Liu, X.G. Chen, *Mater. Des.* 84 (2015) 340-350.
- [32] O.D. Sherby, R.H. Klundt, A.K. Miller, *Metall. Trans. A* 8 (1977) 843-850.
- [33] R. Iricibar, C. Pampillo, E.H. Chia, *Aluminum Transformation Technology and its Applications*, Metals Park Ohio, 1978.
- [34] C.J. Shi, W.M. Mao, X.G. Chen, *Mater. Sci. Eng. A* 571 (2013) 83-91.
- [35] O. Ryen, O. Nijs, E. Sjolander, B. Holmedal, H.E. Ekstrom, E. Nes, *Metall. Mater. Trans. A* 37A (2006) 1999-2006.
- [36] H.J. McQueen, E.H. Chia, E.A. Starke, *JOM* 38 (1986) 19-24.
- [37] H.J. Rack, M. Cohen, *Frontiers in Materials Science*, Dekker, New York, 1976.
- [38] R.J. McElroy, Z.C. Szkopiak, *Int. Mater. Rev.* 17 (1972) 175-202.
- [39] T. Furu, R. Orsund, E. Nes, *Mat. Sci. Eng. A* 214 (1996) 122-132.
- [40] C.J. Shi, X.G. Chen, *Mater. Sci. Eng. A* 613 (2014) 91-102.
- [41] D. Kalish, B.G. Lefevre, *Metall. Trans. A* 6 (1975) 1319-1324.
- [42] D.N. Seidman, E.A. Marquis, D.C. Dunand, *Acta Mater.* 50 (2002) 4021-4035.
- [43] C.J. Shi, X.G. Chen, *Mater. Sci. Eng. A* 596 (2014) 183-193.
- [44] G.E. Dieter, *Mechanical metallurgy*, 3rd ed., McGraw-Hill, New York, 1986.
- [45] R.W. Cahn, *Physical metallurgy*, North-Holland Pub. Co.; Wiley, Amsterdam, New York, 1965.
- [46] M. Spittel, T. Spittel, *Part 2: Non-ferrous Alloys-Light metal*, 4th ed., Springer Berlin Heidelberg, 2011.
- [47] A. Mamala, W. Sciezor, *Arch. Metall. Mater.* 59 (2014) 413-417.

-
- [48] R.A. Karnesky, L. Meng, D.C. Dunand, *Acta Mater.* 55 (2007) 1299-1308.
- [49] M. Jabłoński, T. Knych, B. Smyrak, *Arch. Metall. Mater.* 54 (2009) 671-676.
- [50] T.D. Ma, Y. Su, Q. Wang, J.L. Li, *Adv. Eng. Mater.* 750-752 (2013) 711-714.
- [51] F. Garofalo, *Fundamentals of creep and creep-rupture in metals*, Macmillan, New York, 1965.
- [52] O.D. Sherby, P.M. Burke, *Prog. Mater. Sci.* 13 (1967) 323-368.
- [53] T.G. Langdon, *Mater. Sci. Eng. A* 283 (2000) 266-273.
- [54] R.W. Honeycome, in: E.A.P. Ltd (Ed.), London, 1984, pp. 356-401.
- [55] P.E. Krajewski, J.W. Jones, J.E. Allison, *Metall. Mater. Trans. A* 26 (1995) 3107-3118.
- [56] L. Kloc, E. Cerri, S. Spigarelli, E. Evangelista, T.G. Langdon, *Mater. Sci. Eng. A* 216 (1996) 161-168.
- [57] R.S. Mishra, A.B. Pandey, *Metall. Mater. Trans. A* 21 (1990) 2089-2090.
- [58] X.W. Wei, X.T. Zu, W.L. Zhou, *Mater. Sci. Tech.* 22 (2006) 730-733.
- [59] R.E. Reed-Hill, *Physical metallurgy principles*, 2d ed., Van Nostrand, New York, 1972.
- [60] H. Wang, Q.D. Wang, C.J. Boehlert, D.D. Yin, J. Yuan, *Mater. Charact.* 99 (2015) 25-37.
- [61] O.D. Sherby, E.M. Taleff, *Mater. Sci. Eng. A* 322 (2002) 89-99.
- [62] F.R.N. Nabarro, *Mater. Sci. Eng. A* 309 (2001) 227-228.
- [63] R. W. Lund, W.D. Nix, *Metall. Trans. A* 6A (1975) 1329-1333.
- [64] Y. Li, T.G. Langdon, *Scripta Mater.* 36 (1997) 1457-1460.
- [65] S.P. Deshmukh, R.S. Mishra, K.L. Kendig, *Mater. Sci. Eng. A* 381 (2004) 381-385.

-
- [66] Z.G. Lin, S.L. Chan, F.A. Mohamed, *Mater. Sci. Eng. A* 394 (2005) 103-111.
- [67] S.P. Deshmukh, R.S. Mishra, I.M. Robertson, *Mater. Sci. Eng. A* 527 (2010) 2390-2397.
- [68] R.S. Mishra, T.K. Nandy, G.W. Greenwood, *Philos. Mag. A* 69 (1994) 1097-1109.
- [69] Y. Li, S.R. Nutt, F.A. Mohamed, *Acta Mater.* 45 (1997) 2607-2620.
- [70] P.K. Chaudhury, K.T. Park, F.A. Mohamed, *Metall. Mater. Trans. A* 25 (1994) 2391-2401.
- [71] P.K. Chaudhury, F.A. Mohamed, *Acta Metall.* 36 (1988) 1099-1110.
- [72] E. Arzt, D.S. Wilkinson, *Acta Metall.* 34 (1986) 1893-1898.
- [73] F.A. Mohamed, *J. Mater. Sci.* 17 (1982) 1381-1388.
- [74] F.A. Mohamed, *Mater. Sci. Eng. A* 245 (1998) 242-256.
- [75] E. Orowan, *Dislocation in Metals*, AIME, New York, M. Cohen(Ed), 1957.
- [76] U.F. Kocks, *Philos. Mag.* 13 (1966) 541-566.
- [77] R.S.W. Shewfelt, L.M. Brown, *Philos. Mag.* 35 (1977) 945-962.
- [78] E. Arzt, M.F. Ashby, *Scripta Metall.* 16 (1982) 1285-1290.
- [79] E. Arzt, J. Rosler, *Acta Metall.* 36 (1988) 1053-1060.
- [80] E.A. Marquis, D.N. Seidman, D.C. Dunand, *Acta Mater.* 51 (2003) 4751-4760.
- [81] Y. Harada, D.C. Dunand, *Mater. Sci. Eng. A* 329 (2002) 686-695.
- [82] J. Rosler, E. Arzt, *Acta Metall.* 36 (1988) 1043-1051.
- [83] Y. Huang, T.G. Langdon, *JOM* 55 (2003) 15-20.
- [84] Y. Li, T.G. Langdon, *Acta Mater.* 47 (1999) 3395-3403.

-
- [85] B.Q. Han, T.G. Langdon, *Mater. Sci. Eng. A* 322 (2002) 73-78.
- [86] F.A. Mohamed, *Mater. Sci. Eng.* 61 (1983) 149-165.
- [87] J. Friedel, *Dislocations*, 1st English ed., Pergamon Press; U.S.A. ed. distributed by Addison-Wesley Pub. Co., Reading, Oxford, New York., 1964.
- [88] D. Hull, D.J. Bacon, *Introduction to dislocations*, 4th ed., Butterworth-Heinemann, Oxford; Boston, 2001.
- [89] E. Sato, M. Valsan, K. Kuribayashi, P. Rodriguez, *Mater. Trans. JIM* 40 (1999) 754-759.
- [90] F.A. Mohamed, *Mater. Sci. Eng.* 38 (1979) 73-80.
- [91] W.J. Kim, D.W. Kum, *Mater. Tran. JIM* 40 (1999) 760-764.
- [92] J. Rosler, M. Baker, *Acta Mater.* 48 (2000) 3553-3567.
- [93] B.B. R. Lagneborg, *Met. Sci.* 10 (1976) 20-28.
- [94] F.R.N. Nabarro, *Philos. Mag.* 16 (1967) 231-237.
- [95] C. Herring, *J. Appl. Phys.* 21 (1950) 437-445.
- [96] R.L. Coble, *J. Appl. Phys.* 34 (1963) 1679-1682.
- [97] J. Weertman, *J. Appl. Phys.* 28 (1957) 1185-1189.
- [98] J.E. Dorn, N. Jaffe, *Trans. Met. Soc. AIME* 221 (1961) 229-233.
- [99] J. Weertman, *J. Appl. Phys.* 28 (1957) 362-364.
- [100] T.G. Langdon, *J. Mater. Sci.* 41 (2006) 597-609.
- [101] J.H. Han, F.A. Mohamed, *Metall. Mater. Trans. A* 42A (2011) 3969-3978.
- [102] D. Mclean, *J. Ins. Met.* 81 (1953) 293-300.
- [103] K.L. Murty, G. Dentel, J. Britt, *Mater. Sci. Eng. A* 410 (2005) 28-31.

-
- [104] A.H. Cottrell, M.A. Jaswon, Proc. R. Soc. Lon. Ser-A 199 (1949) 104-114.
- [105] R. Horiuchi, M. Otsuka, Trans. Jap. Ins. Met. 13 (1972) 284-293.
- [106] M.X. Ying, D.O. Northwood, I.O. Smith, Mater. Charact. 19 (1986) 285-304.
- [107] M.A. Morris, J.L. Martin, Acta Metall. 32 (1984) 549-561.
- [108] R.S. Mishra, Scripta Metall. Mater. 26 (1992) 309-313.
- [109] A.B. Pandey, R.S. Mishra, Y.R. Mahajan, Acta Metall. Mater. 40 (1992) 2045-2052.
- [110] N.N. Du, Y. Qi, P.E. Krajewski, A.F. Bower, Metall. Mater. Trans. A 42A (2011) 651-659.
- [111] R.S. Mishra, R.H. Lu, R.B. Grishaber, A.K. Mukherjee, Scripta Mater. 38 (1998) 1819-1824.
- [112] I. Ferreira, R.G. Stang, Acta Metall. 31 (1983) 585-590.
- [113] R.I. Babicheva, S.V. Dmitriev, Y. Zhang, S.W. Kok, N. Srikanth, B. Liu, K. Zhou, Comp. Mater. Sci. 98 (2015) 410-416.
- [114] O.D. Sherby, A. Goldberg, O.A. Ruano, Philos. Mag. 84 (2004) 2417-2434.
- [115] F.A. Mohamed, T.G. Langdon, Acta Metall. 22 (1974) 779-788.
- [116] D.O. Northwood, L. Moerner, I.O. Smith, J. Mater. Sci. 20 (1985) 1683-1692.
- [117] P.K. Chaudhury, F.A. Mohamed, Mater. Sci. Eng. A 101 (1988) 13-23.
- [118] P. Yavari, F.A. Mohamed, T.G. Langdon, Acta Metall. 29 (1981) 1495-1507.
- [119] P. Yavari, T.G. Langdon, Acta Metall. 30 (1982) 2181-2196.
- [120] A.B. Pandey, R.S. Mishra, Y.R. Mahajan, Metall. Mater. Trans. A 27 (1996) 305-316.
- [121] A.H. Monazzah, A. Simchi, S.M.S. Reihani, Mater. Sci. Eng. A 527 (2010)

2567-2571.

[122] M.F.A. H.J. Frost, Deformation-mechanism maps: the plasticity and creep of metals and ceramics, Oxford: Pergamon Press, 1982.

[123] N. Jaffe, J.E. Dorn, Trans. Met. Soc. AIME 224 (1962) 1167-1173.

CHAPTER 3
EXPERIMENTAL

Chapter 3

Experimental

3.1 Experimental design

A series of 8xxx aluminum alloys with various levels of Fe, Cu and Mg were designed to study their effects on the properties of 8xxx aluminum conductor alloys. The level of Fe was from 0.3 wt.% to 0.7 wt.% while Cu varied from 0.18 wt.% to 0.29 wt.% and Mg varied from 0.025 wt.% to 0.1 wt.% (all the alloy compositions in this research are in wt.% unless otherwise indicated). Tables 3.1–3.3 show the chemical compositions of the designed alloys used in this project.

**Table 3.1 Chemical compositions of the experimental alloys
at 0.3% Fe used in this work.**

Alloy#	Elements (wt.%)							
	Fe	Cu	Mg	Si	Mn	Cr	Zn	Al
L00	0.30	0.01	0.001	0.025	0.002	0.001	0.012	Bal.
L20	0.30	0.18	0.001	0.023	0.003	0.001	0.002	Bal.
L30	0.30	0.29	0.000	0.033	0.001	0.001	0.012	Bal.
L23	0.30	0.18	0.025	0.031	0.002	0.001	0.012	Bal.
L25	0.30	0.19	0.052	0.038	0.003	0.001	0.002	Bal.
L210	0.30	0.18	0.100	0.049	0.002	0.001	0.012	Bal.

**Table 3.2 Chemical compositions of the experimental alloys
at 0.5% Fe used in this work.**

Alloy#	Elements (wt.%)							
	Fe	Cu	Mg	Si	Mn	Cr	Zn	Al
M00	0.46	0.01	0.001	0.046	0.002	0.001	0.012	Bal.
M20	0.50	0.18	0.001	0.027	0.004	0.001	0.002	Bal.
M30	0.47	0.29	0.000	0.023	0.002	0.001	0.003	Bal.
M23	0.46	0.18	0.026	0.051	0.002	0.001	0.013	Bal.
M25	0.44	0.17	0.055	0.021	0.001	0.001	0.002	Bal.
M210	0.47	0.18	0.100	0.049	0.002	0.001	0.012	Bal.

**Table 3.3 Chemical compositions of the experimental alloys
at 0.7% Fe used in this work.**

Alloy#	Elements (wt.%)							
	Fe	Cu	Mg	Si	Mn	Cr	Zn	Al
H00	0.70	0.01	0.001	0.023	0.002	0.001	0.013	Bal.
H20	0.70	0.19	0.001	0.042	0.003	0.001	0.016	Bal.
H30	0.71	0.29	0.000	0.032	0.003	0.001	0.002	Bal.
H23	0.69	0.18	0.027	0.052	0.002	0.001	0.013	Bal.
H25	0.70	0.18	0.056	0.042	0.003	0.001	0.012	Bal.
H210	0.72	0.18	0.100	0.051	0.002	0.001	0.013	Bal.

The alloys used for this study were provided by the Rio Tinto Aluminum (Arvida, Quebec, Canada). The samples were provided in the form of the as-cast billets and 9.5 mm extruded rods. The rods were produced and fabricated into 9.5 mm for drawn wire by convention extrusion method which consists of fabrication of DC cast billets and hot extrusion. The true strain from the cast materials to supply rods is 0.991. Besides, in addition to the convention extrusion method, alloys with 0.3% Fe and 0.7% Fe were fabricated into 9.5 mm rods using integrated continuous cast rolling operation (Propezi

process) with a true strain of 0.986 [1].

Besides, in order to investigate the influence of Fe solute atoms on the creep properties, the extruded rods were subjected to two kinds of thermal holding treatments as shown in Table 3.4. Two-step thermal holding treatment was used for LT treatment to firstly have the similar phase category and grain structure, and then low Fe solute content. After thermal holding treatment, the samples were water quenched in order to keep different level of Fe solute atoms in the matrix. Both of the thermal holding treatment time was designed long enough to reach the equilibrium condition of Fe solute atoms in solid aluminum. It can be assumed that the alloys after HT treatment contained about 0.04 wt.% Fe solute content and the alloys after LT treatment contained about 0.007 wt.% Fe solute contents according to the Al-Fe binary phase diagram [2].

Table 3.4 Parameters of the thermal holding treatment methods in this study.

Specimens	Alloys	Thermal holding treatment
A3L	L00	640°C/24 h + 500°C/24 h (LT)
A7L	H00	
A3H	L00	640°C/24 h (HT)
A7H	H00	

3.2 Microstructure observation

3.2.1 Optical microscopy (OM)

Optical microscope (Nikon Eclipse ME600, Fig. 3.1(a)) was used to examine the microstructures of experimental samples in both as-cast and extruded conditions. The samples were sectioned, mounted and metallographically polished. In addition, the image analyzer (CLEMEX JS-200, PE4.0) was used to measure the size, distribution and volume fraction of the iron-rich dispersoids.

3.2.2 Scanning electron microscopy (SEM)

A scanning electron microscope (SEM, JSM-6480LV, Fig. 3.1(b)) equipped with energy-dispersive X-ray spectroscopic (EDS) facilities were used to identify the iron-rich intermetallics in the as-cast samples and quantify the alloying elements in the intermetallics. In addition, SEM was also used to observe the particle distribution in the extruded samples. In order to have a better contrast, the specimens were etched in Keller's solution for 10 s before SEM observation.

3.2.3 Electron backscatter diffraction (EBSD)

The intermetallic phases in the as-cast samples were identified using the EBSD technique. Besides, EBSD analysis was performed to measure the grain and subgrain size of the samples using the linear intercept method [3]. The specimens for EBSD analysis were

the same as those used in the SEM analysis. An HKL channel 5 EBSD system equipped on the SEM (JSM-6480LV) was used for this investigation and the average subgrain size is from more than measured 200 subgrains in each sample.

3.2.4 Transmission electron microscopy (TEM)

Specimens for TEM observation were prepared in order to investigate the evolution of precipitates after extrusion as well as microstructure evolution during the creep process. To prepare the TEM specimens, some foils were cut from the transverse rod section into thin discs. They were mechanically ground to a thickness of 50 μm and followed by electropolishing in a twin-jet polishing unit, which was operated at 15 V and $-20\text{ }^{\circ}\text{C}$ using a 30% nitric acid and 70% methanol solution. The samples were observed under a TEM (JEM-2100) operated at 200 kV (Fig. 3.1(c)). In addition, X-ray energy-dispersive spectroscopy (EDS) attached to TEM was used to analyze the chemical composition of the dispersoids after extrusion.

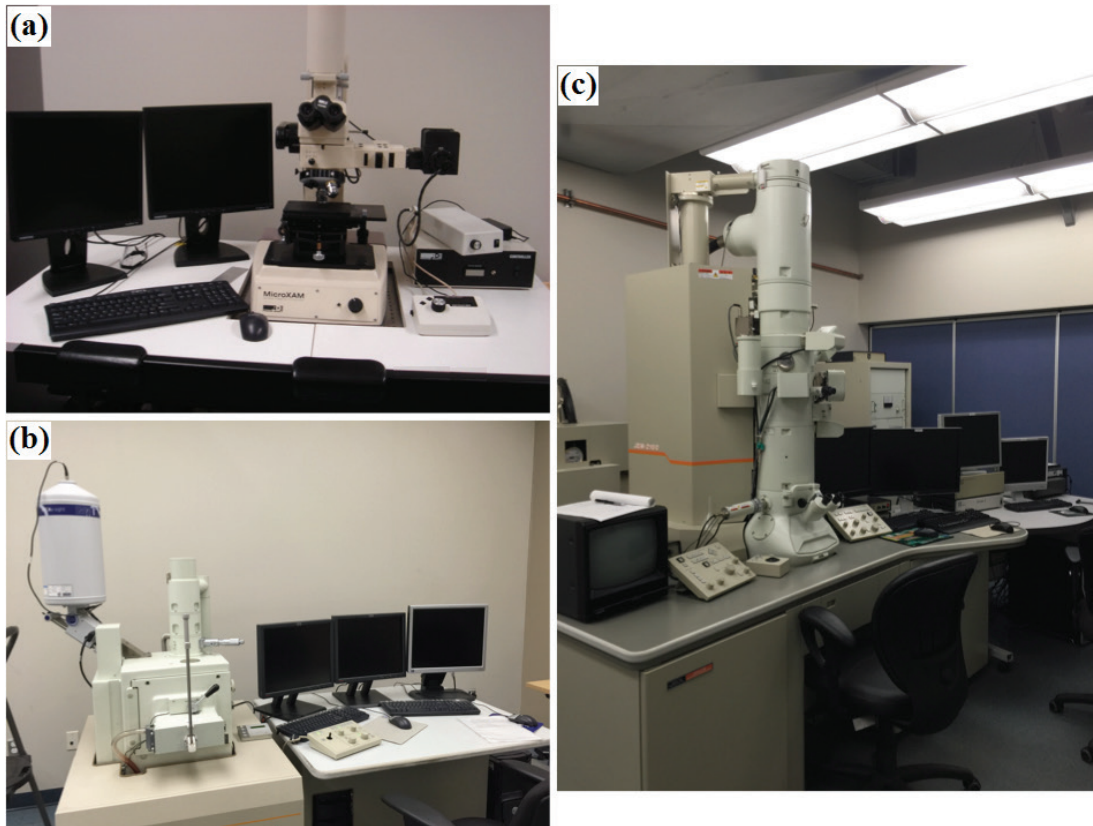


Fig. 3.1 Experimental equipment used in this work, (a) Optical microscopy (OM), (b) Scanning electron microscopy (SEM), and (c) Transmission electron microscopy (TEM).

3.3 Properties measurements

3.3.1 Electrical conductivity

The electrical conductivity of the as-cast billets was measured by electrical conductivity meter (SigmaScope SMP10, as presented in Fig. 3.2(a)). The as-cast specimens were polished to a surface roughness of around $1 \mu\text{m}$ before electrical conductivity test. Due to the small diameter of rods, their electrical conductivity cannot be measured directly from the electrical conductivity meter. Instead, the electrical resistance

was measured on the rods of 9.5 mm in diameter and 200 mm in length using Megger resistance ohmmeter (DLRO10HD, as shown in Fig. 3.2(b)). To ensure a thermal stability, all specimens were held at room temperature for 1 h before testing. For each alloy, one sample for the billet was tested on a minimum of 10 areas while three samples for rods were measured to obtain the average value.

3.3.2 Microhardness

To test the Fe solute content on strength, Vickers microhardness test was performed on the samples after different homogenization treatment according to the ASTM standard E92-82 using Micro Hardness Tester (HVS-1000 Digital, Fig 3.2(c)) [4]. The test load was fixed to be 50 g for an indentation time of 20 s, with the diagonal of impression in the range of 40–60 μm . All samples for hardness tests were polished to a surface roughness of around 0.05 μm . A minimum of 20 measurements was performed on each sample. The mean value and standard deviation were calculated as its hardness value.

3.3.3 Tensile test

Specimens for tensile tests were directly cut from the extrusion rods with 9.5 mm in diameter and 250 mm long according to ASTM B557 standard [5]. Then parts of the tensile testing rods were performed the annealing treatment at 350 $^{\circ}\text{C}$ for 4 h in order to simulate a real condition for the conductors in the industry application.

Tensile tests were conducted on the as-extruded and as-annealed rods at room temperature at a crosshead speed of 0.5 mm/min using electromechanical testing machine (Instron 8801 tensile test system, Fig. 3.2(d)). During the testing, an extensometer with gauge length of 25 mm was used for the determination of displacement. Both the yield strength (YS) and ultimate tensile strength (UTS) were obtained from the data acquisition system of the tensile test machine. For each alloy, a minimum of five tests was performed to obtain the average value for the yield strength, ultimate tensile strength and elongation.

3.3.4 Compression test

The yield strength (YS) at the temperature range of 100–200 °C was evaluated by the compression test. The tests on cylindrical specimens with an aspect ratio of 1.5 (dia: 9.5 mm, L_0 : 14.25 mm) were carried out using a Gleeble 3800 device (Fig. 3.2(e)). The specimens were deformed at 0.001 s^{-1} strain rate at 100, 150 and 200 °C with heating rate of 2 °C/s and 3 min stabilization time. The temperature is controlled by a K-thermocouple. An average value of YS was obtained from 3 tests.

3.3.5 Creep test

To investigate the creep properties of the rods with different Fe, Cu and Mg additions, the creep tests were conducted using the compression creep machine (Fig. 3.2(f)). The cylindrical specimens with a diameter of 9.5 mm and a length of 19 mm were prepared. To

investigate the effect of Fe addition on the creep properties, the compression creep tests were performed at a temperature range from 100 to 200 °C and under constant loads from 20 to 60 MPa while the creep tests were conducted at 100 °C for 100 hours by applying a constant load of 69 MPa to study the effect of Cu and Mg on the creep properties. The temperature for the specimen was determined using a thermocouple attached to the center of the gauge section, and the deformation of the specimen was recorded using a linear variable displacement transducer (LVDT). In order to ensure a thermal stability, all specimens were held at the test temperature for 1 h before loading.

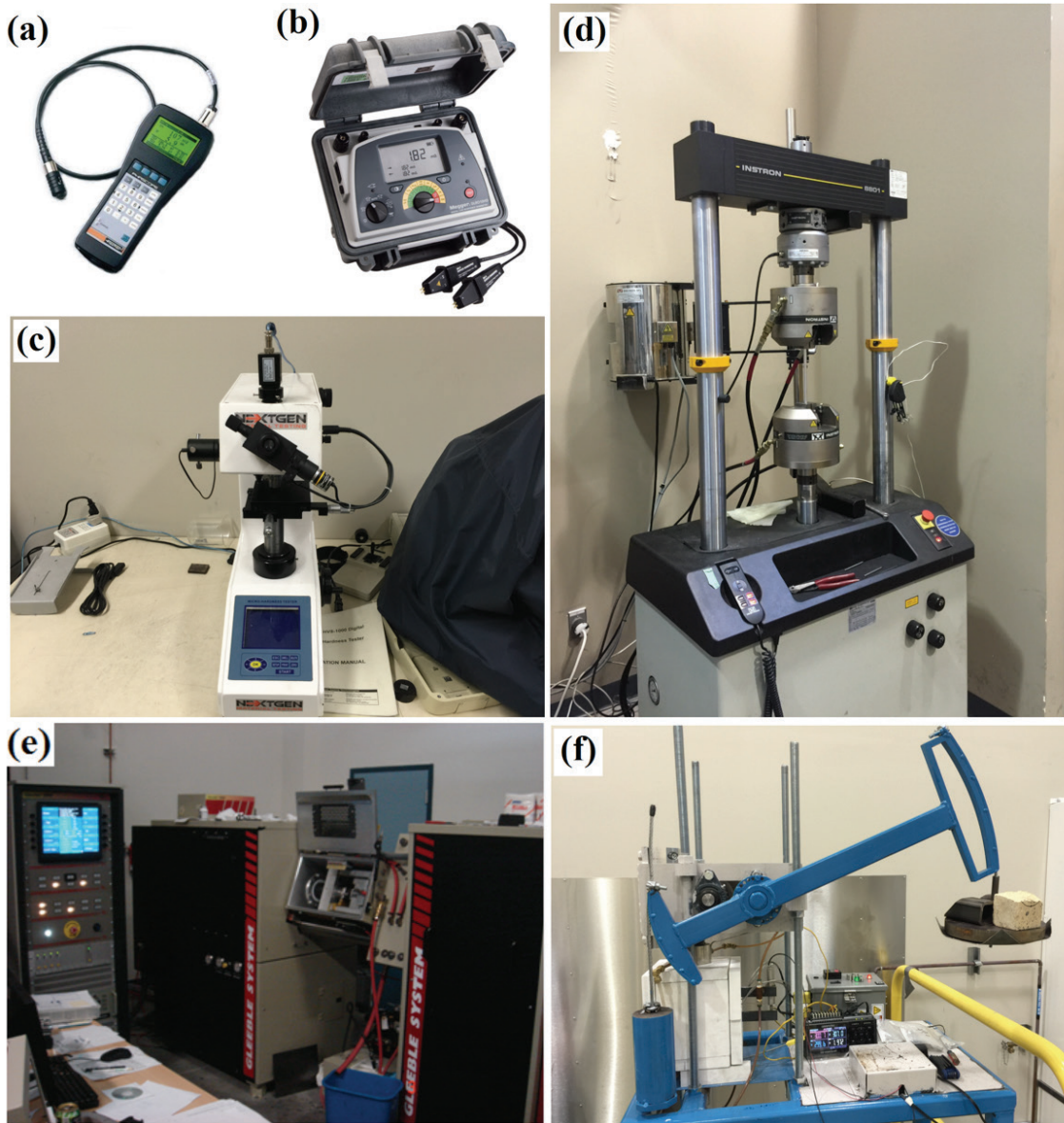


Fig. 3.2 Experimental equipment used in this work,

(a) SigmaScope SMP10 electrical conductivity meter,

(b) Megger resistance ohmmeter, (c) HVS-1000 Digital Micro Hardness Tester,

(d) Instron 8801 tensile test system,

(e) Gleeble 3800 device, and (f) compression creep test machine.

References

- [1] R.W. Westerman, Metall. Trans. 5 (1974) 667-672.
- [2] C.M. Allen, K.A.Q. O'Reilly, B. Cantor, P.V. Evans, Prog. Mater. Sci. 43 (1998) 89-170.
- [3] F.J. Humphreys, J. Mater. Sci. 36 (2001) 3833-3854.
- [4] ASTM E92-82(2003)e2, Standard Test Method for Vickers Hardness of Metallic Materials (Withdrawn 2010), ASTM International, West Conshohocken, PA, 2003.
- [5] ASTM B557-15, Standard Test Methods for Tension Testing Wrought and Cast Aluminum- and Magnesium-Alloy Products, ASTM International, West Conshohocken, PA, 2015.

CHAPTER 4
EFFECT OF FE ON MICROSTRUCTURE
AND PROPERTIES OF 8XXX
ALUMINUM CONDUCTOR ALLOYS

Chapter 4 Effect of Fe on microstructure and properties of 8xxx aluminum conductor alloys

Abstract

The effect of Fe contents (0.3–0.7 wt.%) on the microstructure, electrical conductivity, mechanical and creep properties of 8xxx aluminum alloy conductors was investigated. Results revealed that the as-cast microstructure of 8xxx alloys was consisted of equiaxed α -Al grains and secondary Fe-rich intermetallics distributed in the interdendritic region. The extruded microstructure showed partially recrystallized structure for 0.3% Fe alloy but only dynamically recovered structures for 0.5% and 0.7% Fe alloys. With increasing Fe contents, the ultimate tensile strength and yield strength were remarkably improved while the electrical conductivity was slightly decreased. Moreover, the creep resistance was greatly improved, which is attributed to the larger volume fraction of fine intermetallic particles and smaller subgrain size in the higher Fe contained alloys. The creep threshold stress was found to increase from 24.6 to 33.9 MPa with increasing Fe contents from 0.3% to 0.7%, respectively. The true stress exponent values were close to 3 for all three experimental alloys, indicating that the creep mechanism of 8xxx alloys was controlled by dislocation glide.

4.1 Introduction

Due to the low density and high conductivity to weight ratio, aluminum conductor alloys become an attractive candidate for replacing copper electric conductors in power building wiring [1-3]. Among those, 8xxx aluminum alloys are one of the most widely used aluminum conductor alloys, which were firstly developed to replace AA1350 conductor alloys for the overhead electrical transmission [4]. For conductor alloys, it is necessary to satisfy the requirements for electrical conductivity (EC), strength and creep resistance [5,6].

Fe is added in this alloy as the main alloying element to improve microstructural stability and mechanical properties [7,8]. Because of the low solubility of Fe in Al [9], most of Fe combines with both aluminum and silicon to form secondary intermetallic particles during casting, such as FeAl_3 , Al_mFe , Al_6Fe , and $\alpha\text{-AlFeSi}$ [10-12]. In the fabrication processes of aluminum electric conductors, the supply rods (9.53 mm in diameter) prior to wire drawing were either conventionally cast and hot-rolled or produced by continuous cast-rolling operation (Propezi process). During hot deformation the Fe-rich intermetallic particles were broken up into segments and distributed as fine dispersoids in aluminum matrix [13,14]. Addition of Fe is reported to play an important role in the hot deformation behavior [14,15]. However, little investigations have been conducted on the effect of Fe on the microstructure evolution and their consequent inference on materials properties of aluminum conductor alloys.

The creep resistance is one of the most important properties in aluminum conductor alloys [16-18]. To ensure high reliability in any further application of aluminum conductors, it is necessary to understand the effect of Fe on the creep behavior of aluminum conductor alloys. However, there have been controversial observations about effect of Fe on creep properties. Westerlund [16] found that addition of 0.65 wt.% Fe to Al-Fe alloy resulted in a significant reduction of the creep resistance. But, McQueen *et al.* [7] investigated the effect of Fe-rich intermetallic particles on the aluminum conductors and showed that addition of Fe could greatly improve the creep resistance for Al-Fe alloys (0.5–0.65 wt.% Fe). Up to day, limited data are available on the effect of Fe contents on the creep properties in 8xxx alloys at the common operating temperatures (up to ~100 °C) in the open literature, which is an important concern for their applications in the electric conductor industry.

The present work, therefore, aimed to investigate the effect of Fe contents on the evolution of microstructure, electrical conductivity, and mechanical and creep properties in 8xxx aluminum conductor alloys. The conventionally extruded 8xxx aluminum alloy conductors with different Fe contents were subjected to the compression creep test at 100 °C. The creep mechanism based on the creep threshold stress and true stress exponent is also explored to better understand the creep resistance in 8xxx aluminum alloys.

4.2 Material and methods

The experiments were conducted on 8xxx Al alloys with different Fe contents ranging from 0.3% to 0.7% (all alloy compositions in this work are in wt.% unless otherwise indicated). The chemical compositions of experimental alloys are listed in Table 4.1. All the samples (equivalent to the industrial 9.53 mm supply rods for drawn wire) were produced by the hot extrusion from DC cast billets.

Table 4.1 Chemical composition of experimental alloys studied (wt.%).

Alloy	Fe	Cu	Mg	Si	Mn	Al
Al3 (0.3Fe)	0.3	0.18	0.001	0.023	0.003	Bal.
Al5 (0.5Fe)	0.5	0.18	0.001	0.027	0.004	Bal.
Al7 (0.7Fe)	0.7	0.19	0.001	0.042	0.003	Bal.

The electrical conductivity measurement was directly carried out on the samples of 9.53 mm in diameter and 200 mm in length using Megger DLRO10HD resistance ohmmeter. Tensile tests were conducted on cylindrical samples of 9.53 mm in diameter and 250 mm long according to ASTM B557 standard at room temperature. The compressive creep tests were performed at 100 °C using cylindrical specimens (9.5 mm in diameter and 19 mm in length) under a constant stress that varied between 35 and 69 MPa. After the creep test, the samples were water quenched to the room temperature in order to examine the microstructure evolution.

The as-cast and extruded samples were polished and etched by the Keller's solution for 10 s, and then observed using optical microscope (OM), scanning electron microscope (SEM) and electron backscattered diffraction (EBSD) technique. All the extruded samples were sectioned parallel to the extrusion direction along the centerline and followed by the standard metallographic preparation. The automated EBSD maps were conducted with 1.0 μm step size for as-cast grain structure and with a scanning step size of 0.2 μm for the extruded structure. The subgrain sizes of the extruded samples were measured using linear intercept method [19]. In addition, the samples after creep tests at 69 MPa and 100 °C were selected to investigate the microstructure evolution using transmission electron microscope (TEM), which was operated at 200 kV. TEM samples with a thickness of 35–60 μm were prepared by mechanically grinding and electropolishing in a solution of 30% nitric acid and 70% methanol at 15 V and -20 °C.

4.3 Results and discussion

4.3.1 Microstructures of as-cast and extruded materials

Fig. 4.1 shows the optical micrographs of as-cast 8xxx aluminum alloys prior to hot extrusion with different Fe contents (0.3%, 0.5% and 0.7%). All the alloys had similar microstructure that is consisted of equiaxed α -Al grains and secondary Fe-rich intermetallics distributed in the interdendritic region (Fig. 4.1). It can be seen that the amount of the intermetallics increases with increasing Fe contents. As shown in Fig. 4.2, the

appearance of the intermetallic phase (arrows in Fig. 4.1) is feathery-like Al-Fe phase, confirmed by SEM-EDS (Fig. 4.2(b)). Those intermetallics are identified as tetragonal Al_mFe phase by EBSD results (Fig. 4.2(c) and 2(d)). In previous study [16,14], these intermetallics were defined as Al_6Fe or $FeAl_3$ phase, which was only based on SEM-EDS qualitative results. The as-cast grain structure is refined due to the restriction effect of intermetallic particles. The average grain sizes measured by EBSD are 86, 77 and 71 μm for the alloys containing 0.3%, 0.5% and 0.7% Fe, respectively.

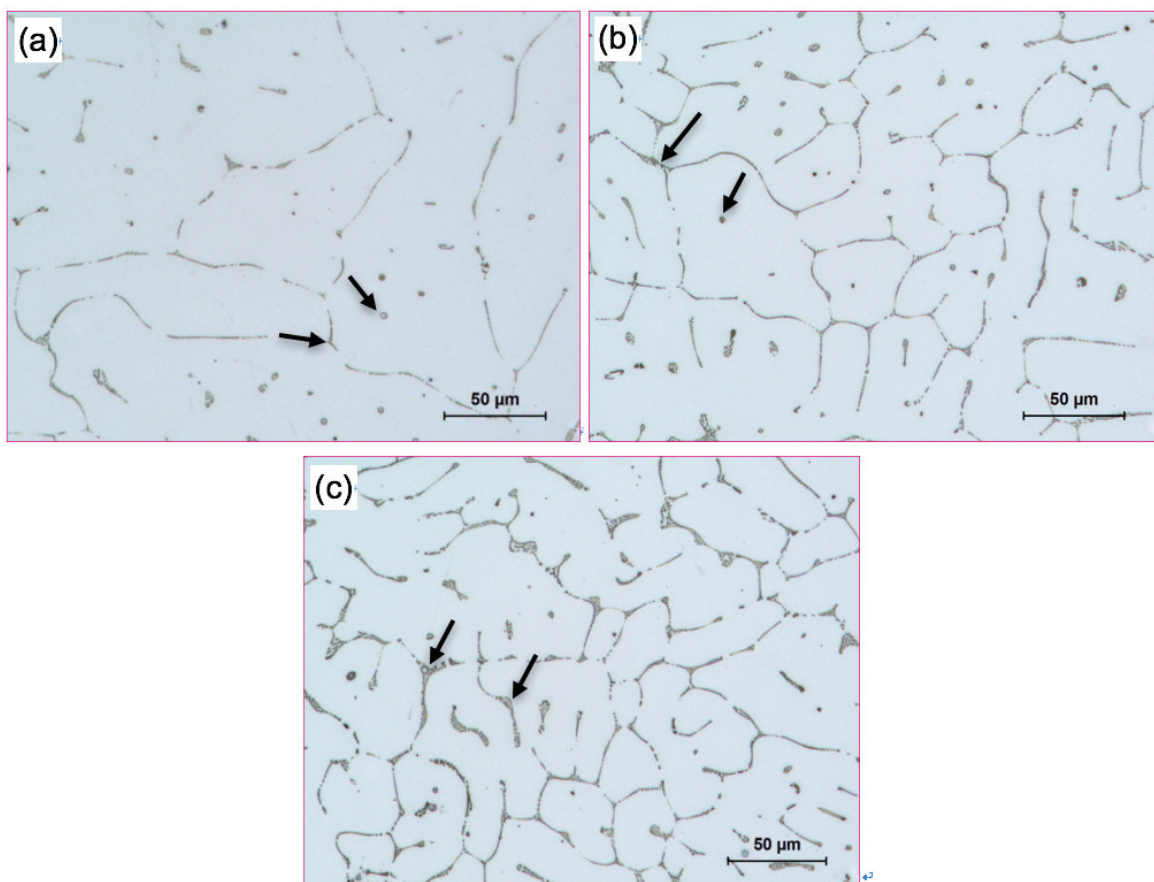


Fig. 4.1 Optical micrographs showing the as-cast grain structures: (a) Al3; (b) Al5; (c) Al7.

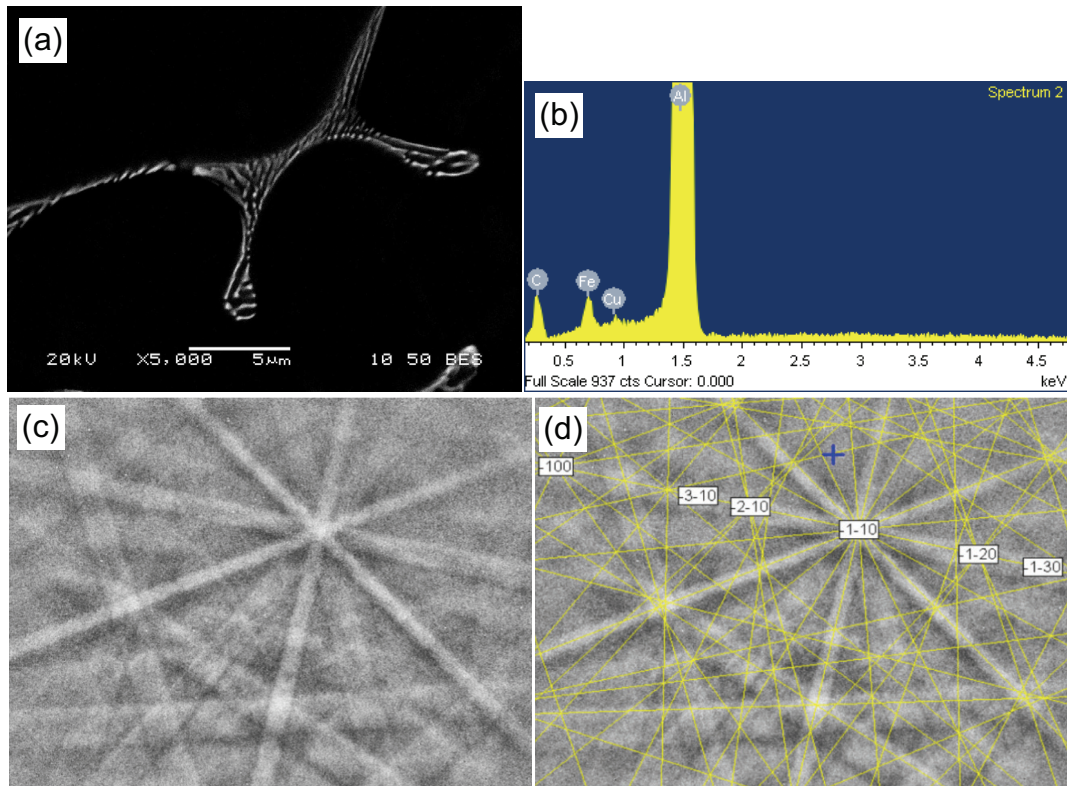


Fig. 4.2 Typical characteristics of Fe-rich intermetallics in Fig. 4.1: (a) SEM micrograph; (b) EDS spectrum; (c) EBSD pattern; (d) simulated solution of EBSD pattern, identifying Al_mFe phase with a lower mean angular deviation of 0.315.

Fig. 4.3 shows the optical images of the extruded samples. The hot extrusion fragmented and broke down intermetallic networks into fine particles which distributed along the extrusion direction in the aluminum matrix. For all the alloys, the Fe-rich intermetallic particles in extruded samples were small and fairly uniformly distributed throughout the matrix. The average size of intermetallic particles was measured to be a similar value of $\sim 0.38 \mu\text{m}$ for all three alloy samples. However, the volume fraction of intermetallic particles is increased from 1.9% in Al3 alloy to 3.2% in Al5 alloy and further to 4.4% in Al7 alloy, respectively.

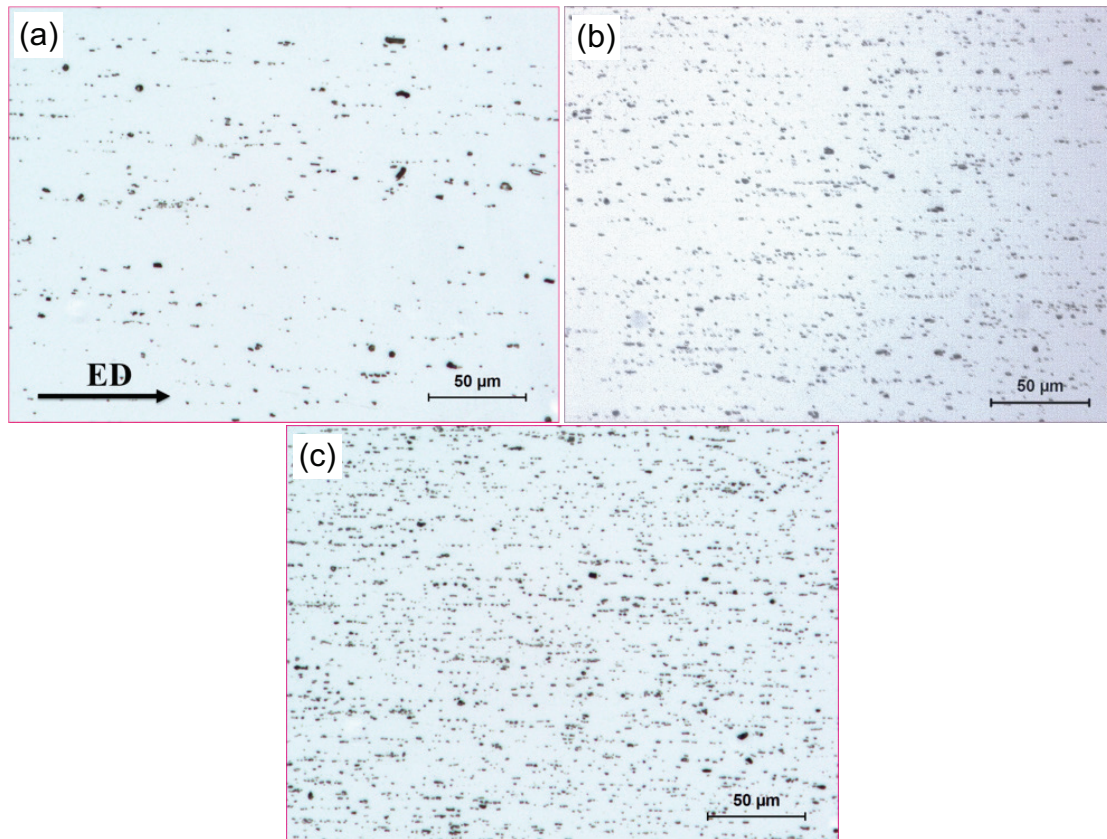


Fig. 4.3 Optical micrographs of the extruded samples: (a) Al3; (b) Al5; (c) Al7, showing fine Fe-rich intermetallic particles distributed along the extrusion direction (ED).

Fig. 4.4 shows the EBSD orientation maps of extruded samples of Al3, Al5 and Al7 alloys. In the orientation imaging maps, the boundaries of grains and subgrains are defined as follows: white lines: 1–5°, blue lines: 5–15°, thin black lines: 15–30° and thick black lines: (> 30°). When the DC cast billets were extruded to the rods, the original grains of three alloys were severely torn and broke into the irregular deformation bands along the elongated grains. A large amount of low-angle boundaries with misorientation angles between of 1° and 5° were created, indicating a high number density of subgrain structure.

Meanwhile, the substructures were well organized and fine subgrains were formed with neatly arranged boundaries of $1-15^\circ$, which suggests the dynamic recovery occurred, involving the annihilation and rearrangement of dislocations [20]. For Al3 alloy as indicated by arrows in Fig. 4.4(a), small equiaxed grains with high-angle boundaries ($>15^\circ$) that contained substructures were observed along the elongated grain boundaries, indicating partially dynamic recrystallization occurred during extrusion. However, only dynamically recovery was observed in the alloys containing 0.5% and 0.7% Fe (as shown in Figs. 4.4(b) and (c)), which was resulted from the inhibition effect of high volume fraction of Fe-rich intermetallic particles on dynamic recrystallization. As measured from EBSD orientation maps (Fig. 4.4), the average subgrain sizes decreased from 3.9, 3.2 to 2.8 μm as the Fe content increased from 0.3% to 0.5% and further to 0.7%, respectively. The increased volume fraction of Fe-rich intermetallic particles in the alloys containing high Fe generated a stronger pinning effect on substructures and led to a decrease in subgrain size [15].

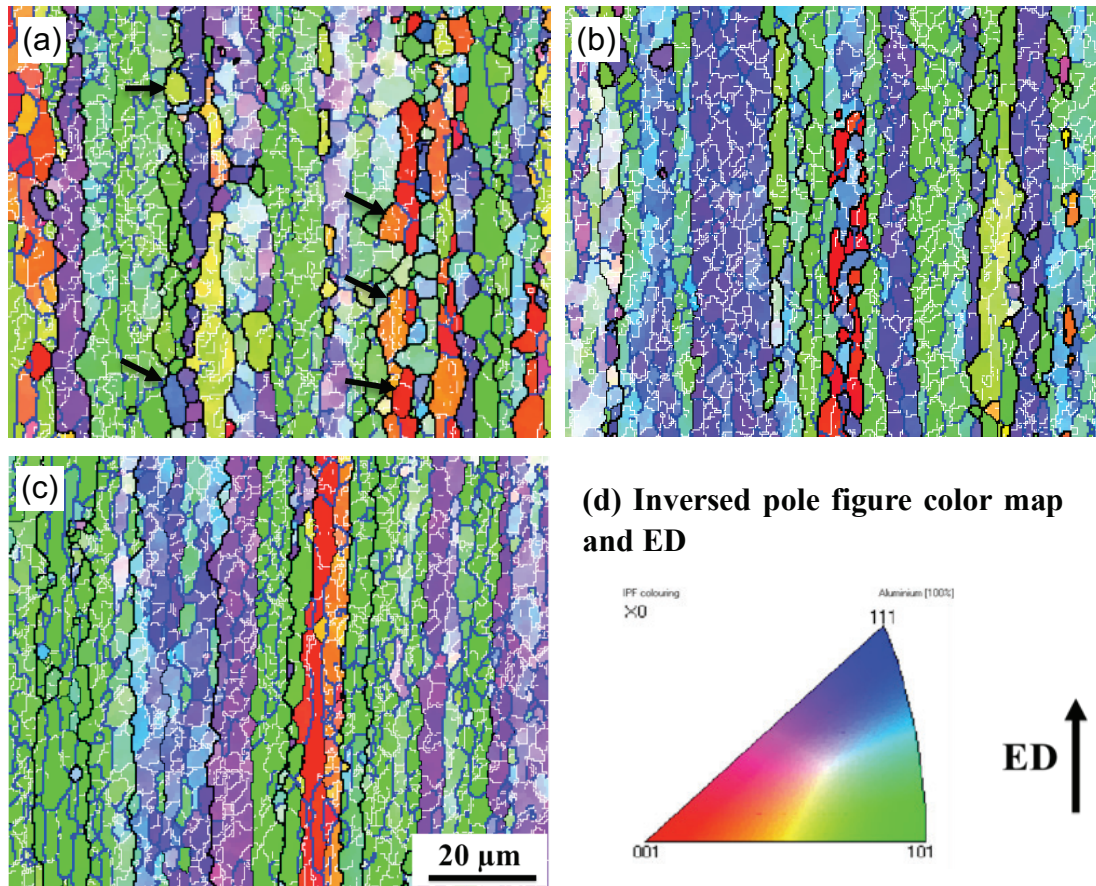


Fig. 4.4 Orientation imaging maps of the extruded samples with different Fe contents: (a) Al3; (b) Al5; (c) Al7; (d) Inversed pole figure color map and extrusion direction (ED).

4.3.2 Effect of Fe on mechanical and electrical properties

Fig. 4.5 shows the evolution of ultimate tensile strength (UTS), yield strength (YS), elongation and electrical conductivity (EC) with different Fe contents. It can be found that both UTS and YS increase while the elongation barely changes with increasing Fe contents from 0.3% to 0.7% (Fig. 4.5(a)). The UTS and YS of Al3 alloy are 108 MPa and 91 MPa, respectively. As the Fe contents increase to 0.5% and 0.7%, the UTS and YS increase

approximately by 8% and 10% for Al5 alloy and 25% and 28% for Al7 alloy, respectively. Meanwhile, the EC of samples moderately decreases with an increase of Fe content (as shown in Fig. 4.5(b)). The EC of Al3 alloy is 61.1 %IACS and it decreases to 60.5% for Al5 alloy and 59.7% for Al7 alloy, respectively.

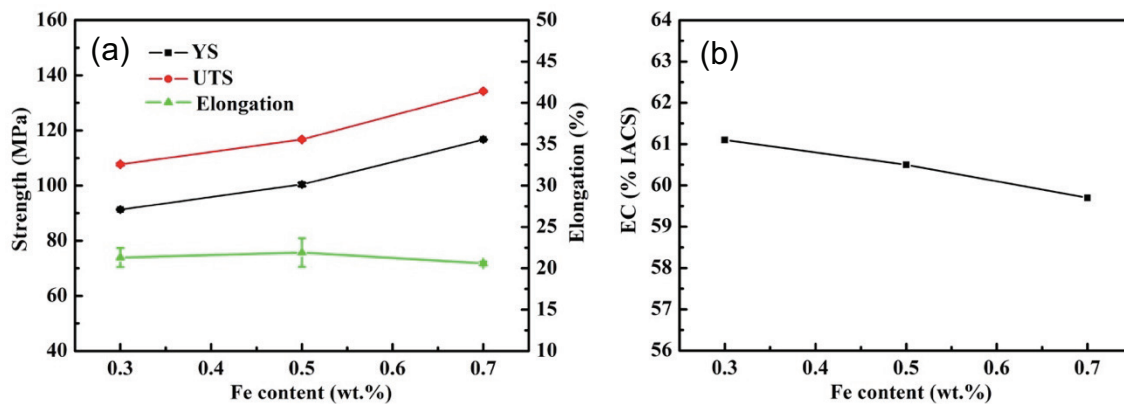


Fig. 4.5 Evolution of mechanical properties (a) and EC (b) with different Fe contents.

In the extruded samples, there were a large number of Fe-rich intermetallic particles with an average size of $0.38 \mu\text{m}$ present (Fig. 4.3). With increase of Fe contents, the volume fraction of Fe-rich intermetallic particles increases and those particles can act as obstacles to the movement of dislocation and block of the migration of grain boundaries, leading to the improvement of both UTS and YS. Besides the intermetallic particles, with increase of Fe contents the recrystallization grains disappeared and the subgrains became smaller (Fig. 4.4), which provided more obstacles for dislocation motion and thus improved tensile properties. On the other hand, the intermetallic particles present in aluminum matrix created a number of defects in the crystal structure. Those intermetallic particles and its related crystal defects

hindered the free movement of electrons, resulting in a decrease in the electrical conductivity with an increase of Fe contents.

In the industrial practice, the annealing after wire drawing is often used to improve the electrical conductivity of conductor products. Fig. 4.6 shows the mechanical properties and EC after annealing treatment at 350 °C for 4 h for three different Fe contained alloys. It is noted the EC increases more than 1% for all three alloys compared to that before annealing and their values are 62.0 %IACS for Al3 alloy, 61.7% for Al5 alloy and 61.1% for Al7 alloy, respectively. For some critical applications where EC is the primary concern, even with higher Fe contents, both Al5 and Al7 alloys can fulfill the minimum requirement as conductors ($EC \geq 61.0$ %IACS). However, The UTS and YS considerably decrease after annealing for all three alloys. There is a trade-off between the strength and EC when the annealing process is applied.

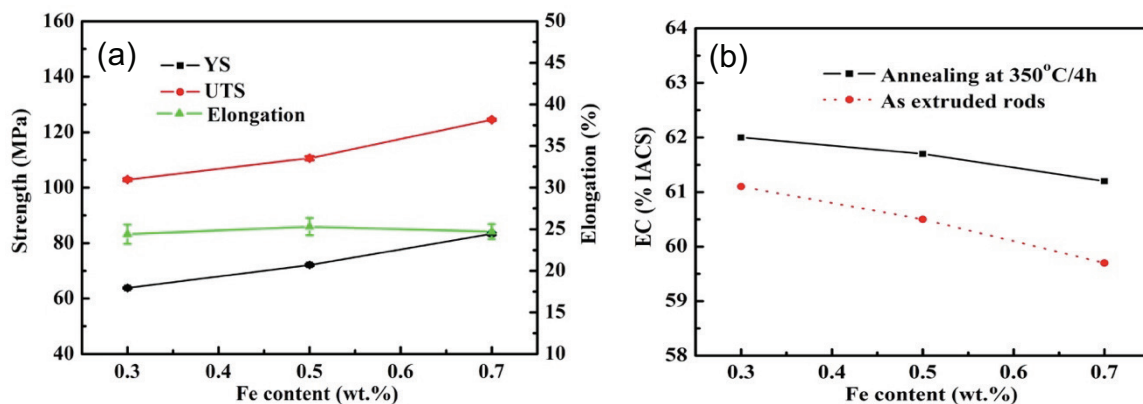


Fig. 4.6 Mechanical properties (a) and EC (b) of the samples after annealing at 350 °C for 4 h.

4.3.3 Effect of Fe on creep properties

Fig. 4.7 shows typical creep curves of extruded Al3, Al5 and Al7 samples tested at 100 °C under a constant stress of 69 MPa, which is close to the compressive YS at 100 °C (73 MPa of Al3 alloy). It can be clearly seen from Fig. 4.7(a) that the total strain after 100 h test decreases from the low Fe alloy (Al3) to the high Fe alloy (Al7). In compressive creep tests, the creep strain increases rapidly at the beginning of the creep deformation, which can be defined as the primary creep stage where the creep rate dramatically decreased with creep time. The creep strain then rises more slowly with increasing time and the primary creep stage gradually transits to a stage where the creep rate becomes more and less constant (quasi-steady stage). As indicated in Fig. 4.7(b), the minimum creep rate, $\dot{\epsilon}_m$, is calculated as the average creep rate in the quasi-steady stage, and the results demonstrate that with increasing Fe content from 0.3% to 0.7%, the minimum creep rate significantly decreases from $7.5 \times 10^{-8} \text{ s}^{-1}$ (Al3 alloy) to $1.8 \times 10^{-8} \text{ s}^{-1}$ (Al5 alloy) and further to $5.6 \times 10^{-9} \text{ s}^{-1}$ (Al7 alloy), respectively, indicating a strong benefit of Fe on improving the creep resistance.

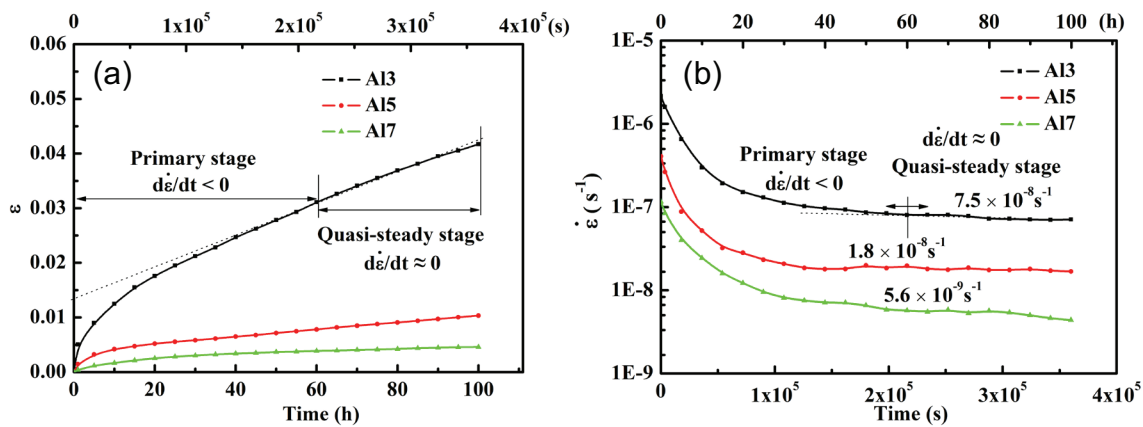


Fig. 4.7 Typical creep strain (ϵ) (a) and instantaneous creep rate ($\dot{\epsilon}$) (b) curves of the samples with different Fe contents, tested at 100 °C and 69 MPa.

To further understand the creep behavior of 8xxx conductor alloys, various loads in the range of 35–69 MPa were applied for the creep tests at the same temperature (100 °C). Figure 4.8 shows the minimum creep rate, $\dot{\epsilon}_m$, as a function of the applied stress for three alloys. It is apparent that at any given stress, the minimum creep rate remarkably decreased from Al3 alloy to Al7 alloy. In other words, the creep resistance of 8xxx conductor alloys clearly increases with increasing Fe contents. By extrapolating the linear fitted curves to the creep rate value of 10^{-10} s^{-1} , the threshold stress, σ_{th} , below which the creep is not experimentally measurable, can be determined for each alloy. The values of threshold stresses are calculated to be 24.6 MPa (Al3 alloy), 30.1 MPa (Al5 alloy) and 33.9 MPa (Al7 alloy), respectively (Fig. 4.8). It is evident that the creep threshold stress increases with increasing Fe contents. The origin of the threshold stress in dispersion strengthened alloys is assumed to be the interaction between the dislocations and dispersion particles. The common explanation for σ_{th} is the presence of an additional stress to bow the dislocation

between the particles, corresponding Orowan stress [21]. Arzt *et al.* [22,23] considered that the threshold stress was the stress required to detach a dislocation from an obstacle or the additional stress required for climbing over an obstacle.

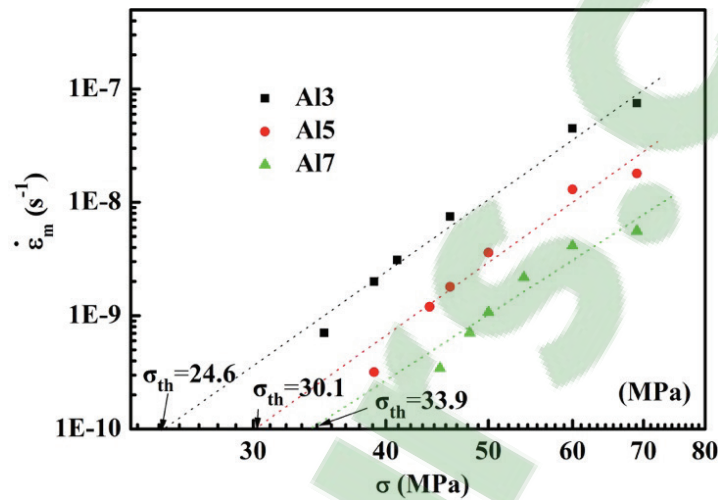


Fig. 4.8 Double logarithmic plot of the minimum creep rate $\dot{\epsilon}_m$ against applied stress σ for Al3, Al5, and Al7 alloys.

After determining the threshold stress, the creep behavior of dispersion strengthened materials can be generally described by a modified power law equation as follows [24]:

$$\dot{\epsilon}_m = A_0 \left(\frac{\sigma - \sigma_{th}}{G} \right)^{n_t} \exp \left(- \frac{Q}{RT} \right) \dots \dots \dots \text{(Eq. 4.1)}$$

where $\dot{\epsilon}_m$ is the minimum creep rate, A_0 is a dimensionless constant, G is the shear modulus; n_t is the true stress exponent, Q is the activation energy, R is the universal gas constant and T is the absolute temperature, σ is the applied stress and σ_{th} is the threshold stress. Fig. 4.9 shows the double logarithmic plot of the minimum creep rate, $\dot{\epsilon}_m$, over the effective stress, $\sigma - \sigma_{th}$, and the slope of plots gives the true stress exponent n_t . It can be

found that the values of n_t are in a range of 2.5–3.3 for three alloys with different Fe contents, which can be used to assess the mechanisms governing creep deformation. The creep behavior of aluminum alloys related to three relevant deformation mechanisms are the dislocation glide ($n_t = 3$), dislocation climb ($n_t = 5$) and invariant substructure model ($n_t = 8$) [25-27]. In the present study, the values of the true stress exponent, n_t , are close to 3, indicating that the creep process is controlled by dislocation glide, which is also confirmed by Jaffe and Dorn that dislocation glide mechanism was responsible for room temperature creep in pure aluminum [28,29].

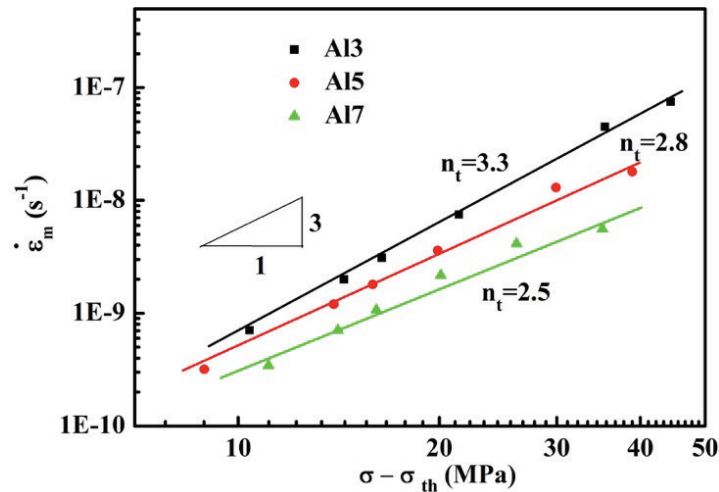


Fig. 4.9 Double logarithmic plot of minimum creep rate $\dot{\epsilon}_m$ vs effective stress $\sigma - \sigma_{th}$ for Al3, Al5 and Al7 alloys.

Though the creep properties vary with Fe contents, as shown in Figs. 4.7 and 4.8, however, the creep behaviours are confirmed to be controlled by the dislocation glide for all experimental Al3, Al5 and Al7 alloys with a similar n_t in Fig. 4.9. Therefore, the factors that can have effect on the movement of dislocations during creep are expected to influence the

creep properties, which principally are the fine intermetallic particles and subgrains in the present work. It is observed that dislocations are piled-up at intermetallic particles, as shown in Fig. 4.10(a), confirming the inhibiting effect of intermetallic particles on dislocations and their influence on creep properties. Besides, the threshold stress originates from the dislocation looping over the particles (Orowan stress, σ_{or}) can be evaluated from Eq. 4.2 [21,24]:

$$\sigma_{or} = 0.84M \frac{Gb}{d} \left(\sqrt{\frac{\pi}{4f}} - 2 \right)^{-1} \dots\dots\dots \text{(Eq. 4.2)}$$

where M is Taylor factor, d is average particle diameter, and f is the particle volume fraction. In the present work, d is the same value ($\sim 0.38 \mu\text{m}$) in all three alloys but the particle volume fractions, f , are 1.9% in Al3 alloy, 3.2% in Al5 alloy and 4.4% in Al7 alloy, respectively (Fig. 4.3). Hence, the Orowan stress σ_{or} has been calculated to be 10.7 MPa in Al3, 16.0 MPa in Al5, and 21.2 MPa in Al7 alloys, respectively. It is apparent that the increased volume fraction of intermetallic particles (f) results in the rising σ_{or} due to the increment in the interaction between fine particles and dislocations.

However, the calculated values, σ_{or} , are smaller than the experimentally determined values, σ_{th} , (Fig. 4.8). This could be likely attributed to the synergy effect of other minor and trace elements (such as Cu, Si) in aluminum matrix, which can also contribute to the part of σ_{th} [30,31]. In addition, the effect of solute atoms should be same due to a similar solution level of solute atoms in all three experimental alloys, which can be confirmed by the liner fit between σ_{th} and σ_{or} in Fig. 4.11. Therefore, with increasing Fe contents, the volume fraction

of intermetallic particles rises, which leads to increasing the Orowan stress, σ_{or} and experimental stress σ_{th} , resulting in a significant improvement of the creep resistance.

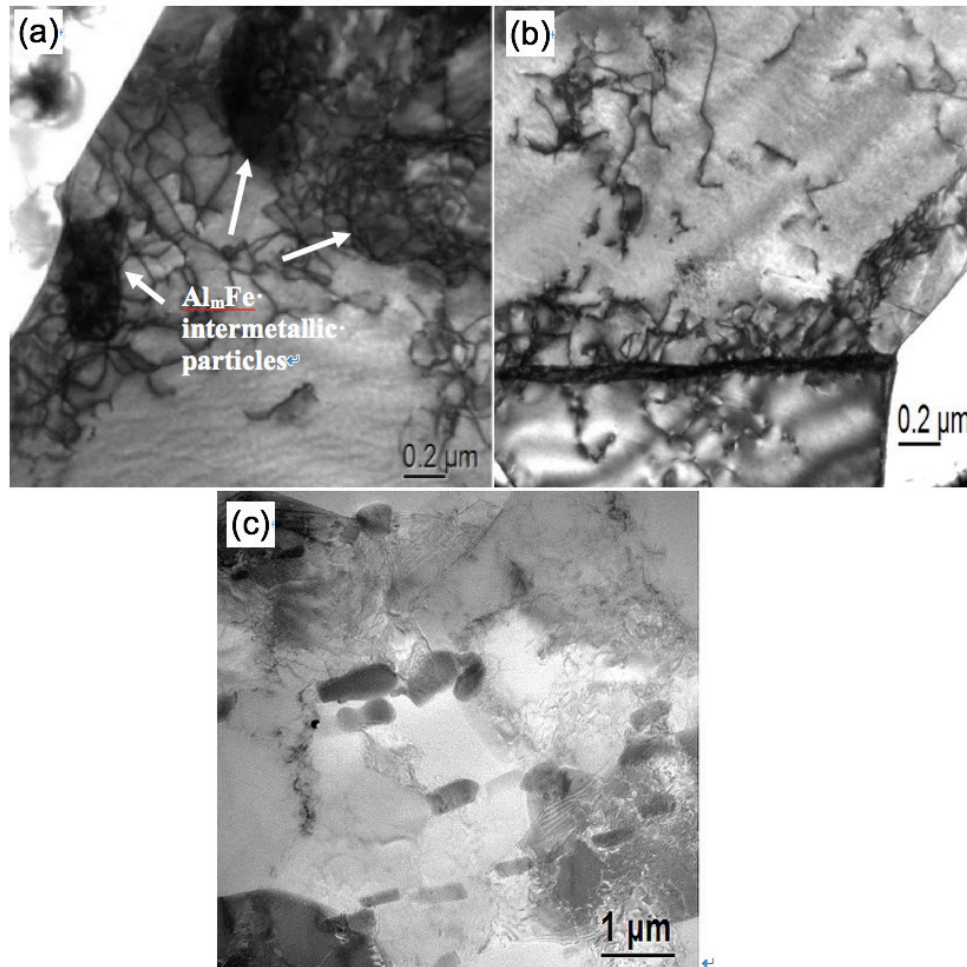


Fig. 4.10 TEM bright field images of Al₃ samples after creep at 100 °C and 69 MPa, representing interaction between dislocations and dispersion particles: (a) dislocation pile-up at Al_mFe intermetallic particles, (b) subgrain boundary blocking the dislocation motion, and (c) intermetallic particles distributed on subgrain boundaries.

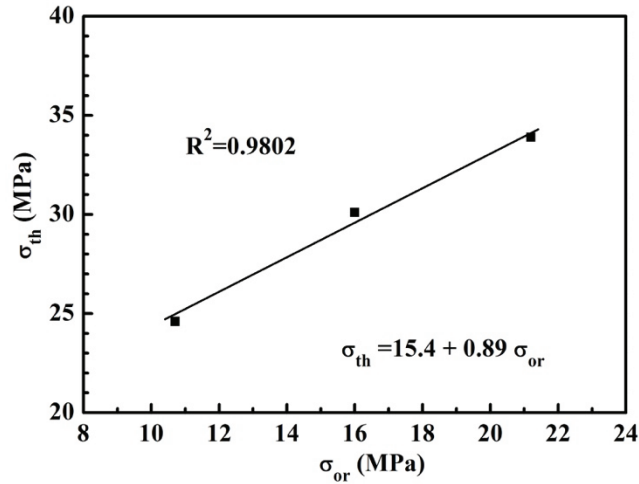


Fig. 4.11 Relation between the threshold stress, σ_{th} and Orowan stress, σ_{or} .

In addition, as shown in Fig. 4.10(b), entangled dislocations interacted with subgrain boundaries and became immobilized, suggesting the beneficial effect of subgrains on the creep resistance. At relatively high temperature ($> 0.5 T_m$), subgrain boundaries are generally considered to be harmful to the creep properties due to their unstable and easily-sliding features during creep. However, the creep testing temperature is relatively low ($\leq 0.4 T_m$) in the present study and the dislocation glide controls the creep deformation (Fig. 4.9), indicating an absence of subgrain boundaries sliding [32], which is further confirmed by the TEM observation. Fig. 4.10(b) illustrates that the subgrain boundary can also act as barriers for dislocation motion during creep deformation and Fig. 4.10(c) shows that a large part of the intermetallic particles distribute on the subgrain boundaries, which increases the pinning effect on subgrain boundaries and hence enhances the subgrain stability. Thus, the presence of fine subgrains results in a positive strengthening effect on creep properties. As demonstrated in Fig. 4.4, the subgrain size decreased with increasing Fe

contents, which reduces the mean free path for dislocation movement and generates an additional contribution to a better creep resistance.

4.4 Conclusions

The effects of Fe contents on microstructure and properties of 8xxx aluminum conductor alloys were investigated. The following conclusions can be drawn:

1. The as-cast microstructure of 8xxx alloys was consisted of equiaxed α -Al grains and secondary Fe-rich intermetallics distributed in the interdendritic region. The deformed microstructure showed partially recrystallized structure for 0.3% Fe alloy but only dynamically recovered structures for 0.5% and 0.7% Fe alloys. The volume fraction of fine intermetallic particles increased and the subgrain size decreased after hot deformation with increasing Fe contents.
2. As the amount of Fe increased from 0.3% to 0.7%, UTS and YS increased by 25% and 28% while EC decreased by 2.3%, respectively. After annealing at 350 °C for 4 h, EC increased more than 1% for all three alloys compared to that before annealing alloy in the trade-off with reduced tensile strength.
3. Addition of Fe to 8xxx alloys greatly improved the creep resistance. With increase of Fe content from 0.3% to 0.5% and 0.7%, the minimum creep rate significantly decreased from $7.5 \times 10^{-8} \text{ s}^{-1}$ to $1.8 \times 10^{-8} \text{ s}^{-1}$ and further to $5.6 \times 10^{-9} \text{ s}^{-1}$, respectively, for creep tests at 100 °C with a constant load of 69 MPa.

4. With increasing Fe contents from 0.3% to 0.5% and 0.7%, the creep threshold stress greatly increased from 24.6 to 30.1 and 33.9 MPa, respectively.

5. The introduction of the threshold stress in the analysis resulted in that the true stress exponent values were close to 3 for all three experimental alloys, indicating that the creep mechanism of 8xxx alloys is controlled by dislocation glide. The presence of larger volume fraction of fine intermetallic particles and smaller subgrain size in the higher Fe contained alloys are responsible for the better creep resistance.

References

- [1] M.Y. Murashkin, I. Sabirov, X. Sauvage, R.Z. Valiev, *J. Mater. Sci.* 51 (2016) 33-49.
- [2] W.H. Yuan, Z.Y. Liang, *Mater. Des.* 32 (2011) 4195-4200.
- [3] L. Pan, B. Bourassa, X.G. Chen, *Aluminium Alloys 2014 - ICAA14* 794-796 (2014) 1121-1126.
- [4] C. Olin, in: *U.S.P. 3711339* (Ed.), US, 1973.
- [5] K.M. Hussain, D. Hussain, *Telecommunications and networks*, Butterworth Heinemann, Oxford; Boston, 1997.
- [6] C. Hunter, *Aluminum Building Wire Installation and Terminations* (2006).
- [7] H.J. Mcqueen, E.H. Chia, E.A. Starke, *JOM* 38 (1986) 19-24.
- [8] T.D. Ma, Y. Su, Q. Wang, J.L. Li, *Adv. Eng. Mater.* 750-752 (2013) 711-714.
- [9] O.D. Sherby, A. Goldberg, O.A. Ruano, *Philos. Mag.* 84 (2004) 2417-2434.
- [10] P. Skjerpe, *Metall. Trans. A* 18 (1987) 189-200.
- [11] C.M. Allen, K.A.Q. O'Reilly, B. Cantor, P.V. Evans, *Prog. Mater. Sci.* 43 (1998) 89-170.
- [12] M. Shakiba, N. Parson, X.G. Chen, *Mater. Sci. Eng. A* 619 (2014) 180-189.
- [13] D. Kalish, B.G. Lefevre, S.K. Varma, *Metall. Mater. Trans. A* 8 (1977) 204-206.
- [14] H.J. Mcqueen, K. Conrod, G. Avramovic-cingara, *Can. Metall. Quart.* 32 (1993) 375-386.
- [15] M. Shakiba, N. Parson, X.G. Chen, *J. Mater. Eng. Perform.* 24 (2015) 404-415.
- [16] R.W. Westerlund, *Metall. Trans.* 5 (1974) 667-672.

-
- [17] D.E. Newbury, *Anal. Chem.* 54 (1982) A059-A064.
- [18] E. Kandare, S. Feih, A. Kootsookos, Z. Mathys, B.Y. Lattimer, A.P. Mouritz, *Mater. Sci. Eng. A* 527 (2010) 1185-1193.
- [19] F.J. Humphreys, *J. Mater. Sci.* 36 (2001) 3833-3854.
- [20] C.J. Shi, W.M. Mao, X.G. Chen, *Mater. Sci. Eng. A* 571 (2013) 83-91.
- [21] E. Orowan, *Dislocation in Metals*, AIME, New York, M. Cohen(Ed), 1957.
- [22] E. Arzt, D.S. Wilkinson, *Acta Metall.* 34 (1986) 1893-1898.
- [23] E. Arzt, J. Rosler, *Acta Metall.* 36 (1988) 1053-1060.
- [24] R.A. Karnesky, L. Meng, D.C. Dunand, *Acta Mater.* 55 (2007) 1299-1308.
- [25] Y. Li, T.G. Langdon, *Mater. Sci. Eng. A* 265 (1999) 276-284.
- [26] F. Dobes, P. Kratochvil, *Intermetallics* 43 (2013) 142-146.
- [27] Z.G. Lin, F.A. Mohamed, *J. Mater. Sci.* 47 (2012) 2975-2984.
- [28] J.E. Dorn, N. Jaffe, *Trans. Met. Soc. AIME* 221 (1961) 229-233.
- [29] N. Jaffe, J.E. Dorn, *Trans. Met. Soc. AIME* 224 (1962) 1167.
- [30] O. Ryen, O. Nijs, E. Sjolander, B. Holmedal, H.E. Ekstrom, E. Nes, *Metall. Mater. Trans. A* 37A (2006) 1999-2006.
- [31] P.K. Chaudhury, F.A. Mohamed, *Metall. Mater. Trans. A* 18 (1987) 2105-2114.
- [32] V.K. Rao, D.M.R. Taplin, P.R. Rao, *Metall. Trans. A* 6A (1975) 77-86.

CHAPTER 5

**EFFECT OF FE-RICH INTERMETALLIC
PARTICLES AND FE SOLUTES ON
CREEP BEHAVIOR OF 8XXX
ALUMINUM CONDUCTOR ALLOYS**

Chapter 5 Effect of Fe-rich intermetallic particles and Fe solutes on creep behavior of 8xxx aluminum conductor alloys

Abstract

The compressive creep behavior of 8xxx aluminum conductor alloys, which contained 0.3 wt.% and 0.7 wt.% Fe and thermal holding treated at 640°C/24 h and 640°C/24 h + 500°C/24 h, were investigated at various temperatures (100–200 °C) and applied stresses from 20 to 60 MPa. Results showed that the creep resistance of the alloys is significantly improved by a large number of Fe-rich intermetallic particles and high Fe solutes in solid solution states restricting and impeding the dislocation movement. At 100 °C, Fe solute (0.023 wt.%) had the stronger effect in increasing the creep resistance than FeAl₃ particles (2.5 vol.%), while with increasing temperature to 150 and 200 °C, the high amount of FeAl₃ particles (2.5 vol.%) had a stronger effect than Fe solutes (0.023 wt.%). The threshold stress was found to increase with increasing of FeAl₃ particles and Fe solutes amount but decrease with increasing temperature. The increment of threshold stress due to FeAl₃ particles and Fe solutes is independent and the value is equal to sum of the individual contribution. The true stress exponent was calculated to be 3.1, 3.8, and 4.5 with increasing creep temperature from 100 to 150 and further to 200 °C, respectively.

5.1 Introduction

With the rapid growth in demand for wires and cables, the consumption of electric conductor materials has been significantly increased in the last decade [1-3]. Aluminum conductors have significant advantages in the electrical industry where weight and cost are major factors [4]. The mass resistivity of aluminum conductor is one-half of copper, which means only one-half the weight of aluminum is required for equivalent capacities [5], which led aluminum conductors to be an attractive alternative for replacing copper conductors in electrical application. Especially, the 8xxx aluminum conductor alloys are the most commercialized alloys, for example such as AA8030, used in the application of electrical distribution within buildings due to sufficient thermal stability to resist the creep deformation [6,7].

Fe is the main alloying element in 8xxx aluminum conductor alloys which traditionally used to enhance the strength of aluminum [5,8]. The strengthening effect was from the presence of small insoluble Fe-rich dispersion particles which were formed during solidification and fabrication process [5,9]. The presence of these particles promotes the retardation of dislocation glide and climb [6,10] and stabilizing the substructure [11]. Zhang *et al.* [6] reported that the addition of 0.7 wt.% Fe greatly improved the creep resistance of Al-Fe-Cu alloy due to presence of AlFe dispersoids. Besides, recent investigations have shown that Fe in solid solution has also a considerable effect on the creep properties of an alloy [12-16]. Sherby *et al.* [12] proposed that the diffusion of solute atoms within the

subgrain boundaries determined the rate-controlling creep process and observed a decreasing creep rate of pure aluminum after the trace addition of 0.054 wt.% Fe.

In general, in the alloys containing particles and solutes, a threshold stress σ_{th} may be existed, which is defined as the lowest limit stress below which the creep is not experimentally measurable [10,17,18]. The presence of a threshold stress contributes to the creep strength and affects the stress exponent, and the one with higher threshold stress leads to a better creep resistance [19,20]. Chaudhury *et al.* [15] observed that addition of 0.032 wt.% Fe solute atoms in Zn–Al alloy resulted in a considerable increase in creep resistance. Furthermore, Karnesky *et al.* [10] reported that in Al–Sc alloys containing two populations of particles, the strengthening effect was equivalent to the sum of the individual contribution. It is to be noted that, little attention has been paid on the combined effect through Fe-rich particles and Fe solutes on the creep deformation of aluminum alloys. Hence, an understanding of the effect of Fe-rich particles and Fe solutes on creep behavior of 8xxx aluminum conductor alloys is critical for the design of aluminum conductor materials.

Generally, temperature ranges for creep can be subdivided into three categories: (1) high temperature creep ($T > 0.6 T_m$), (2) intermediate temperature creep ($0.3 T_m < T < 0.6 T_m$), and (3) low temperature creep ($T < 0.3 T_m$) where T_m is the absolute melting point of the alloy [21]. However, most of the creep works were conducted at high temperatures $T > 0.5 T_m$ [11,12,22]. Sherby *et al.* [12], studied the effect of Fe on the creep of aluminum at temperature higher than 200 °C ($T > 0.5 T_m$) and Marquis *et al.* [11] studied the presence of

threshold stress of Al–Sc alloys at 300 °C. Very few studies has paid attention to the intermediate temperature creep since the materials generally neither fail nor experience significant plasticity at relatively lower temperatures [21]. To the author’s knowledge, no systematic investigation has been yet focused to study the effect of Fe on the creep behavior of aluminum alloys at the intermediate temperature range ($0.4 \sim 0.5 T_m$), which seriously limits the further application of 8xxx aluminum conductor alloys [23]. Thus, the aim of the present work was to investigate the influence of both Fe-rich particles and Fe solutes on the creep behavior of 8xxx aluminum conductor alloys in the temperature range of 100–200 °C. Besides, the creep mechanism was discussed based on the values of the true stress exponent.

5.2 Material and experimental procedure

The material used in this study was an 8xxx aluminum alloy with 0.3% Fe (A3) and 0.7% Fe (A7) (all alloy compositions in this work are in wt.% unless otherwise indicated). The chemical compositions of experimental alloys are given in Table 5.1. The present alloys were produced and fabricated into 9.5 mm supply rods for drawn wire by hot extrusion from DC cast billets. Details of the fabrication process were described in elsewhere [2]. The experimental alloys with two Fe contents were designed to have different amounts of Fe-rich particles to quantify the effect of Fe-rich particles on the creep properties. Besides, to have large difference of Fe solute levels in aluminum matrix, the alloys were subjected to two thermal holding treatments, one at 640 °C for 24 h (high thermal, HT) and another with

two step treatments (low thermal, LT): 640 °C for 24 h (aimed to obtain similar grain structure and same type of Fe-rich particles as HT treatment) + 500 °C for 24 h (aimed at getting the low Fe solute content in aluminum due to the temperature dependent solubility [12,24]). These conditions were designated as A3H and A3L for A3 alloys after HT and LT treatments, and A7H and A7L for A7 alloys after HT and LT treatments, respectively. All thermal holding treatments were followed by a directly water quench in order to keep the Fe solutes in the aluminum matrix.

Table 5.1 Chemical composition (wt.%) of the alloys.

Alloys	Fe	Cu	Si	Mg	Al
A3	0.30	0.01	0.025	0.001	Bal.
A7	0.70	0.01	0.023	0.001	Bal.

To quantitatively analyze Fe-rich particle distribution, the alloys after thermal holding treatments were examined using scanning electron microscope (SEM). All samples were sectioned parallel to the extrusion direction along the centerline and then polished. X-ray energy-dispersive spectroscopy (EDS) attached to the transmission electron microscope (TEM) was used to analyze the chemical composition of the dispersoids. In addition, image analysis technique was used to measure the size and volume fraction of Fe-rich particles. Furthermore, the electrical conductivity was measured at room temperature on the cylindrical samples (9.5 mm in diameter and 200 mm in length) after different thermal holding treatments using Megger DLRO10HD resistance ohmmeter in order to detect the Fe

solute contents.

Compressive creep tests were performed on samples (dia: 9.5 mm, L_0 : 19.0 mm) at temperatures from 100 to 200 °C and under various applied loads from 20 to 60 MPa. The samples were subjected to stepwise loading, where the load changed to a new value after the second creep stage had been established for a given load. In order to ensure a thermal stability, all specimens were held at the test temperature for 1 h prior to loading.

5.3 Results

5.3.1 Distribution of Fe-rich intermetallics and Fe solutes

Fig. 5.1 shows SEM back-scattered images of A3 and A7 alloys after two thermal holding treatments. As shown in Figs. 5.1(a-d), a large number of Fe-rich intermetallic particles was observed (white particles indicated by arrows), which was uniformly distributed throughout the matrix. The particles were identified as the equilibrium Al_3Fe phase from the electron backscattered diffraction (EBSD), which is also confirmed in the work of Shakiba *et al.* [25]. The average sizes of Fe-rich particles were measured to be a similar value of 0.36 μm in all these four conditions. Besides, it is found the volume fraction of particles is similar in alloy with same Fe content either after “HT” or “LT” heat treatment. For instance, as shown in Fig. 5.1(c-d), it is 4.26 vol. % in A7H to 4.33 vol. % in A7L, respectively. However, there is big difference in the volume of Fe-rich intermetallics in Alloys A3 and A7, which is rapidly increasing with increasing Fe content. The

calculated vol.% from image analysis is 1.8 vol.% in A3L and A3H while it is as high as 4.3 vol.% in Alloy A7L and A7H.

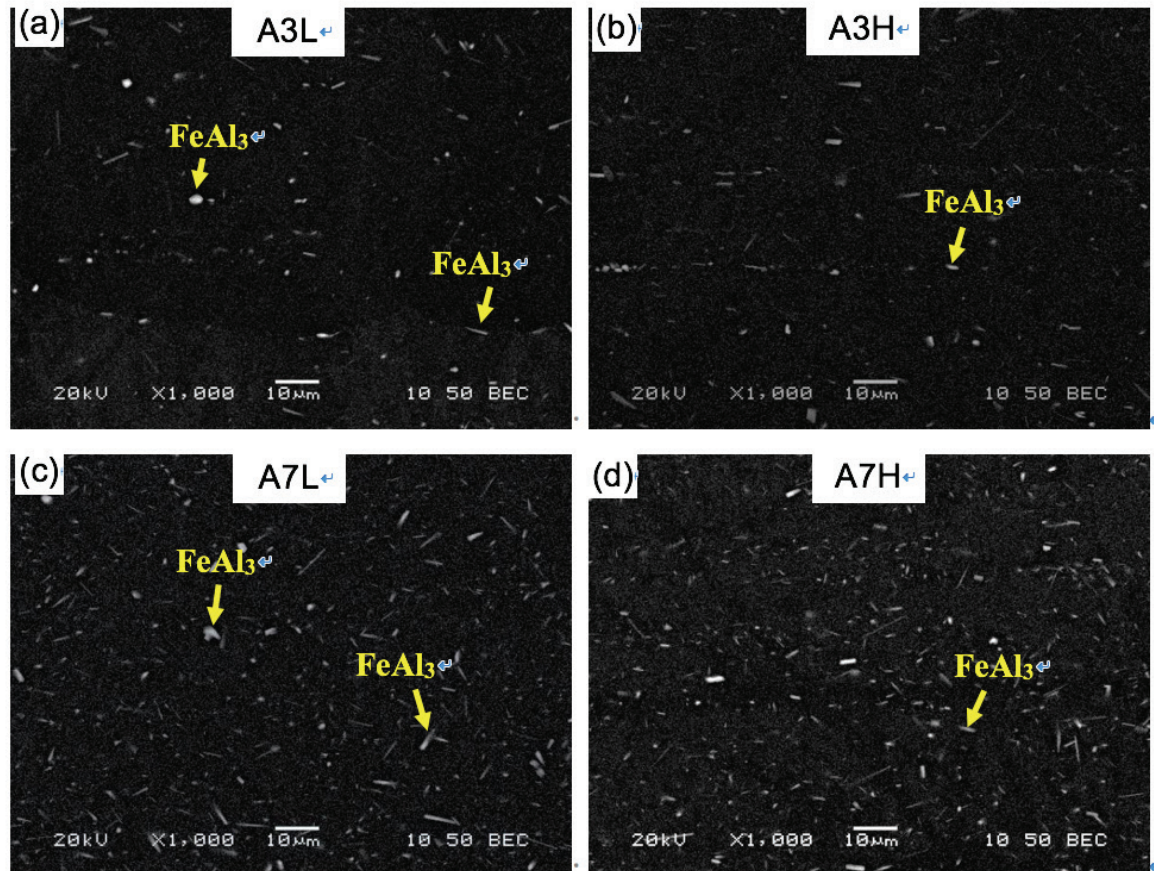


Fig. 5.1 SEM back-scattered micrographs of the Alloy A3 (a-b) and Alloy A7 (c-d) after thermal holding treatments.

On the other hand, the Fe solute level after thermal holding treatment was evaluated with the measurements of the electrical conductivity (EC). Based on the relationship between the EC and the concentration of alloying elements in solid solution, the quantitative estimation of the Fe solute content can be calculated through the following equation [26,27]:

$$\frac{1}{EC} = 0.0267 + 0.032Fe_{ss} + 0.002Cu_{ss} + 0.0068Si_{ss} + 0.003Mg_{ss} + 0.0003Particle\%$$

.....(Eq. 5.1)

where, Fe_{ss} , Cu_{ss} , Si_{ss} , and Mg_{ss} are the weight percentages of these elements in solid solution, and $Particle\%$ is the volume fraction of particles. The calculated Fe solute levels at different conditions are summarized in Table 5.2. It is clearly seen that after HT treatment the alloys showed comparatively higher Fe solute level compared with those alloys after LT treatment. In addition, the equilibrium solubility of Fe in Al–Fe system (Fig. 5.2) is also introduced to estimate the solute Fe levels [24]. As shown in Table 5.2, it is found that the calculated Fe solute contents are in good agreement with the theoretical values of binary Al–Fe phase diagram. It can be seen that the Fe solute level is $\sim 0.03\%$ after “HT” treatment (A3H and A7H) while it is 0.005–0.008% after “LT” treatment (A3L and A7L).

Table 5.2 Concentration of Fe solutes in the samples.

Specimens	EC measured, MS/m	Fe solutes estimated by EC values, wt.%	Fe solutes calculated from Al–Fe phase diagram, wt.% [26]
A3L	36.1	0.008	0.007
A3H	35.2	0.031	0.040
A7L	35.3	0.005	0.007
A7H	34.3	0.031	0.040

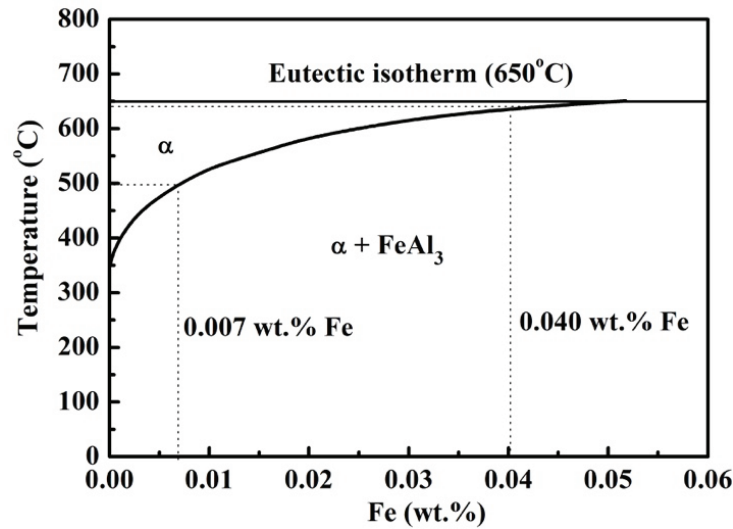


Fig. 5.2 Binary Al–Fe phase diagram illustrating the solid solubility of Fe content at a given temperature [24].

5.3.2 Creep behavior

Fig. 5.3 shows typical compressive creep curves of all alloys tested at 100 °C under a constant load of 45 MPa for 100 h. These curves are representative for all the experimental conditions. It was found in Fig. 5.3(a) that the total creep strain significantly decreases from 0.096 in A3L alloys to 0.001 in A7H alloys with an increase of Fe-rich particles from 1.8 to 4.3 vol.% and Fe solute level from 0.008 to 0.031 wt.%. There were two creep stages observed in the compressive creep tests. At the initial stage, the creep strain greatly increased with increasing time in a decelerating rate due to the work hardening (primary creep stage, $d\dot{\epsilon}/dt < 0$), and then the primary creep stage transits to a second stage where the creep strain increased at a nearly constant rate (quasi-steady stage, $d\dot{\epsilon}/dt \approx 0$). The minimum creep rate, $\dot{\epsilon}_m$, was calculated to be as an average creep rate in the second stage as shown in

Fig. 5.3(b). It was found that with increasing FeAl₃ particles and Fe solutes amounts, the $\dot{\epsilon}_m$ significantly decreases from $2.3 \times 10^{-7} \text{ s}^{-1}$ in A3L alloy to $2.2 \times 10^{-8} \text{ s}^{-1}$ in A3H alloy (the Fe solutes level increased from 0.008 to 0.031 wt.%), to $3.7 \times 10^{-8} \text{ s}^{-1}$ in A7L alloy (the FeAl₃ particles increased from 1.8 to 4.3 vol.%), and further to $4.9 \times 10^{-10} \text{ s}^{-1}$ in A7H alloy (both of FeAl₃ particles and Fe solutes increased), respectively. In conclusion, higher amounts of FeAl₃ particles and Fe solutes are greatly beneficial to the creep resistance, which is probably due to the pinning and impeding effects of both particles and solutes on dislocation movement [6,15].

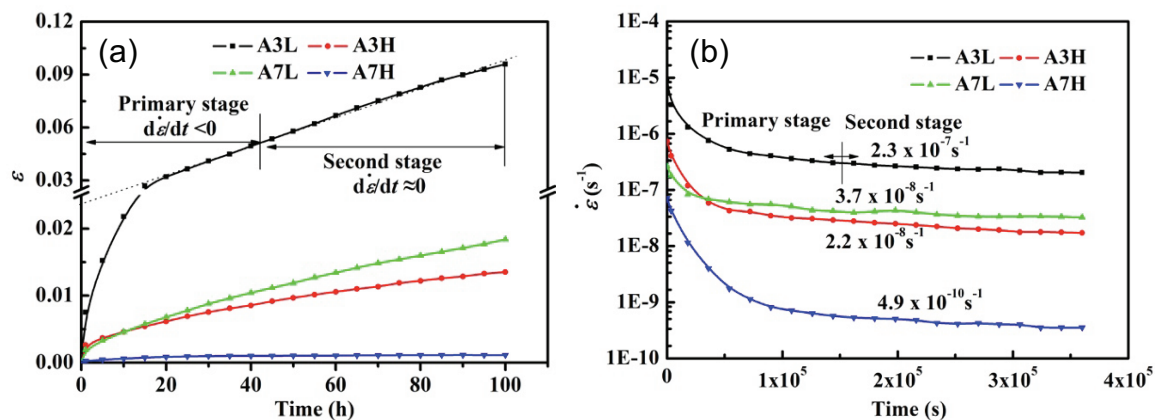


Fig. 5.3 Typical compressive curves of the alloys: (a) creep strain (ϵ) and (b) instantaneous creep rate ($\dot{\epsilon}$), tested at 100 °C and applied load of 45 MPa.

To better understand the effects of FeAl₃ particles and Fe solutes on the creep behavior, the creep tests were further conducted at various temperatures and under different applied stresses. Fig. 5.4 shows the minimum creep rate $\dot{\epsilon}_m$, as a function of applied stress σ , at 100, 150, and 200 °C. It can be seen that A7H showed the highest creep resistance, then A3H and

A7L displayed moderate creep resistance, and finally, A3L alloy had the lowest creep resistance. At 100 °C, A3H is slightly more creep resistant than A7L, but at 150 and 200 °C, A3H was less creep resistant than A7L. For a given temperature, the stress dependency is apparently given by a straight line, which implies a constant apparent stress exponent, n_a , (defined as $\partial \ln \dot{\epsilon}_m / \partial \ln \sigma$) [10]. The apparent stress exponent value n_a varies between 7.7 and 13.5 for alloys at the tested temperatures. The value of n_a was much larger than that of pure Al ($n = 3-5$), which is indicative of the presence of the threshold stress analogous to that of the dispersion strengthened alloys [28].

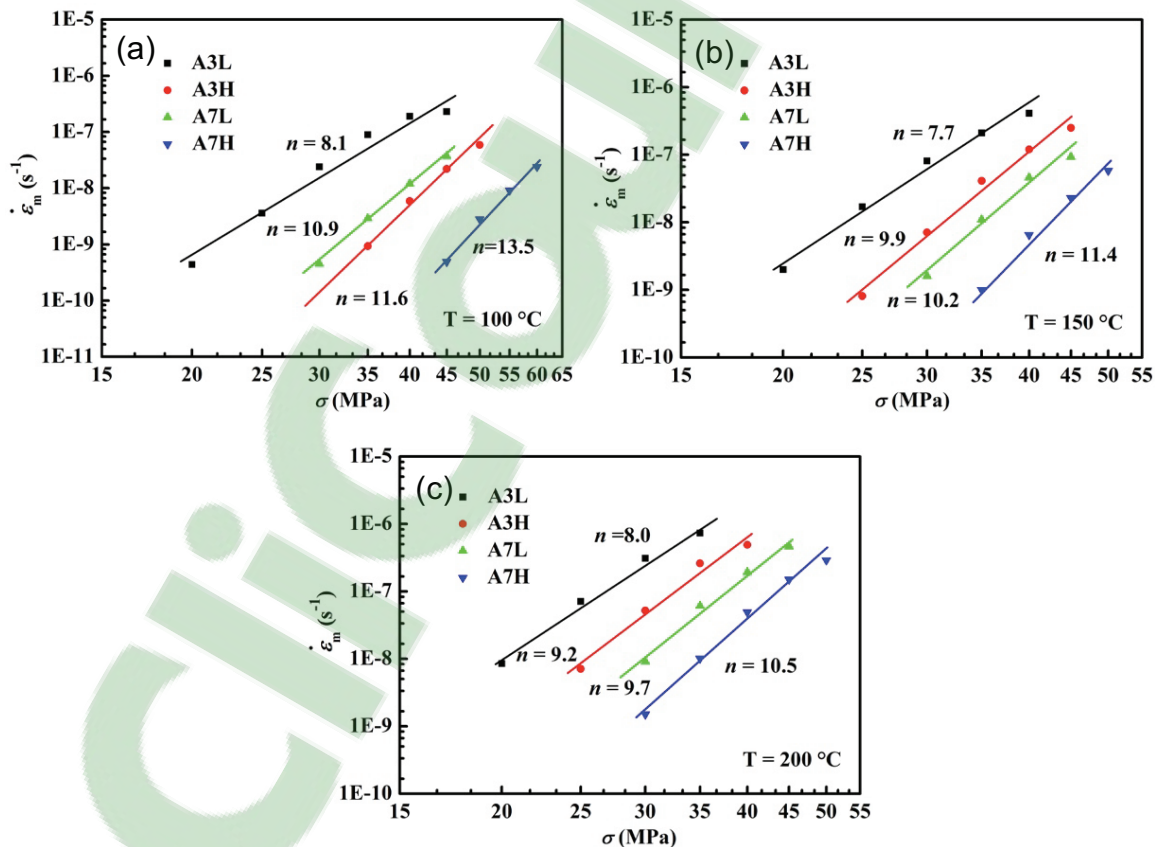


Fig. 5.4 Variations of minimum creep rate $\dot{\epsilon}_m$ with applied stress σ for alloys tested at 100 °C (a), 150 °C (b), and 200 °C (c).

The values of the threshold stress in the present alloys at various temperatures were estimated by extrapolating the linear fitting method as proposed by Li *et al.* [18]. For example, an extrapolation of the fitted lines to the minimum creep rate of 10^{-10} s^{-1} (shown in Fig. 5.5(a)) gives the threshold stress σ_{th} of 15.8, 13.5, and 11.5 MPa for A3L alloys at 100, 150 and 200 °C respectively. Fig. 5.5(b) shows the threshold stresses for all the alloys at different test temperatures. It can be clearly seen that the value of σ_{th} decreased with increasing creep temperature for all temperature conditions. At a constant temperature, A7H (high Fe particles and solutes) shows the highest σ_{th} , then A3H (high Fe solutes) and A7L (high Fe particles) alloys have higher σ_{th} and the least σ_{th} is the A3L alloy (low Fe particles and solutes), revealing the synergic effect of FeAl_3 particles and Fe solutes on the creep properties. At 100 °C, A3H alloy showed higher σ_{th} than A7L alloy (28.9 vs 25.9 MPa), indicating the stronger strengthening effect of Fe solutes than FeAl_3 particles. With increasing temperature to 150 and 200 °C, A3H alloy demonstrated lower σ_{th} compared with A7L alloy (19.6 vs 22.0 MPa at 150 °C and 15.7 vs 18.1 MPa at 200 °C), demonstrating stronger strengthening effect of FeAl_3 particles than Fe solutes.

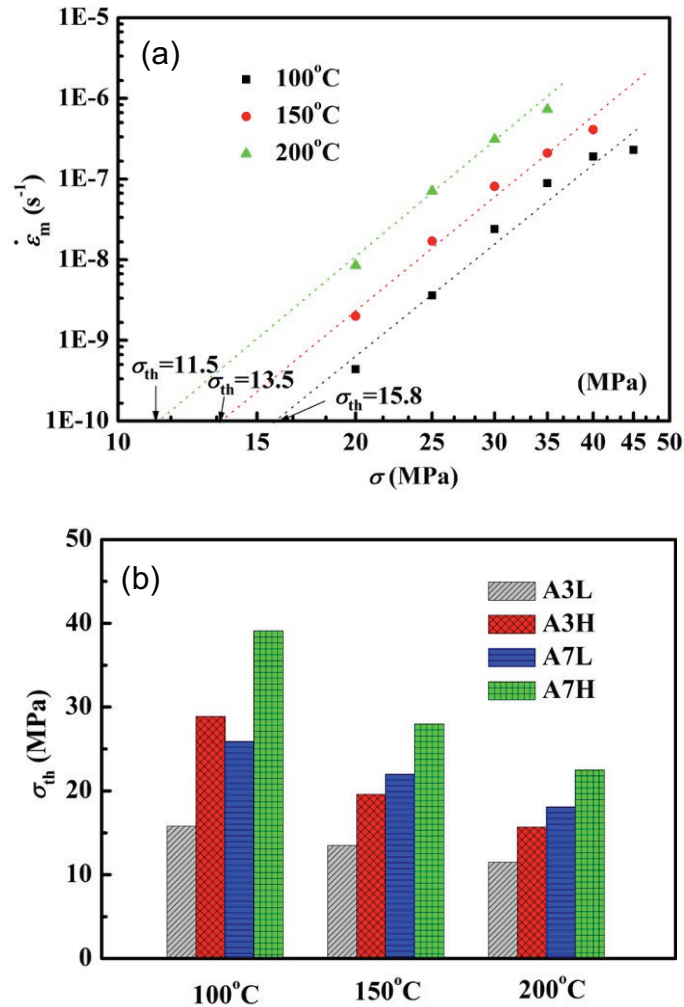


Fig. 5.5 Determining the threshold stress by linear fitting $\log \dot{\epsilon}_m$ against $\log \sigma$ for A3L alloys (a) and the threshold stress σ_{th} of all the alloys at the three test temperatures (b).

After determining the threshold stress, the creep behavior of alloys can be generally described by a modified power law equation as follows [10], in which the true stress exponents can be determined:

$$\dot{\epsilon}_m = A_0 \left(\frac{\sigma - \sigma_{th}}{G} \right)^{n_t} \exp \left(-\frac{Q}{RT} \right) \dots \dots \dots \text{(Eq. 5.2)}$$

where $\dot{\epsilon}_m$ is the minimum creep rate, σ is the applied stress and σ_{th} is the threshold stress, A_0 is a dimensionless constant, G is the shear modulus; n_t is the true stress exponent, Q is the activation energy, R is the universal gas constant and T is the absolute temperature.

Fig. 5.6 shows the plots of the minimum creep rate $\dot{\epsilon}_m$ against the effective stress $\sigma - \sigma_{th}$ on a logarithmic scale and the slope of plots gives the true stress exponent n_t . In literatures, the n_t has been frequently used for identifying the mechanisms controlling the creep process. According to different n_t values, the creep mechanisms are theoretically estimated as follows: $n_t = 3$, for creep controlled by viscous glide processes of dislocations [29], $n_t = 5$, for creep controlled by high-temperature dislocation climb [10], and $n_t = 8$ for lattice diffusion-controlled creep with a constant structure [30]. It is found that the values of n_t are between 2.8 and 4.8 under all temperatures, and indicating dislocation glide and climb controls the creep deformation in the experimental alloys. At 100 °C, the values of n_t varied from 2.8 to 3.4, indicating that the dislocation glide is the dominated rate-controlling deformation mechanism. With increasing creep temperature to 200 °C, more slip systems are activated, and the value of n_t was between 4.1 to 4.8, revealing the dislocation climb is the dominated deformation mechanism. Similar results were reported by Ishikawa *et al.* [31] and Sherby *et al.* [12] who postulated that dislocation glide was responsible for creep in pure aluminum at 100 °C with a true stress exponent of 3.0 and dislocation climb dominated the creep deformation for pure aluminum at 200 °C with a true stress exponent of 4.4, respectively.

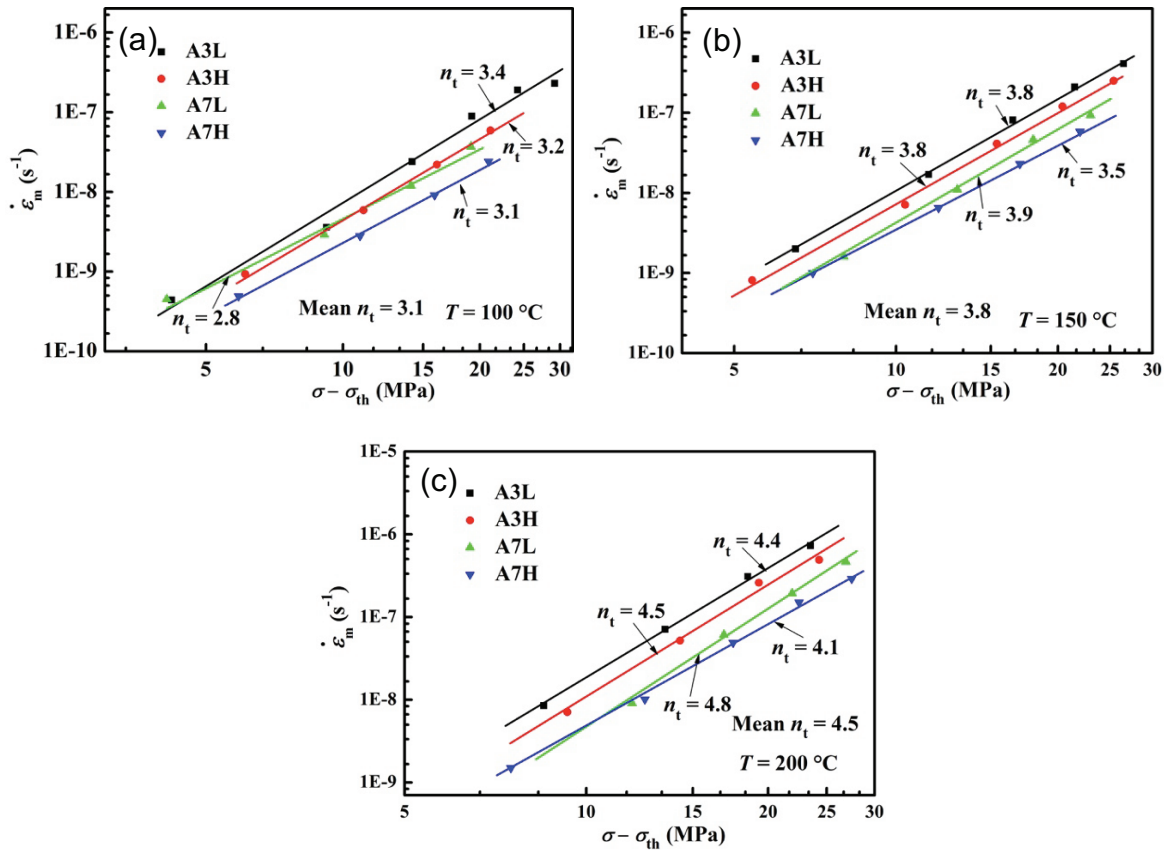


Fig. 5.6 Logarithmic plots of minimum creep rate $\dot{\epsilon}_m$ vs the effective stress, $\sigma - \sigma_{th}$, for alloys at three temperatures: 100 °C (a), 150 °C (b), and 200 °C (c).

5.4 Discussions

To understand the individual and combined effects of FeAl_3 particles and Fe solutes on the creep properties, the increments of the threshold stress $\Delta\sigma_{th}$ due to FeAl_3 particles and Fe solutes at various temperatures are calculated based on the data of Fig. 5.5(b), as listed in Table 5.3. The relationship between the total $\Delta\sigma_{th}$, and individual $\Delta\sigma_{th}(S)$ and $\Delta\sigma_{th}(P)$ with increasing temperature is plotted in Fig. 5.7. In general, the increment of the threshold stress $\Delta\sigma_{th}$ can be expressed by the sum of the $\Delta\sigma_{th}(P)$ for particles and $\Delta\sigma_{th}(S)$ for Fe solutes [11]:

$$\Delta\sigma_{th} = \Delta\sigma_{th}(P) + \Delta\sigma_{th}(S) \dots\dots\dots (Eq. 5.3)$$

It can be seen that both $\Delta\sigma_{th}(S)$ and $\Delta\sigma_{th}(P)$ decrease with increasing temperature, but the decreasing rate of $\Delta\sigma_{th}(S)$ is higher than $\Delta\sigma_{th}(P)$, suggesting the stronger temperature sensitivity of Fe solutes compared with that of $FeAl_3$ particles. The value of $\Delta\sigma_{th}$ from A7H–A3L is very close to the sum of individually calculated values of $\Delta\sigma_{th}(P)$ ($FeAl_3$ particles contribution from A7L–A3L and A7H–A3H) and $\Delta\sigma_{th}(S)$ (Fe solutes contribution from A3H–A3L and A7H–A7L), indicating the strengthening occurs due to the combined effect of both $FeAl_3$ particles and Fe solutes but the contribution of $FeAl_3$ particles and Fe solutes is independent.

Since the dislocation mechanism controls the creep deformation, this could be explained by the combined effect of $FeAl_3$ particles and Fe solutes in impeding dislocation movement [10,32], which means the stress required to cause the dislocation movement is higher than for a dislocation interaction with either particles or solute atoms. Similar results were reported by Karnesky *et al.* [10] during the creep process at 300 °C in Al alloys with two particle populations (Al_2O_3 incoherent dispersoids and Al_3Sc precipitates) where the overall threshold stress is equivalent to the sum of both contributions of two populations.

Table 5.3 Experimentally estimated increments of threshold stresses $\Delta\sigma_{th}$, $\Delta\sigma_{th}(P)$ for FeAl_3 particles and $\Delta\sigma_{th}(S)$ for Fe solutes at various temperatures (MPa).

		100 °C	150 °C	200 °C
$\Delta\sigma_{th}(P)$	A7L-A3L	10.1	8.5	6.6
	A7H-A3H	10.2	8.4	6.8
$\Delta\sigma_{th}(S)$	A3H-A3L	13.1	6.1	4.2
	A7H-A7L	13.2	6.0	4.4
$\Delta\sigma_{th}$	A7H-A3L	23.2	14.5	11.0

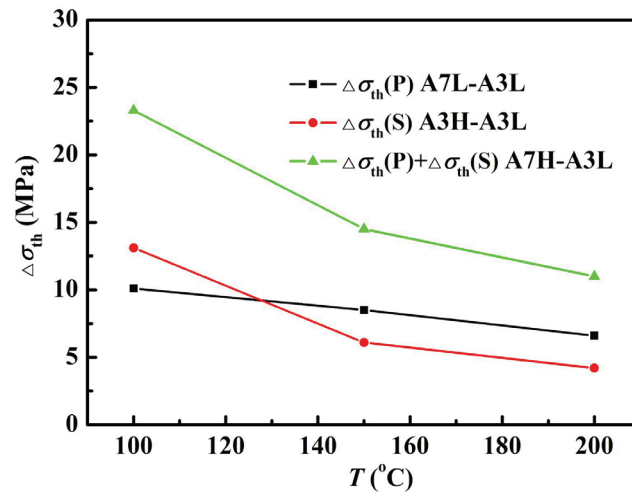


Fig. 5.7 The increment of threshold stress $\Delta\sigma_{th}$ due to FeAl_3 particles and Fe solutes with increasing temperatures.

5.4.1 Effect of Fe-rich intermetallic

The effect of FeAl_3 particles on the threshold stress could be due to the interaction between the dislocations and incoherent dispersion particles [32-34]. The most common explanation for σ_{th} is the stress required to cause dislocation bowing between the particles,

named Orowan stress σ_{or} , which is given by [33]:

$$\sigma_{or} = 0.84M \frac{Gb}{(\lambda-d)} \dots\dots\dots (Eq. 5.4)$$

where M is Taylor factor, d is average particle diameter, and λ is the inter-particle spacing. On the other hand, the attractive interaction between particle and dislocations leads to dislocation climb over the particles, then the threshold stress may be associated with the stress (σ_d) required to detach a dislocation from departure side of an obstacle, which is given by as follows [32]:

$$\sigma_d = \sigma_{or} \sqrt{1 - K^2} \dots\dots\dots (Eq. 5.5)$$

where K is a relaxation parameter that takes value between 0 (maximum attractive interaction) and 1 (no attractive interaction). The corresponding average inter-particle spacing λ , can be calculated according to the following equation [10]:

$$\lambda = d \left(\sqrt{\frac{\pi}{4f}} - 1 \right) \dots\dots\dots (Eq. 5.6)$$

where f is the volume fraction of the particles. Therefore, taking $M = 3.06$ and $K = 0.85$ [34], the calculated values of both threshold stresses ($\Delta\sigma_{or}$ and $\Delta\sigma_d$) are given in Table 5.4. The increment of Orowan stress ($\Delta\sigma_{or}$) is calculated to be the same value as 11.1 MPa for A7L–A3L and for A7H–A3H at 100 °C due to the volume fraction increase of FeAl₃ particles, which is close to that of the experimental estimated value $\Delta\sigma_{th}(P)$ of 10 MPa as shown in Table 5.3. The ratio ($\Delta\sigma_{th}/\Delta\sigma_{or}$) was calculated to be 0.91 and 0.92 for A7L–A3L and A7H–A3H, respectively. Therefore, it can be concluded that the Orowan dislocation

looping is the dominant factor responsible for the threshold stress. However, the values obtained from the detachment model (the same values of 5.8 MPa for A7L–A3L and for A7H–A3H, respectively) are much lower than the experimental determined threshold stress $\Delta\sigma_{th}(P)$.

At the high temperature of 200 °C, the experimental determined $\Delta\sigma_{th}(P)$ was 6.6 and 6.8 MPa for A7L–A3L and A7H–A3H, respectively, which is very close to the detachment stress $\Delta\sigma_d$ (as shown in Table 5.4). The ratio ($\Delta\sigma_{th}/\Delta\sigma_d$) was calculated to be the same value as 1.2 for A7L–A3L and A7H–A3H. Therefore, the origin of the threshold stress might be changed from the Orowan stress at 100 °C to the dislocation detachment stress at 200 °C. This is in consistent with the creep mechanism changes from dislocation glide to climb with increasing temperature from 100 to 200 °C as shown in Fig. 5.6. Similar results were reported by Kloc *et al.* [34] during the creep deformation in 2024 aluminum alloy where the estimated threshold stress decreases from a value close to the Orowan stress to a value near to the detachment stress with increasing creep temperature.

Table 5.4 The calculated Orowan stress σ_{or} and detachment stress σ_d for the alloys.

Specimens	100 °C				200 °C			
	σ_{or} , MPa	σ_d , MPa	$\Delta\sigma_{or}$, MPa	$\Delta\sigma_d$, MPa	σ_{or} , MPa	σ_d , MPa	$\Delta\sigma_{or}$, MPa	$\Delta\sigma_d$, MPa
A3L	11.0	5.8	-	-	10.4	5.5	-	-
A3H	10.6	5.6	-	-	10.0	5.3	-	-
A7L	22.1	11.7	-	-	20.8	11.0	-	-
A7H	21.7	11.5	-	-	20.5	10.9	-	-
A7L–A3L	-	-	11.1	5.8	-	-	10.4	5.5
A7H–A3H	-	-	11.1	5.8	-	-	10.5	5.6

5.4.2 Effect of Fe solutes

Although the amount of Fe solutes in both low and high Fe content alloys seems to be small (0.03% in the HT condition), the Fe solutes can have considerable impact on the creep properties in term of the minimum creep rate (Fig. 5.3(b)) and the threshold stress (Fig. 5.7). The contribution to the creep properties was greatly increased by the increasing Fe solutes, as shown in Figs. 5.3 and 5.7, which may be attributed to the Fe-solute-diffusion-controlled creep deformation as proposed by Sherby *et al.* [12,16,25]. It is suggested that the Fe solutes could segregate at the dislocations at the early stage of creep deformation to reduce the energy of dislocation. During the creep process, the initial stress field from the pile-up dislocation occurs under the applied shear stress and is balanced with the stress field from the subgrain boundary dislocations. Then, the opposing stresses from subgrain boundaries and from pile-up dislocations during creep deformation are cyclically relaxed by the diffusion of Fe solutes in the subgrain boundaries. Thereby, the pile-up dislocation is

allowed to glide or climb through the boundaries, and creep deformation of the material occurs. Due to a rather lower diffusion rate of Fe in aluminum matrix (as shown in Fig. 5.8), the pile-up dislocations were strongly hindered at the subgrain boundaries by Fe solute atoms. Sherby *et al.* [12] reported that addition of 200 ppm Fe in solution could significantly decrease the minimum creep rate by a factor of 10^6 compared with the same aluminum without Fe solution, which is attributed to the low Fe solute diffusion rate in the subgrain boundary region. The high pinning effect of Fe solutes results in a high external stress (threshold stress) is required to cause dislocation movement, which is confirmed by the high value of threshold stress ($\sigma_{th}(S)$) as shown in Table 5.3.

Besides, the improvement on the threshold stress from Fe solutes is decreasing with increasing temperature, as shown in Fig. 5.7 and Table 5.3, which can be attributed to the increasing diffusion rate of Fe. As shown in Fig. 5.8, the diffusion rate of Fe in Al rapidly increases with temperature. For instance, the diffusion of Fe in $6.4 \times 10^{-32} \text{ m}^2/\text{s}$ at 100 °C but it sharply increases to $2.6 \times 10^{-25} \text{ m}^2/\text{s}$ at 200 °C (Fig. 5.8). Therefore, the faster diffusion of Fe solute atoms weakens the pinning ability on the dislocation slip and decreases the threshold stress

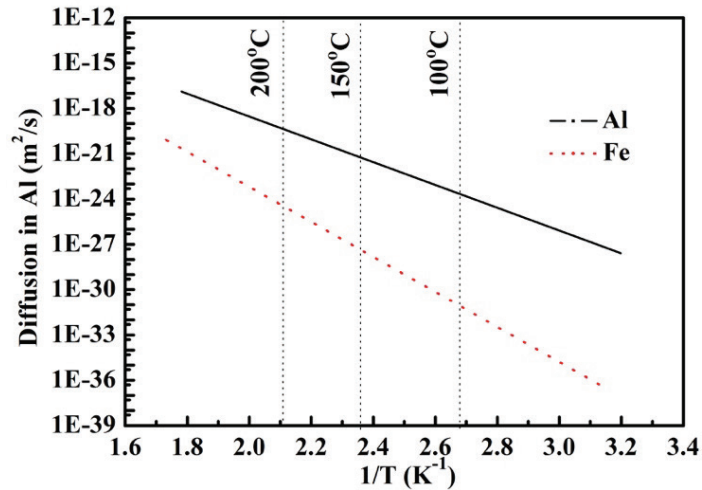


Fig. 5.8 The diffusion rate of Al and Fe in aluminum as a function reciprocal temperature [12].

5.5 Conclusions

The creep behavior of 8xxx aluminum conductor alloys containing submicron incoherent Fe-rich particles and different amounts of Fe solutes were studied. The following conclusions can be drawn from this investigation:

1. The presence of FeAl₃ particles and Fe solutes in 8xxx alloys significantly improved the creep resistance simultaneously at all test temperatures and stress levels, meanwhile, the strengthening effect is decreased with increasing temperature.
2. At 100 °C, Fe solutes (0.023 wt.%) had a stronger effect in increasing the creep resistance than FeAl₃ particles (2.5 vol.%), while at 150 and 200 °C, the high amount of FeAl₃ particles (2.5 vol.%) had a stronger effect than Fe solutes (0.023 wt.%).
3. The threshold stress is greatly increased with increasing FeAl₃ particles and Fe solutes.

The strengthening effect due to FeAl_3 particles and Fe solutes is independent and the value is equal to sum of the individual contribution in a linear relationship.

4. The threshold stress decreased with increasing temperature. For the particle contribution, the value is decreased with increasing temperature due to the strengthening mechanism changing from Orowan stress at 100 °C to detachment stress at 200 °C, while the Fe solutes contribution strongly decreased with increasing temperature due to the diffusion rate of Fe in Al rapidly increased with temperature.
5. With increasing creep temperature from 100 °C to 150 °C and further to 200 °C, the true stress exponent increases from 3.1 to 3.8 and further to 4.5, respectively.

References

- [1] V.M. Sizyakov, V.Y. Bazhin, A.A. Vlasov, *Metallurgist* 54 (2010) 409-414.
- [2] L. Pan, B. Bourassa, X.G. Chen, *Aluminium Alloys 2014 - ICAA14* 794-796 (2014) 1121-1126.
- [3] W.H. Yuan, Z.Y. Liang, *Mater. Des.* 32 (2011) 4195-4200.
- [4] W.W. Zhou, B. Cai, W.J. Li, Z.X. Liu, S. Yang, *Mater. Sci. Eng. A* 552 (2012) 353-358.
- [5] H.J. McQueen, E.H. Chia, E.A. Starke, *JOM* 38 (1986) 19-24.
- [6] X.Y. Zhang, H. Zhang, X.X. Kong, D.F. Fu, *Trans. Nonferrous Met. Soc. China* 25 (2015) 1763-1769.
- [7] C. Olin, in: *U.S.P. 3711339 (Ed.)*, US, 1973.
- [8] K. Conrod, H.J. McQueen, *JOM* 37 (1985) A16-A16.
- [9] H.J. McQueen, K. Conrod, G. Avramovic-cingara, *Can. Metall. Quart.* 32 (1993) 375-386.
- [10] R.A. Karnesky, L. Meng, D.C. Dunand, *Acta Mater.* 55 (2007) 1299-1308.
- [11] E.A. Marquis, D.N. Seidman, D.C. Dunand, *Acta Mater.* 51 (2003) 4751-4760.
- [12] O.D. Sherby, A. Goldberg, O.A. Ruano, *Philos. Mag.* 84 (2004) 2417-2434.
- [13] R.I. Babicheva, S.V. Dmitriev, Y. Zhang, S.W. Kok, N. Srikanth, B. Liu, K. Zhou, *Comp. Mater. Sci.* 98 (2015) 410-416.
- [14] A.V. Kazantzis, Z.G. Chen, J.T.M. De Hosson, *J. Mater. Sci.* 48 (2013) 7399-7408.
- [15] P.K. Chaudhury, K.T. Park, F.A. Mohamed, *Metall. Mater. Trans. A* 25 (1994) 2391-2401.
- [16] O.D. Sherby, O.A. Ruano, *Mater. Sci. Eng. A* 410 (2005) 8-11.

-
- [17] P.K. Chaudhury, F.A. Mohamed, *Acta Metall.* 36 (1988) 1099-1110.
- [18] Y. Li, T.G. Langdon, *Scripta Mater.* 36 (1997) 1457-1460.
- [19] S.P. Deshmukh, R.S. Mishra, I.M. Robertson, *Mater. Sci. Eng. A* 527 (2010) 2390-2397.
- [20] F. Naghdi, R. Mahmudi, *Mater. Sci. Eng. A* 616 (2014) 161-170.
- [21] M.E. Kassner, K. Smith, *J. Mater. Res. Technol.* 3 (2014) 280-288.
- [22] W.J. Li, B. Cai, Y.C. Wang, Z.X. Liu, S. Yang, *Mater. Sci. Eng. A* 615 (2014) 148-152.
- [23] K.W. Barber, K.J. Callaghan, *IEEE T. Power Deliver.* 10 (1995) 403-409.
- [24] C.M. Allen, K.A.Q. O'Reilly, B. Cantor, P.V. Evans, *Prog. Mater. Sci.* 43 (1998) 89-170.
- [25] M. Shakiba, N. Parson, X.G. Chen, *Mater. Sci. Eng. A* 619 (2014) 180-189.
- [26] Q.L. Zhao, B. Holmedal, Y.J. Li, *Philos. Mag.* 93 (2013) 2995-3011.
- [27] A. Mamala, W. Sciezor, *Arch. Metall. Mater.* 59 (2014) 413-417.
- [28] S.P. Deshmukh, R.S. Mishra, K.L. Kendig, *Mater. Sci. Eng. A* 381 (2004) 381-385.
- [29] A.H. Monazzah, A. Simchi, S.M.S. Reihani, *Mater. Sci. Eng. A* 527 (2010) 2567-2571.
- [30] Y. Li, T.G. Langdon, *Mater. Sci. Eng. A* 265 (1999) 276-284.
- [31] K. Ishikawa, H. Okuda, Y. Kobayashi, *Mater. Sci. Eng. A* 234 (1997) 154-156.
- [32] H. Watanabe, T. Mukai, K. Higashi, *Metall. Mater. Trans. A* 39A (2008) 2351-2362.
- [33] Y. Li, S.R. Nutt, F.A. Mohamed, *Acta Mater.* 45 (1997) 2607-2620.
- [34] L. Kloc, S. Spigarelli, E. Cerri, E. Evangelista, T.G. Langdon, *Acta Mater.* 45 (1997) 529-540.

CHAPTER 6
EFFECTS OF MINOR CU AND MG
ADDITIONS ON MICROSTRUCTURE
AND MATERIALS PROPERTIES OF
8XXX ALUMINUM CONDUCTOR
ALLOYS

Chapter 6 Effects of minor Cu and Mg additions on microstructure and materials properties of 8xxx aluminum conductor alloys

Abstract

Effects of minor Cu (0–0.29 wt.%) and Mg (0–0.1 wt.%) additions on the microstructure, electrical conductivity, mechanical and creep properties of 8xxx aluminum conductor alloys were studied in present work. The microstructure evolution was investigated using an optical microscope and the electron backscattered diffraction technique. The creep property was characterized by the primary creep strain in the primary stage and the minimum creep rate in the second stage of the creep deformation. Results showed that additions of minor Cu and Mg reasonably improved the ultimate tensile strength (UTS), but slightly reduced electrical conductivity (EC). The effects of Cu, Mg and Fe on the UTS and EC are quantitatively evaluated. Addition of Cu remarkably decreases the primary creep strain but has a negligible effect on the minimum creep rate, leading to a beneficial effect on the short-term creep resistance but no advantage to the creep resistance under the long-term creep process. The minor addition of Mg greatly reduces both primary creep strain and minimum creep rate, resulting in a significant and effective improvement on the creep resistance of 8xxx aluminum conductor alloys.

6.1 Introduction

As the economy has developed in the past few decades, the demand for the electrical conductor materials has been significantly increasing [1,2]. The 8xxx aluminum conductor alloys offer significant advantages such as low density, high conductivity to weight ratio and low cost over copper conductors. They progressively replace the copper conductor alloy in overhead transmission and electrical distribution within buildings [1,3]. For a wide application of aluminum conductors, it is necessary to satisfy the overall requirement of materials properties in electrical industry, notably the electrical conductivity, tensile strength and creep resistance [2,4]. Consequently, considerable efforts have been devoted to develop the aluminum conductor alloys with high comprehensive properties [4,5].

As minor alloying elements, Cu and Mg were often added in 8xxx aluminum alloys to improve the tensile strength and creep property and simultaneously to maintain the similar level of electrical conductivity [4-6]. Alloying of commercially pure aluminum alloy may create solid solution or individual phases that greatly improve tensile strength due to solid solution strengthening and precipitation strengthening [7,8]. However, the electrical conductivity may drop because of the enhanced scattering of free electrons at solute atoms and precipitates [9]. For electrical applications, it is a challenge to find a favorable combination of high electrical conductivity with enhanced mechanical properties in the alloy design and development.

In addition, creep property is one of the most important properties required in aluminum conductor alloys [2]. Previous investigations have demonstrated that the creep property of aluminum alloys can be significantly affected by alloying elements [6,10-15]. In general, alloying in pure aluminum increases the creep property by decreasing grain boundary mobility, impeding dislocation movement and accelerating dislocation multiplication [10,11,13]. Some researchers have investigated the effect of Cu addition on creep properties in aluminum alloys, however, the results appear to be somewhat inconsistent. Chaudhury *et al.* [10] reported that an Al-2wt.% Cu alloy exhibited higher creep property compared with pure aluminum due to the segregation of Cu atoms to moving dislocations. Reynolds *et al.* [14] investigated the creep behaviour of Al alloys containing (0.64–1.72 wt.%) Cu, and found that addition of Cu had a negligible effect on the creep property. Kato [15] studied the sliding in bicrystals of Al-Cu solid solutions and noted that small Cu addition decrease the creep property. Besides, some research works suggested that Mg addition in aluminum could enhance the creep property at relatively high temperatures ($T > 0.5 T_m$, where T_m is the absolute melting point of the alloy) [6,11]. Du *et al.* [11] reported that Mg atoms could increase the creep property by increasing the sliding threshold of grain boundaries by forming immobile Mg-Al clusters. Marquis *et al.* [6] reported that Mg addition could increase the creep property of Al-2wt.% Mg-0.2wt.% Sc alloy at 300 °C by increasing the threshold stress. To the author's knowledge, little investigation has been done on the effect of Cu and Mg on the creep properties of aluminum conductor alloys at

relatively low temperatures ($T \leq 0.4 T_m$), which are the normal service temperature range for most aluminum conductor alloys.

In the present study, 8xxx aluminum alloys with three Fe levels are alloyed with different Cu and Mg additions. The electrical conductivity and tensile strength as a function of Cu, Mg and Fe levels are quantitatively evaluated. The effect of Cu and Mg on the creep property is systematically investigated.

6.2 Experimental

The materials used in the experiments were 8xxx aluminum alloys with three fixed Fe levels (Al-0.3Fe, Al-0.5Fe and Al-0.7Fe base alloys), alloyed with various Cu and Mg concentrations. The addition of 0.18% and 0.29% Cu was made to Al-0.3Fe, Al-0.5Fe and Al-0.7Fe base alloys, and further addition of 0.025%, 0.05% and 0.1% Mg were made to Al-0.3Fe-0.18Cu, Al-0.5Fe-0.18Cu and Al-0.7Fe-0.18Cu alloys, respectively. A total of 18 alloys with various Cu, Mg and Fe contents were batched in an electrical resistant furnace and cast in the form of round billets with 4 inches in diameter by a direct chill (DC) cast unit. Their chemical compositions are shown in Table 6.1 (all alloy compositions in the paper are in wt.% unless otherwise indicated). All the rod samples with 9.5 mm in diameter, which are equivalent to the industrial 9.5 mm supply rods for drawn wire, were produced by the hot extrusion from DC cast billets.

Table 6.1 Chemical compositions of the experimental alloys investigated (wt.%).

Alloys	Fe	Cu	Mg	Si	Mn	Zn	Al
Al-0.3Fe (L00)	0.30	0.01	0.001	0.025	0.002	0.012	Bal.
Al-0.3Fe-0.18Cu (L20)	0.30	0.18	0.001	0.023	0.003	0.002	Bal.
Al-0.3Fe-0.29Cu (L30)	0.30	0.29	0.000	0.033	0.001	0.012	Bal.
Al-0.3Fe-0.18Cu-0.03Mg (L23)	0.30	0.18	0.025	0.031	0.002	0.012	Bal.
Al-0.3Fe-0.18Cu-0.05Mg (L25)	0.30	0.19	0.052	0.038	0.003	0.002	Bal.
Al-0.3Fe-0.18Cu-0.1Mg (L210)	0.30	0.18	0.100	0.049	0.002	0.012	Bal.
Al-0.5Fe (M00)	0.46	0.01	0.001	0.046	0.002	0.012	Bal.
Al-0.5Fe-0.18Cu (M20)	0.50	0.18	0.001	0.027	0.004	0.002	Bal.
Al-0.5Fe-0.29Cu (M30)	0.47	0.29	0.000	0.023	0.002	0.003	Bal.
Al-0.5Fe-0.18Cu-0.03Mg (M23)	0.46	0.18	0.026	0.051	0.002	0.013	Bal.
Al-0.5Fe-0.18Cu-0.05Mg (M25)	0.44	0.17	0.055	0.021	0.001	0.002	Bal.
Al-0.5Fe-0.18Cu-0.1Mg (M210)	0.47	0.18	0.100	0.049	0.002	0.012	Bal.
Al-0.7Fe (H00)	0.70	0.01	0.001	0.023	0.002	0.013	Bal.
Al-0.7Fe-0.18Cu (H20)	0.70	0.19	0.001	0.042	0.003	0.016	Bal.
Al-0.7Fe-0.29Cu (H30)	0.71	0.29	0.000	0.032	0.003	0.002	Bal.
Al-0.7Fe-0.18Cu-0.03Mg (H23)	0.69	0.18	0.027	0.052	0.002	0.013	Bal.
Al-0.7Fe-0.18Cu-0.05Mg (H25)	0.70	0.18	0.056	0.042	0.003	0.012	Bal.
Al-0.7Fe-0.18Cu-0.1Mg (H210)	0.72	0.18	0.100	0.051	0.002	0.013	Bal.

The electrical conductivity measurement was directly conducted on the samples of 9.5 mm in diameter and 200 mm long using Megger DLRO10HD resistance ohmmeter. Tensile test was carried out on cylindrical specimens (9.5 mm in diameter and 250 mm in length) according to ASTM B557 standard at room temperature. The compression creep tests were performed at 100 °C for 100 hours under a constant load 69 MPa using cylindrical specimens with a diameter of 9.5 mm and a length of 19 mm. To confirm the reliability of the results, 3 tests were repeated for each condition.

For microstructure examination, the extruded rods were first cut 20 mm in length and then sectioned longitudinally along the centerline. All the samples were polished and etched by the Keller's solution for 10 s and then were observed using optical microscope (OM), scanning electron microscope (SEM) and electron backscattered diffraction (EBSD) technique. The automated EBSD maps were conducted on the deformed structure with 0.2 μm step size using HKL Channel 5 software for substructure analysis. The linear intercept method was used to measure the subgrain size of alloys with different alloying contents [16]. To ensure statistical reliability, more than 200 subgrains were measured in each sample.

6.3 Results and discussion

6.3.1 Microstructure evolution

Fig. 6.1 shows optical micrographs of some typical alloys with different compositions after extrusion. Due to a very low solubility of Fe in aluminum matrix, almost all the Fe precipitated out in the form of Fe-contained intermetallic particles in the cast microstructure. After hot extrusion, the Fe-contained intermetallic particles were broken down to a number of fine intermetallic dispersion particles. For all the alloys, the fine intermetallic particles, which were confirmed as Al_mFe in our previous work [17], were uniformly distributed along the extrusion direction in aluminum matrix. With increasing Fe from 0.3 to 0.7% in the three base alloys, the volume fraction of Fe-contained intermetallic particles is increased from 1.8% in Al-0.3Fe to 3.2% in Al-0.5Fe and further to 4.4% in Al-0.7Fe alloys. The sizes of

Fe-contained intermetallic particles are very similar with an average value of 0.38 μm for all the alloys studied. When adding Cu and Mg in three base alloys, the volume fraction of intermetallic particles was found to remain almost unchanged compared to the corresponded base alloys, which are typically shown in Figs. 6.1(a) and (b) for the addition of 0.29% Cu and in Figs. 6.1(c) and (d) for the combined addition of 0.18% Cu and 0.1% Mg, respectively. This can be attributed to the higher solid solubility of Cu and Mg in aluminum, which is approximately 0.4% and 1.7% at room temperature, respectively [18]. Therefore, the additions of Cu up to 0.29% and Mg up to 0.1% in this study are expected to remain all in the solid solution after extrusion.

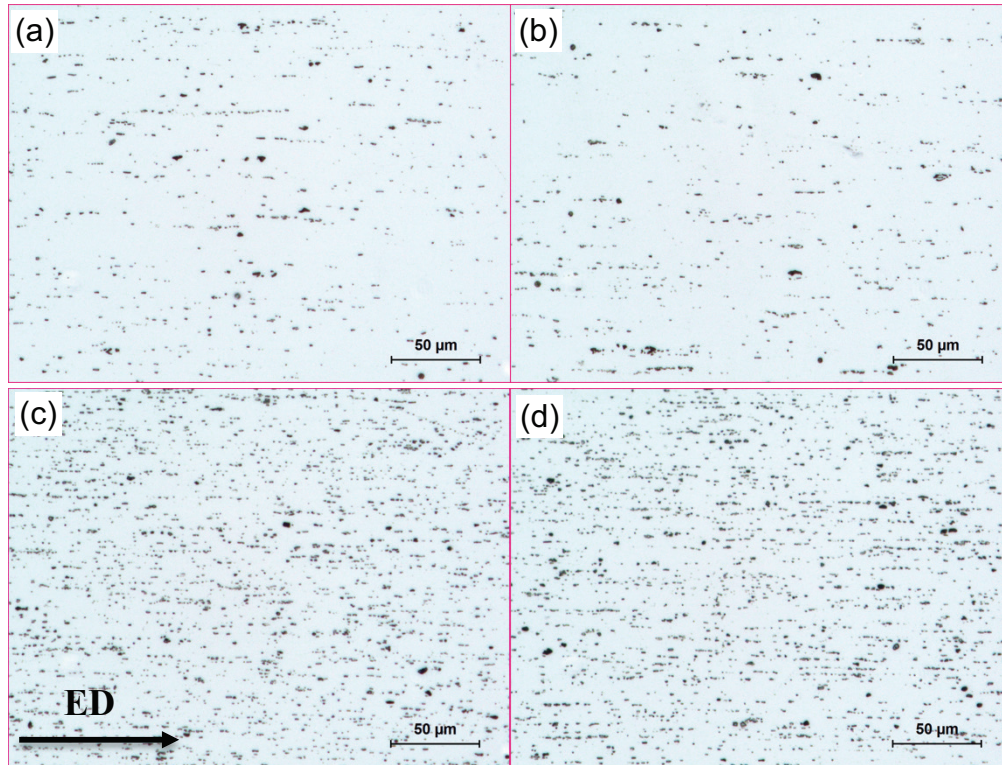
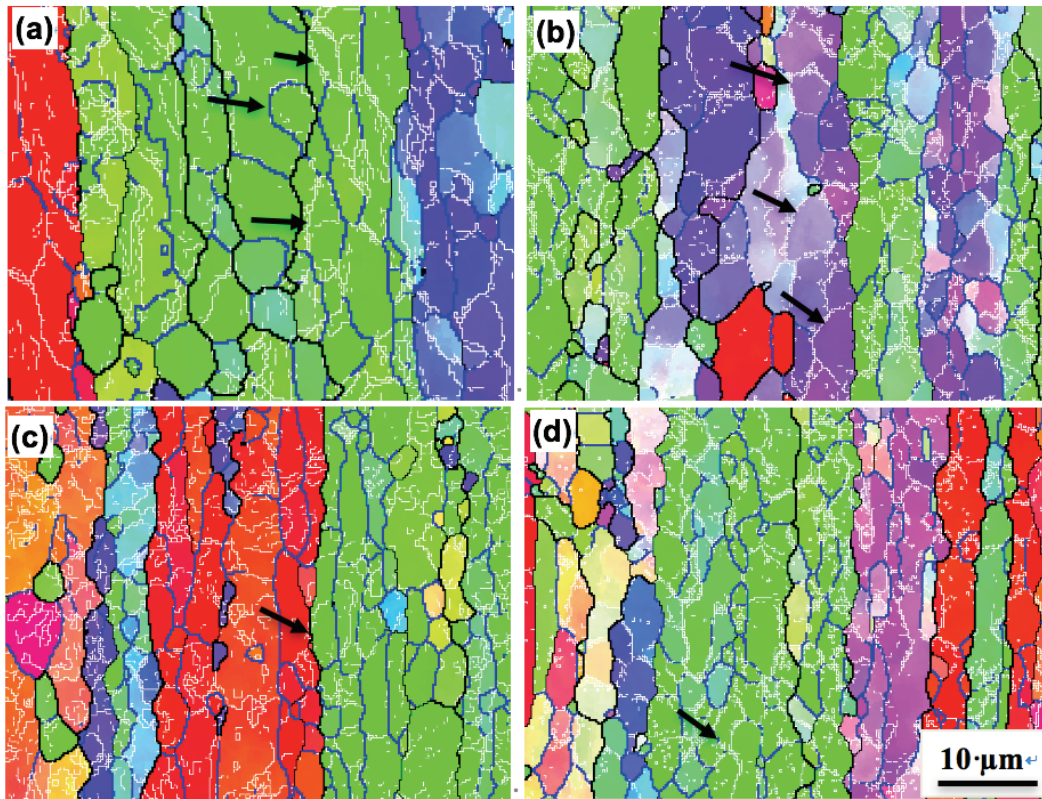


Fig. 6.1 Optical micrographs showing the particles distribution of the alloys: (a) Al–0.3Fe, (b) Al–0.3Fe–0.29Cu, (c) Al–0.7Fe, and (d) Al–0.7Fe–0.18Cu–0.1Mg, showing fine Fe-rich intermetallic particles distributed along the extrusion direction (ED).

To understand the microstructure evolution with additions of Cu and Mg in 8xxx aluminum alloys, EBSD orientation maps of the same typical alloy samples as in Fig. 6.1 were examined and the results are shown in Fig. 6.2. It can be seen that all the extruded alloys showed a characteristic of recovered structure, in which a large amount of low-angle boundaries with misorientation angles between of 1° and 5° were observed. In addition, the substructures were organized and large well-defined subgrains (arrowed in Fig. 6.2) were formed along the elongated grains with neatly arranged boundaries of $1\text{--}15^\circ$.



(e) Inversed pole figure color map and ED

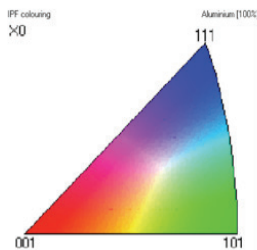


Fig. 6.2 Orientation image mapping showing the extruded microstructure of the alloys: (a) Al–0.3Fe, (b) Al–0.3Fe–0.29Cu, (c) Al–0.7Fe, (d) Al–0.7Fe–0.18Cu–0.1Mg, and (e) Inversed pole figure color map and extrusion direction (ED). Boundary misorientation indicated as follows: white lines 1–5°, blue lines: 5–15°, thin black lines: 15–30°, and thick black lines > 30°.

Though the recovered structure is present in all experimental alloys, there are differences in subgrain size due to additions of Cu and Mg (Fig. 6.3). It is found that with increasing Cu content up to 0.29%, the average subgrain size slightly decreases from 4.5 to 3.8 μm in Al–0.3Fe–Cu, from 3.7 to 3.3 μm in Al–0.5Fe–Cu and from 3.2 to 2.7 μm in Al–0.7Fe–Cu alloys (Fig. 6.3(a)), respectively. However, the addition of Mg (0.025–0.1%) in all three base alloys showed a negligible effect on subgrain size. As shown in Fig. 6.3(b), with increasing Mg contents, the subgrain size kept almost constant in three corresponded base alloys. This can be attributed to the various diffusion behaviors of Cu and Mg. Firstly, Cu solutes in aluminum solution have a lower diffusion rate than Al self-diffusion, which would strongly hinder the dislocation movement at the subgrain boundaries and enhance dislocation multiplication, leading to the retardation of the dynamic recovery [19,20]. However, the diffusion rate of Mg is very close to Al self-diffusion, resulting in little effect on the dynamic recovery. As a result, the subgrain size decreases with increasing Cu level while the Mg addition exhibited no change on subgrain size.

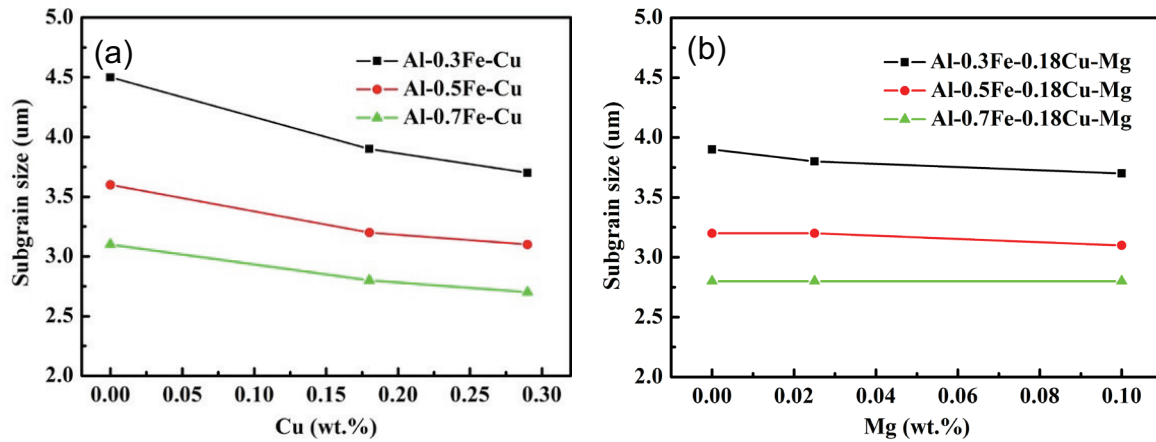


Fig. 6.3 The evolution of subgrain size with an increase of (a) Cu and (b) Mg contents.

6.3.2 Electrical conductivity and tensile strength

Fig. 6.4 shows the evolution of the electrical conductivity (EC) with different amounts of Cu and Mg in 8xxx aluminum alloys. It can be found that EC slightly decreases with increasing Cu and Mg due to enhanced scattering of free electrons at Cu and Mg solutes in aluminum [9]. With increasing Cu from 0 to 2.9%, EC decreases from 62.4 to 60.5 %IACS in Al-0.3Fe alloy and from 60.9 to 59.1 %IACS in Al-0.7Fe alloy (Fig. 6.4(a)), while with increasing Mg from 0% to 0.1%, EC decreases from 61.1 to 60.2 %IACS in Al-0.3Fe-0.18Cu alloy and from 59.7 to 58.8 %IACS in Al-0.7Fe-0.18Cu alloy (as shown in Fig. 6.4(b)), respectively.

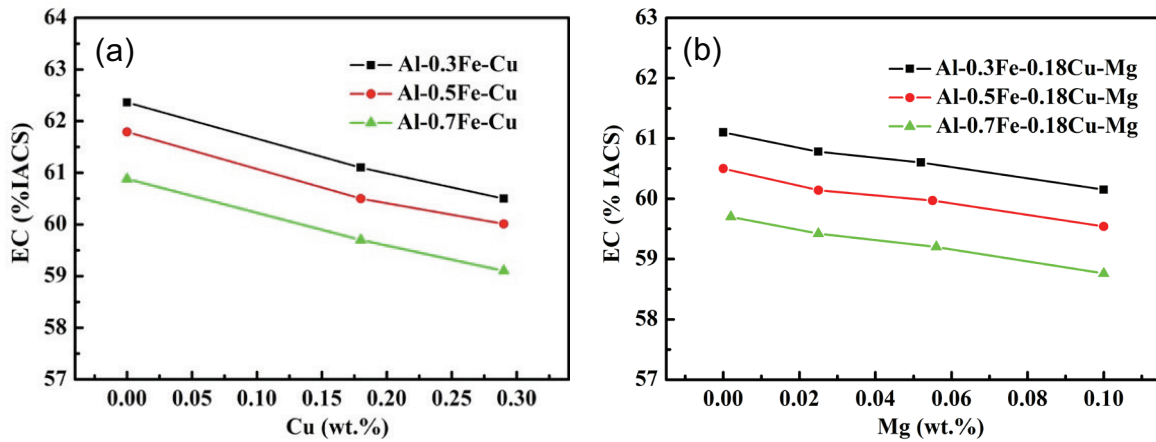


Fig. 6.4 Individual influences of selected alloying elements on electrical conductivity: (a) Cu and (b) Mg.

In the present work, the Matthiessen's law was adapted to establish the relationship of the EC with chemical composition as follows [21]:

$$\frac{1}{EC} = \rho_b + \sum_i \rho_i C_i + \rho_p f_p \quad \dots\dots\dots \text{(Eq. 6.1)}$$

where EC is the electrical conductivity, ρ_b is resistivity of the base alloy, $\sum_i \rho_i C_i$ is the sum of the resistivity contributions from the various solutes, *i.e.* ρ_i is the resistivity parameter and C_i is the concentration of the i^{th} solute, ρ_p is the resistivity parameter of the particles and f_p is the particle volume fraction. In the present study, due to the low solubility of Fe in aluminum, it can be assumed that almost all the Fe precipitated out into intermetallic particles and the volume fraction of intermetallic particles has a linear relation with Fe contents [18]. As all the alloys had similar particles size, the particle contribution $\rho_p f_p$ in Eq. 6.1 can be substituted by $\rho'_{Fe} C_{Fe}$. Consequently, Eq. 6.1 can be transformed to

$$\frac{1}{EC} = \rho_b + \rho_{Cu}C_{Cu} + \rho_{Mg}C_{Mg} + \rho'_{Fe}C_{Fe} \dots\dots\dots \text{(Eq. 6.2)}$$

where EC is in the unit of %IACS, ρ_{Cu} , ρ_{Mg} and ρ'_{Fe} are the resistivity parameters of Cu, Mg and Fe alloying elements, and C_{Cu} , C_{Mg} and C_{Fe} are the concentrations in wt.%. Based on the results from Fig. 6.4, the values of all resistivity parameters (ρ) can be obtained using the multiple linear regression. Therefore, an empirical expression can be obtained to predict the electrical conductivity as a function of alloying element contents:

$$\frac{1}{EC} = 0.01575 + 0.00174C_{Cu} + 0.00289C_{Mg} + 0.00096C_{Fe} \dots\dots\dots \text{(Eq. 6.3)}$$

The calculated values of the electrical conductivity versus the measured values with different Cu and Mg contents in three base alloys are plotted in Fig. 6.5. As demonstrated, there is excellent agreement between the calculated and experimental results. Furthermore, to evaluate the accuracy of the equation 6.3, the error between the calculated $EC(C)$ and the measured $EC(M)$ can be expressed as follows:

$$\text{Error}\% = \left| \frac{EC(C) - EC(M)}{EC(M)} \right| 100 \dots\dots\dots \text{(Eq. 6.4)}$$

The mean error for the 8xxx alloys with Cu contents (ranging from 0% to 0.29%) and Mg contents (ranging from 0% to 0.1%) is determined to be 0.13%, which confirms the excellent agreement between the calculated and measured EC. The equation 6.3 offers a very useful tool to predict the electrical conductivity as function of alloying elements (Cu, Mg and Fe) in 8xxx aluminum alloys.

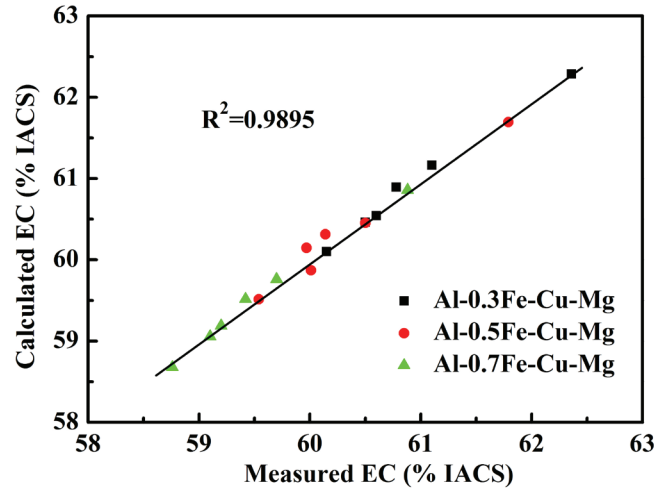


Fig. 6.5 Correlation between calculated and experimentally measured EC.

On the other hand, the UTS of the alloys were evaluated with different compositions and the results are shown in Fig. 6.6. It is found that the UTS show a nearly linear relationship with Cu, Mg and Fe contents and the values are moderately increased with increasing Cu and Mg concentrations due to solid solution strengthening and substructure strengthening [7]. The results reveal a beneficial effect of Cu and Mg on the mechanical properties. The overall strength σ (UTS) of the alloys can be expressed by an empirical equation in the form [6,8]:

$$\sigma(\text{UTS}) = \sigma_b + H_{\text{Cu}}C_{\text{Cu}} + H_{\text{Mg}}C_{\text{Mg}} + H_{\text{Fe}}C_{\text{Fe}} \dots\dots\dots (\text{Eq. 6.5})$$

where σ_b is strength of the base alloy in the unit of MPa, H_{Cu} , H_{Mg} , and H_{Fe} are the strengthening parameters of Cu, Mg and Fe, and C_{Cu} , C_{Mg} and C_{Fe} are the concentrations in wt.%, respectively. By using the multiple linear regression method, the values of σ_b and strengthening parameters (H) can be determined from the results of Fig. 6.6. Then, the

flowing equation can be used to describe the UTS as a function of alloying element contents:

$$UTS = 75.6 + 51.1C_{Cu} + 66.7C_{Mg} + 71.0C_{Fe} \dots\dots\dots (Eq. 6.6)$$

The calculated values of the UTS versus the measured values for 8xxx alloys with various Cu, Mg and Fe contents in different base alloys are plotted in Fig. 6.7, which demonstrated good agreement between the calculated and experimentally measured results. Besides, the mean error between the calculated and measured values for the 8xxx alloys is determined to be 1.0%, which confirms a very good accuracy of Eq. 6.6. Therefore, the obtained equation could be used to predict the UTS with various Cu, Mg and Fe additions in 8xxx aluminum alloys.

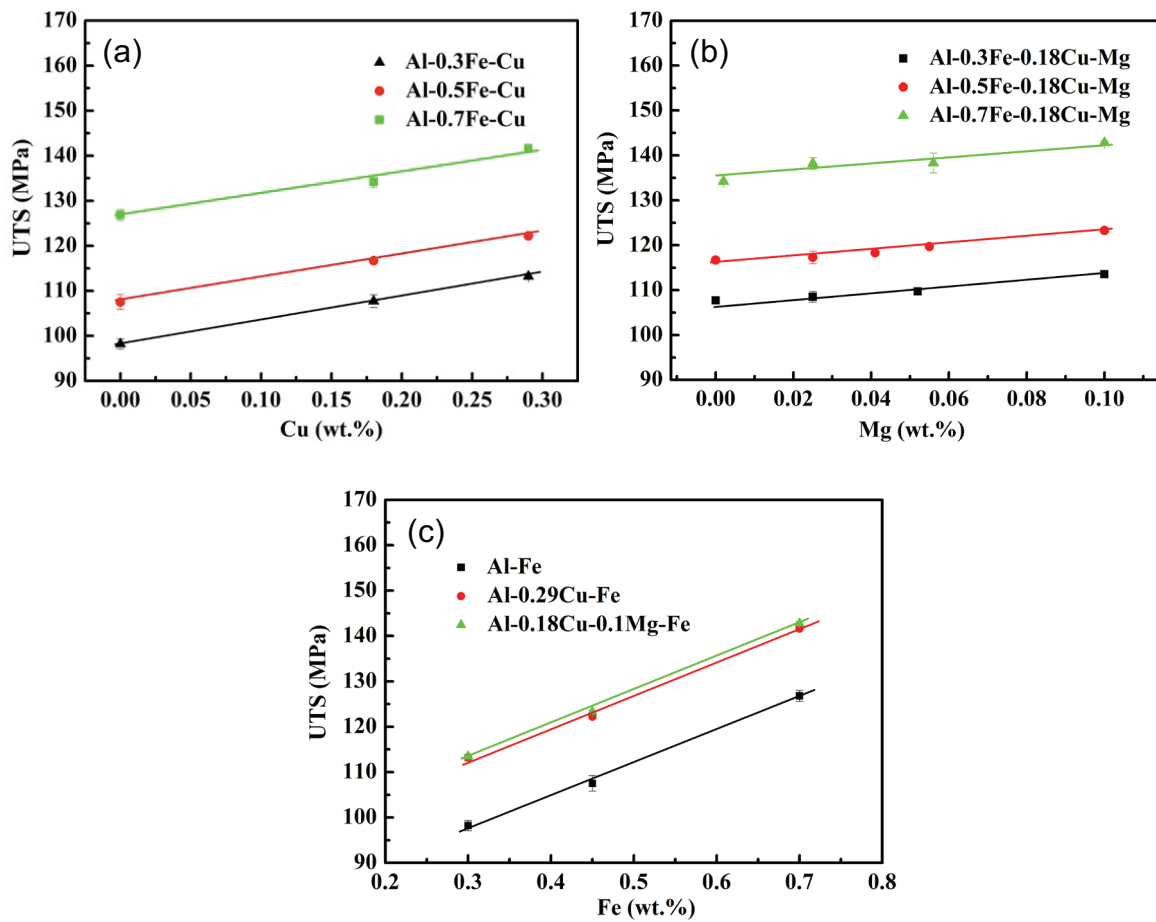


Fig. 6.6 Individual influences of selected chemical elements on UTS: (a) Cu, (b) Mg, and (c) Fe with a linear relationship.

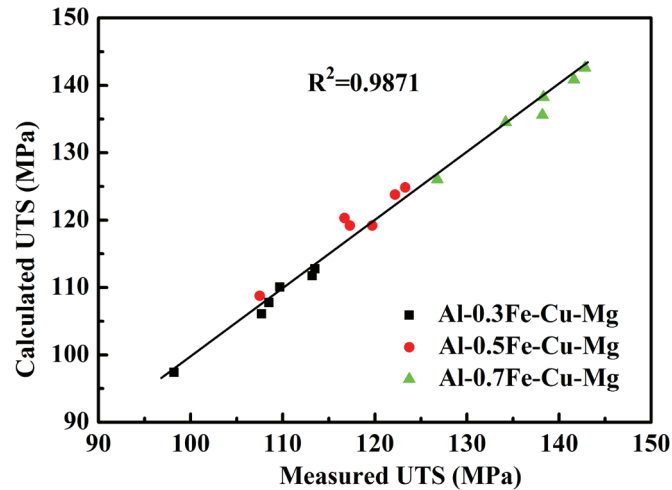


Fig. 6.7 Correlation between calculated and experimentally measured UTS.

For aluminum conductor alloys, high EC with enhanced UTS are most desirable in 8xxx aluminum alloys. However, high EC and high UTS are usually opposite because of the metallurgical nature of both properties. In an attempt to have a tool for alloy development and design, the EC and UTS profile of the alloys with different Cu and Mg additions in Al-0.3Fe, Al-0.5Fe and Al-0.7Fe base alloys are plotted in Fig. 6.8. This figure can be divided into three regions with different combinations of EC and UTS. It is evident that there is always a trade-off between EC and UTS. The region I is with high UTS but low EC while the region III is with high EC but low UTS. The region II in the middle has balanced EC and UTS. In the present study, both 0.3Fe (L00) and 0.5Fe (M00) alloys have higher EC but lower UTS (region III) compared to 0.7Fe (H00) alloy (region II). With additions of Cu and Mg (see black and red arrows), the 0.3Fe and 0.5Fe alloys move to the region II with more balanced EC and UTS. For example, the 0.5Fe alloys with Cu and Mg additions could have enhanced values of UTS at the expense of EC. It is also evident that the 0.7 alloys with

Cu and Mg additions tend to move from the region II to the region I, which have higher UTS but relatively lower EC. By adjusting Fe, Cu and Mg alloying elements, different combinations of EC and UTS could be obtained to fulfill different design requirements for specific applications.

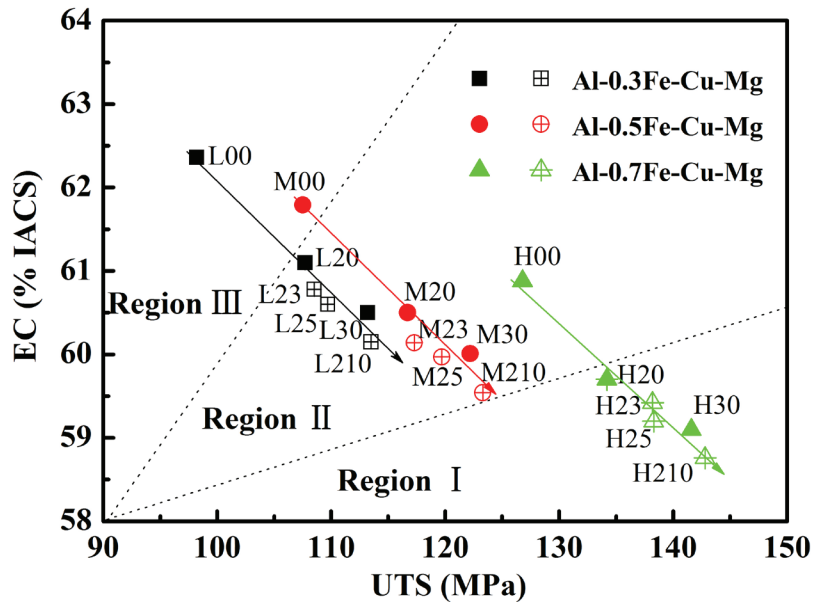


Fig. 6.8 EC and UTS profile of the alloys with different Cu and Mg additions. Arrows show the increasing Cu and Mg additions to their corresponding regions.

6.3.3 Effects of Cu and Mg on creep properties

Fig. 6.9(a) shows typical creep curves of samples of Al-0.3Fe alloys with different Cu contents as an example. During compressive creep deformation, the creep strain rapidly increases and the instant creep rate $\dot{\epsilon}$ decreases with increasing time, which can be defined as the primary creep stage. The primary stage ends when the $d\dot{\epsilon}/dt \approx 0$, and subsequently, the creep deformation runs to a quasi-steady state, in which the creep rate $\dot{\epsilon}$

becomes more and less constant (namely the second stage). The primary creep strain ε_p in the primary stage and the minimum creep rate $\dot{\varepsilon}_m$ in the second stage are used here to characterize the creep properties during creep deformation. The primary creep strain ε_p is obtained by extrapolating the second creep curve linearly back to the zero time (Fig. 6.9(a), dotted line) according to the literature [22] while the minimum creep rate $\dot{\varepsilon}_m$ is calculated as the average creep rate in the second stage (Fig. 6.9(b)).

Results of Fig. 6.9(a) shows that the total creep strain greatly decreases due to the addition of Cu in 0.3Fe alloys, which decreases from 6.87% in Al–0.3Fe base alloy to 2.44% in Al–0.3Fe–0.29Cu alloy, indicating a general beneficial effect of the Cu addition on the creep properties. However, the minimum creep rate is almost unchanged with increasing Cu contents (Fig. 6.9(b)), showing a mixed effect of the Cu addition on the creep properties. To clearly reveal the Cu effect, the primary creep strain ε_p and the minimum creep rate $\dot{\varepsilon}_m$ in all three alloys (Al–0.3Fe, Al–0.5Fe and Al–0.7Fe) have been calculated and the results are shown in Fig. 6.10. It can be seen that ε_p is significantly decreased with increasing Cu contents at a given Fe level (Fig. 6.10(a)). For instance, with increasing Cu from 0% to 0.29%, the ε_p decreases from 3.82% to 0.43% in Al–0.3Fe alloys (89% reduction), from 1.25% to 0.22% in Al–0.5Fe alloys (82% reduction), and from 0.71% to 0.15% in Al–0.7Fe alloys (79% reduction), respectively. On the other hand, the addition of Cu has almost no influence on $\dot{\varepsilon}_m$ in all studied Fe contents (Fig. 6.10(b)). For example, the $\dot{\varepsilon}_m$ keeps almost constant at $8.1 \times 10^{-8} \text{ s}^{-1}$ with 0.3Fe alloys and $5.5 \times 10^{-9} \text{ s}^{-1}$ with 0.7Fe alloys,

independent with the increase of Cu from 0% to 0.29%. It becomes now evident that the minor Cu addition shows a beneficial effect to improve the creep properties mainly in controlling the creep deformation in the primary stage. However, it has a negligible effect on the minimum creep rate in the second creep stage.

It is worthwhile mentioning that the improved benefit of Cu in the primary creep stage is decreased with increasing Fe contents in the base alloys (Fig. 6.10(a)), which can be attributed to the increasing fine Fe-rich dispersoids and small subgrains acting as strong barriers to the dislocation movements during creep deformation from higher Fe content alloys [20]. Therefore, it is suggested that Cu addition would be more effective in increasing the creep property in low Fe content alloys.

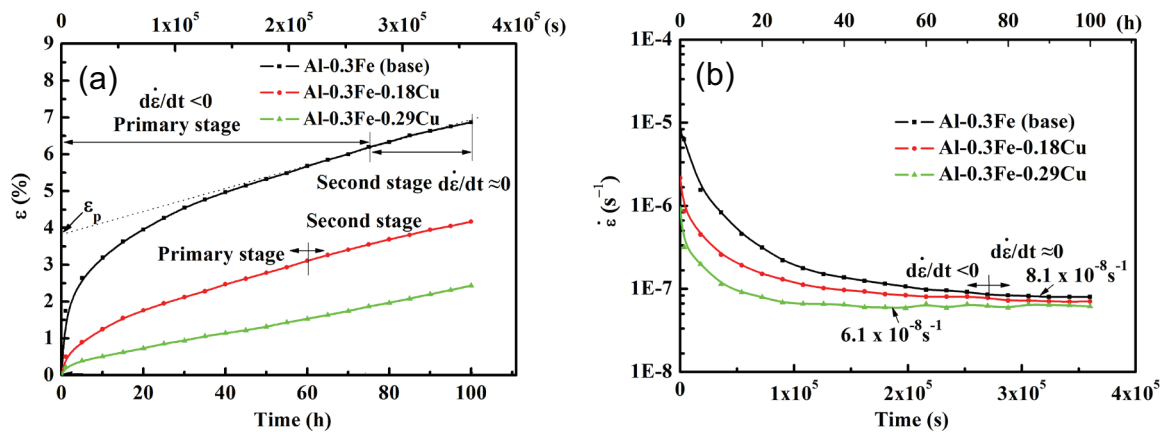


Fig. 6.9 Typical compressive creep curves of Al–0.3Fe alloys with different Cu contents, tested at 100 °C and applied load of 69 MPa: (a) creep strain (ϵ) and (b) instantaneous creep rate ($\dot{\epsilon}$).

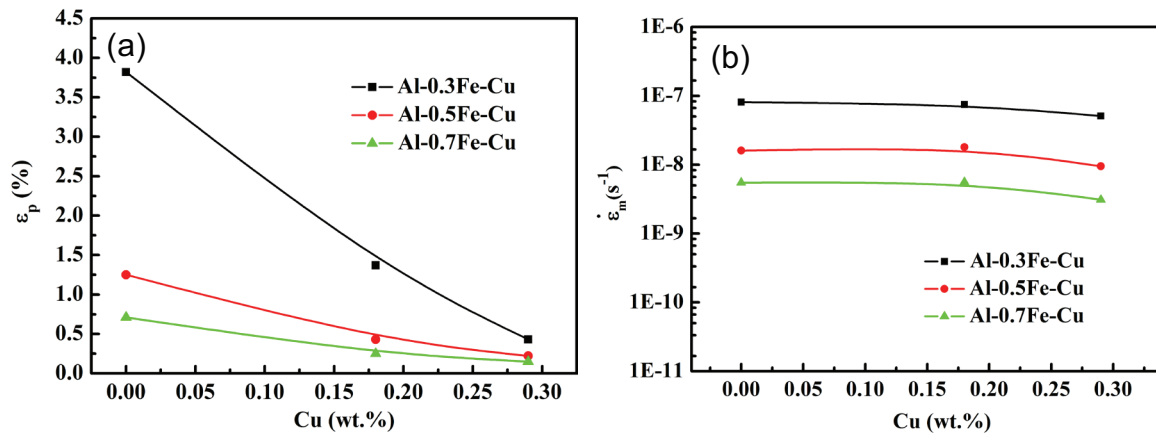


Fig. 6.10 Evolution of the primary creep strain (ϵ_p) (a) and minimum creep rate ($\dot{\epsilon}_m$) (b) as a function of Cu contents.

To illustrate the influence of Mg addition, the typical creep curves of samples of Al-0.3Fe-0.18Cu alloys with different amounts of Mg are shown in Fig. 6.11. With Mg addition, both of total creep strain and minimum creep rate considerably decrease with increasing Mg content. The evolution of the primary creep strain ϵ_p and the minimum creep rate $\dot{\epsilon}_m$ as a function of Mg contents in three alloys (Al-0.3Fe-0.18Cu, Al-0.5Fe-0.18Cu and Al-0.7Fe-0.18Cu) is shown in Fig. 6.12. Similar to the Cu addition, the primary creep strain ϵ_p has been greatly reduced with additions of Mg (Fig. 6.12(a)). For example, with Mg increasing from 0% to 0.1%, the ϵ_p greatly decreases from 1.37% to 0.09% in Al-0.3Fe-0.18Cu alloys (93% reduction), from 0.43% to 0.07% in Al-0.5Fe-0.18Cu alloys (84% reduction) and from 0.25% to 0.05% in Al-0.7Fe-0.18Cu alloys (80% reduction), respectively. However, different to the Cu addition, the $\dot{\epsilon}_m$ is significantly reduced with Mg addition at all studied Fe contents. As shown in Fig. 6.12(b), with Mg increasing from 0% to 0.1%, $\dot{\epsilon}_m$ noticeably decreases from $7.5 \times 10^{-8} s^{-1}$ to $4.8 \times$

10^{-10} s^{-1} in Al-0.3Fe-0.18Cu alloys (99% reduction), from $1.8 \times 10^{-8} \text{ s}^{-1}$ to $2.8 \times 10^{-10} \text{ s}^{-1}$ in Al-0.5Fe-0.18Cu alloys (98% reduction), and further from $5.6 \times 10^{-9} \text{ s}^{-1}$ to $2.1 \times 10^{-10} \text{ s}^{-1}$ in Al-0.7Fe-0.18Cu alloys (96% reduction), respectively. It can be clearly seen that the minor Mg addition can greatly decrease both ε_p and $\dot{\varepsilon}_m$, and therefore, has a great benefit to enhance the creep properties both in the primary stage and second stage of the creep deformation.

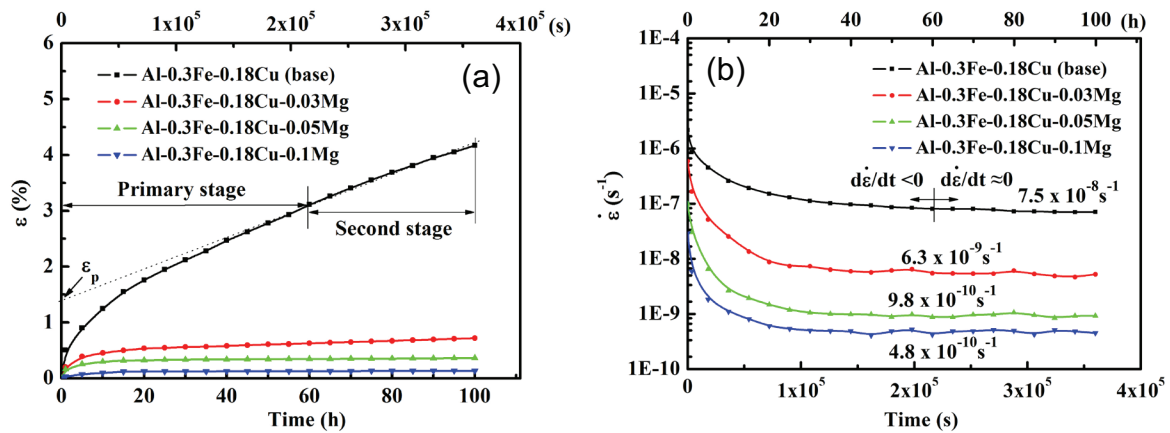


Fig. 6.11 Typical compressive creep curves of Al-0.3Fe-0.18Cu alloys with different Mg contents, tested at 100 °C and applied load of 69 MPa: (a) creep strain (ε) and (b) instantaneous creep rate ($\dot{\varepsilon}$).

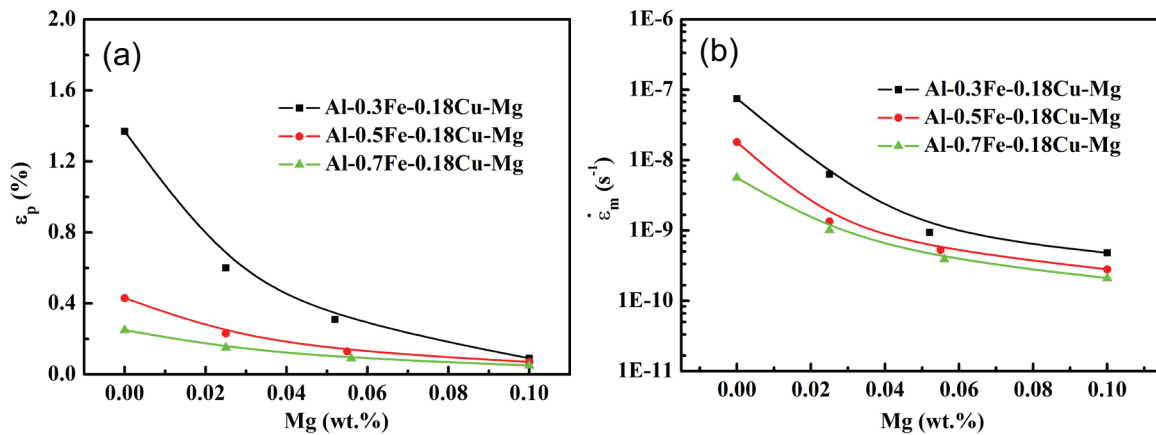


Fig. 6.12 Evolution of the primary creep strain (ϵ_p) (a) and minimum creep rate ($\dot{\epsilon}_m$) (b) as a function of Mg contents.

In the base alloys free of Cu and Mg, the creep properties are only dependent on the amount of Fe-rich intermetallic dispersion particles, which is in return controlled by Fe contents in the alloys (Fig. 6.1). This is because that in the base alloys only Fe-rich intermetallic dispersion particles can act as barriers to dislocation movement during creep deformation. The higher Fe contents and more Fe-rich intermetallic dispersion particles, the better the creep properties are (Figs. 6.10 and 6.12). With additions of minor Cu and Mg as solute atoms in aluminum matrix, the creep properties (both ϵ_p and $\dot{\epsilon}_m$) are significantly changed. For example, with additions of 0.29% Cu (Fig. 6.10(a)) or of 0.1% Mg in Al-0.3Fe alloys (Fig. 6.12(a)), the ϵ_p remarkably decreased and approached to the same value of Al-0.7%Fe alloys. However, Cu and Mg influence the creep properties through different ways, in which Cu has a benefit principally from the primary stage (Figs. 6.9 and 6.10) while Mg can have positive impacts on both primary and second stage of the creep deformation (Figs. 6.11 and 6.12). The different contributions of Cu and Mg on

creep properties, can be derived from the various behaviors of Cu and Mg. Firstly, the work hardening is the principle controlling mechanism on the primary stage of creep deformation [23], which is largely related to the solid solution levels that increases the work hardening ability of the material [20]. Therefore, the primary creep strain has been greatly reduced with increasing Cu and Mg solutes. In addition, the subgrain size decreases with Cu addition (Fig. 6.3), which can retard the dislocation movement and then further decreases the primary creep strain.

Secondly, the second stage of creep deformation is controlled by the glide and climb of dislocation at all studied alloys [24]. Hence, the creep properties can be influenced by the factors that can have effect on the movement of dislocations. However, it is reported that the interaction between the dislocation and Cu solute atmosphere is low [25,26], which is the probably reason for the negligible change on the minimum creep rate from Cu. On the other hand, the interaction of Mg with dislocation is stronger than Cu due to the higher atomic misfit with aluminum matrix [18,27], resulting in a possible increase in creep resistance in the second stage than Cu. Moreover, there is a strong tendency for Mg to form clusters with other elements [7,28] due to its much higher diffusivity (1.4×10^{-22} m²/s vs 6.3×10^{-24} m²/s of Cu at 100 °C [19,20]) and the presence of subgrain boundaries, which could lower the stacking fault energy, provide great obstacles to dislocation glide and make intersections more difficult, leading to the further decrease of the minimum creep rate [12,13,29,30]. The formation of Mg clusters has been confirmed by using 3D atom probe

tomography techniques in [12,13], resulting in a significant increase in the strength and a decrease in the minimum creep rate in aluminum alloys.

The creep is a relatively slow but time-dependent continuous deformation process. In the aspect of the creep resistance of materials, the improvement in the primary stage of the creep deformation (reducing the primary creep strain ε_p) is mainly related to the short-term creep resistance. The decrease of the minimum creep rate $\dot{\varepsilon}_m$ in the second stage of the creep deformation has major contribution on the long-term creep resistance. Because the minor Cu addition can only reduce ε_p but has negligible effect on $\dot{\varepsilon}_m$, the benefit effect of Cu in 8xxx alloys is limited to the short-term creep resistance. On the other hand, the minor Mg addition is highly effective in the increase of both short-term and long-term creep resistances by simultaneously reducing ε_p and $\dot{\varepsilon}_m$. Therefore, the minor alloying with Mg is more promising to enhance the creep resistance in 8xxx conductor alloys with less expense of the electrical conductivity in term of the small quantity and high effectiveness compared to the minor alloying with Cu.

6.4 Conclusions

1. Addition of Cu promotes the retardation of the dynamic recovery, leading to a finer subgrain size. However, little change on the microstructure has been observed with addition of Mg.
2. Additions of Cu and Mg reasonably increase the UTS but slightly decrease EC. The effects of Cu, Mg and Fe on the UTS and EC are quantitatively evaluated and summarized in Eqs. 6.3 and 6.6, which offer a good prediction of the UTS and EC as a function of alloying elements (Cu, Mg and Fe) in 8xxx aluminum conductor alloys.
3. Addition of Cu remarkably decreases the primary creep strain but shows negligible effect on the minimum creep rate, leading to a beneficial effect on the early creep deformation but no advantage to the creep resistance under the long-term creep process.
4. The minor addition of Mg greatly reduces both primary creep strain and minimum creep rate, resulting in a significant and effective improvement on the creep resistance of 8xxx aluminum conductor alloys.

Reference

- [1] O. Engler, G. Laptyeva, N. Wang, *Mater. Char.* 79 (2013) 60-75.
- [2] K.W. Barber, K.J. Callaghan, *IEEE T. Power Deliver.* 10 (1995) 403-409.
- [3] H.J. Mcqueen, E.H. Chia, E.A. Starke, *JOM* 38 (1986) 19-24.
- [4] A. Mamala, W. Sciezor, *Arch. Metall. Mater.* 59 (2014) 413-417.
- [5] M.Y. Murashkin, I. Sabirov, X. Sauvage, R.Z. Valiev, *J. Mater. Sci.* 51 (2016) 33-49.
- [6] E.A. Marquis, D.N. Seidman, D.C. Dunand, *Acta Mater.* 51 (2003) 4751-4760.
- [7] O. Ryen, O. Nijs, E. Sjolander, B. Holmedal, H.E. Ekstrom, E. Nes, *Metall. Mater. Trans. A* 37A (2006) 1999-2006.
- [8] R.A. Karnesky, L. Meng, D.C. Dunand, *Acta Mater.* 55 (2007) 1299-1308.
- [9] M.F. Ashby, H. Shercliff, D. Cebon, *Materials: engineering, science, processing and design*, 1st ed., Butterworth-Heinemann, Amsterdam; Boston, 2007.
- [10] P.K. Chaudhury, F.A. Mohamed, *Mater. Sci. Eng. A* 101 (1988) 13-23.
- [11] N.N. Du, Y. Qi, P.E. Krajewski, A.F. Bower, *Metall. Mater. Trans. A* 42A (2011) 651-659.
- [12] R.N. Lumley, A.J. Morton, I.J. Polmear, *Acta Mater.* 50 (2002) 3597-3608.
- [13] X. Sauvage, N. Enikeev, R. Valiev, Y. Nasedkina, M. Murashkin, *Acta Mater.* 72 (2014) 125-136.
- [14] G.H. Reynolds, F.V. Lenel, G.S. Ansell, *Metall. Mater. Trans. B* 2 (1971) 3027-3034.
- [15] M. Kato, *Trans. Jap. Ins. Met.* 10 (1969) 215.
- [16] C.J. Shi, W.M. Mao, X.G. Chen, *Mater. Sci. Eng. A* 571 (2013) 83-91.

-
- [17] L. Pan, K. Liu, F. Breton, and X. G. Chen, *J. Mater. Eng. Perform.* (2016), submitted for publication.
- [18] M. Spittel, T. Spittel, Part 2: Non-ferrous Alloys-Light metal, 4th ed., Springer Berlin Heidelberg, 2011.
- [19] G. Neumann, C. Tuijn, *Self-diffusion and impurity diffusion in pure metals: handbook of experimental data*, 1st ed., Elsevier Ltd, London, 2009.
- [20] M. Shakiba, N. Parson, X.G. Chen, *Mater. Sci. Eng. A* 636 (2015) 572-581.
- [21] B. Raeisinia, W.J. Poole, D.J. Lloyd, *Mater. Sci. Eng. A* 420 (2006) 245-249.
- [22] X.W. Wei, X.T. Zu, W.L. Zhou, *Mater. Sci. Tech.* 22 (2006) 730-733.
- [23] F.R.N. Nabarro, *Mater. Sci. Eng. A* 309 (2001) 227-228.
- [24] R.W. Westerlund, *Metall. Trans.* 5 (1974) 667-672.
- [25] F.A. Mohamed, *Mater. Sci. Eng.* 61 (1983) 149-165.
- [26] M.D. Halliday, C.J. Beevers, *J. Mater. Sci.* 6 (1971) 1254-1260.
- [27] R.I. Babicheva, S.V. Dmitriev, Y. Zhang, S.W. Kok, N. Srikanth, B. Liu, K. Zhou, *Comp. Mater. Sci.* 98 (2015) 410-416.
- [28] I.A. Ovid'ko, A.G. Sheinerman, R.Z. Valiev, *J. Mater. Sci.* 49 (2014) 6682-6688.
- [29] S.A. Mahmoud, K.H. Georgy, F.M. Mansy, R. Kamel, *phy. stat. sol. (a)* 51 (1979) 257-260.
- [30] X.Y. Liu, Q.L. Pan, X.L. Zhang, S.X. Liang, F. Gao, L.Y. Zheng, M.X. Li, *Mate. Sci. Eng. A* 599 (2014) 160-165.

CHAPTER 7
CONCLUSIONS AND
RECOMMENDATIONS

Chapter 7 Conclusions and recommendations

7.1 Conclusions

In the present work, the effect of alloying elements (Fe, Cu and Mg) on microstructure, electrical conductivity and mechanical properties of 8xxx aluminum alloys were systematically investigated. The relationship between the alloying concentration, the electrical conductivity and ultimate tensile strength was established. In addition, effect of small amount of Fe, Cu and Mg on the creep behavior of 8xxx aluminum conductor alloys at relatively low temperature ($T < 0.5 T_m$, where T_m is the melting point) was also systematically studied. The following conclusions can be drawn from this investigation:

Part I: Effect of Fe on microstructure and properties of 8xxx aluminum conductor alloys

- 1) The as-cast microstructure of 8xxx alloys was consisted of equiaxed α -Al grains and secondary Fe-rich intermetallics distributed in the interdendritic region. The deformed microstructure showed partially recrystallized structure for 0.3% Fe alloy but only dynamically recovered structures for 0.5% and 0.7% Fe alloys. The volume fraction of fine intermetallic particles increased and the subgrain size decreased after hot deformation with increasing Fe contents.
- 2) As the amount of Fe increased from 0.3% to 0.7%, UTS and YS increased by 25% and 28% while EC decreased by 2.3%, respectively. After annealing at 350 °C for 4 h,

EC increased more than 1% for all three alloys compared to that before annealing alloy in the trade-off with reduced tensile strength.

- 3) Addition of Fe to 8xxx alloys greatly improved the creep resistance. With increase of Fe content from 0.3% to 0.5% and 0.7%, the minimum creep rate significantly decreased from $7.5 \times 10^{-8} \text{ s}^{-1}$ to $1.8 \times 10^{-8} \text{ s}^{-1}$ and further to $5.6 \times 10^{-9} \text{ s}^{-1}$, respectively, for creep tests at 100 °C with a constant load of 69 MPa.
- 4) With increasing Fe contents from 0.3% to 0.5% and 0.7%, the creep threshold stress greatly increased from 24.6 to 30.1 and 33.9 MPa, respectively.
- 5) The introduction of the threshold stress in the analysis resulted in that the true stress exponent values were close to 3 for all three experimental alloys, indicating that the creep mechanism of 8xxx alloys is controlled by dislocation glide. The presence of larger volume fraction of fine intermetallic particles and smaller subgrain size in the higher Fe contained alloys are responsible for the better creep resistance.

Part II: Effect of Fe-rich intermetallic particles and Fe solutes on creep behavior of 8xxx aluminum conductor alloys

- 6) The presence of FeAl_3 particles and Fe solutes in 8xxx alloys significantly improved the creep resistance simultaneously at all test temperatures and stress levels, meanwhile, the strengthening effect is decreased with increasing temperature.

-
- 7) At 100 °C, Fe solutes (0.023 wt.%) had a stronger effect in increasing the creep resistance than FeAl₃ particles (2.5 vol.%), while at 150 and 200 °C, the high amount of FeAl₃ particles (2.5 vol.%) had a stronger effect than Fe solutes (0.023 wt.%).
 - 8) The threshold stress is greatly increased with increasing FeAl₃ particles and Fe solutes amount. The strengthening effect due to FeAl₃ particles and Fe solutes is independent and the value is equal to sum of the individual contribution in a linear relationship.
 - 9) The threshold stress decreased with increasing temperature. For the particle contribution, the value is decreased with increasing temperature due to the strengthening mechanism changing from Orowan stress at 100 °C to detachment stress at 200 °C, while the Fe solutes contribution strongly decreased with increasing temperature due to the diffusion rate of Fe in Al rapidly increased with temperature.
 - 10) With increasing creep temperature from 100 °C to 150 °C and further to 200 °C, the true stress exponent increases from 3.1 to 3.8 and further to 4.5, respectively.

Part III: Effects of minor Cu and Mg additions on the microstructure and properties of 8xxx aluminum conductor alloys

- 11) Addition of Cu promotes the retardation of the dynamic recovery, leading to a finer subgrain size. However, little change on the microstructure has been observed with addition of Mg.

- 12) Additions of Cu and Mg reasonably increase the UTS but slightly decrease EC. The effects of Cu, Mg and Fe on the UTS and EC are quantitatively evaluated and summarized in Eqs. 6.3 and 6.6, which offer a good prediction of the UTS and EC as a function of alloying elements (Cu, Mg and Fe) in 8xxx aluminum conductor alloys.
- 13) Addition of Cu remarkably decreases the primary creep strain but shows negligible effect on the minimum creep rate, leading to a beneficial effect on the early creep deformation but no advantage to the creep resistance under the long-term creep process.
- 14) The minor addition of Mg greatly reduces both primary creep strain and minimum creep rate, resulting in a significant and effective improvement on the creep resistance of 8xxx aluminum conductor alloys.

7.2 Recommendations

The effect of Fe, Cu and Mg additions on microstructure, electrical conductivity, mechanical and creep properties of the 8xxx aluminum conductor alloys was systematically investigated. Besides, the creep behavior of 8xxx alloys at elevated temperatures was studied. Based on the present study, following recommendations can be drawn for future work in this field:

- To better understand the compression creep behavior at relatively low temperature range, the microstructure evolution after very long time creep deformation is suggested to investigate.
- The effect of post-deformation heat treatments (*i.e.* annealing treatment) on microstructure evolution, electrical conductivity and mechanical properties of 8xxx aluminum alloys are suggested to investigate.
- The effects of grain refinement and homogenization treatment in 8xxx aluminum alloy on microstructure, electrical conductivity and mechanical property are advised to study.
- The distribution of minor Mg addition in the aluminum alloy should be systematically investigated under possible technique (*i.e.* atom probe tomography) to better understand the clustering effect.

PUBLICATIONS

JOURNAL ARTICLES

- Lei. Pan, Bruno Bourassa, and X.-Grant Chen, Effect of thermomechanical processing on electrical and mechanical properties of aluminum conductor alloys, *Materials Science Forum* Vols. 794-796 (2014) pp 1121-1126.
- Lei Pan, Kun Liu, Francis Breton, and X.-Grant Chen, Effect of Fe on microstructure and properties of 8xxx aluminum conductor alloys, *Journal of Materials Engineering and Performance* (2016), submitted for publication.
- Lei Pan, F.A. Mirza, Kun Liu and X.-Grant Chen, Effect of Fe particles and Fe solutes on compressive creep behavior of 8xxx aluminum conductor alloys, to be submitted in 2016.
- Lei Pan, Kun Liu, Francis Breton, and X.-Grant Chen, Effects of minor Cu and Mg on the microstructure and properties of 8xxx aluminum conductor alloys, to be submitted in 2016.

PATENT

- “Aluminum conductor alloys having improved creeping resistance”, United States Patent Application No. 62/365, 020, July, 2016.

CONFERENCE PAPERS

- Lei Pan, Kun Liu, Francis Breton, and X.-Grant Chen, Effects of alloying elements on microstructure and creep properties of 8xxx aluminum conductor alloys, COM 2016, September 11-15, 2016, abstract submitted.

SCIENTIFIC POSTERS

- Lei Pan, Kun Liu, Francis Breton, and X.-Grant Chen, Effect of minor Cu and Mg on the microstructure and creep properties of 8xxx electric conductor alloy, REGAL Students' Day, Chicoutimi, Canada, November 2015.
- Lei Pan, Bruno Bourassa, and X.-Grant Chen, Effect of Fe on the microstructure and creep properties of 8xxx series electric conductor alloy, REGAL Students' Day, Montreal, Canada, November 2014.
- Lei Pan, Bruno Bourassa, and X.-Grant Chen, Effect of thermomechanical processing on electrical and mechanical properties of aluminum conductor alloys, REGAL Students' Day, Montreal, Canada, October 2013. (Rewards of CIAC)